R-64-16

ENG

[redacted]

ENCLOSED ROTATING DISKS with SUPERPOSED THROUGHFLOW:

MEAN STEADY and PERIODIC UNSTEADY CHARACTERISTICS OF INDUCED FLOW

by

J. W. Daily

W. D. Ernst

V. V. Asbedian

HYDRODYNAMICS LABORATORY

Report No. 64

Prepared Under
Grants Nos.
DA-ORD-31-124-61-G5; DA-ORD-31-124-G131
DA Project No. 59901004
ARO (D) Proj. No. 2500-E
ARMY RESEARCH OFFICE (DURHAM)

APRIL 1964

MIT

DEPARTMENT
OF
CIVIL
ENGINEERING

SCHOOL OF ENGINEERING
MASSACHUSETTS INSTITUTE OF TECHNOLOGY
Cambridge 39, Massachusetts

R 64-16

DEPARTMENT OF CIVIL ENGINEERING
HYDRODYNAMICS LABORATORY
Massachusetts Institute of Technology

Enclosed Rotating Disks with Superposed Throughflow: Mean Steady and Periodic Unsteady Characteristics of the Induced Flow

by

J.W. Daily, W.D. Ernst and V.V. Asbedian

April 1964

Report No. 64

Prepared Under

Grant Nos. DA-ORD-31-124-61-G5, DA-ORD-31-124-G131

DA Proj. No. 59901004

AROD Proj. 2500-E

Army Research Office (Durham)

FINAL REPORT ACKNOWLEDGEMENT

This technical report also constitutes the final report for an investigation carried out in the MIT Civil Engineering Hydrodynamics Laboratory under the sponsorship of the Army Research Office (Durham) under contracts No. DA-OR(D)-31-124-61-G5 and No. DA-OR(D)-31-124-G 131. The work was done in part at the Computation Center at M.I.T., Cambridge, Massachusetts.

The scientific personnel participating in this project included Professor James W. Daily as principal investigator and three graduate students each of whom obtained M.S. degrees in Civil Engineering with theses based on the work of the project. Their names and thesis tables are as follows:

R.E.A. Arndt, "Effect of Superposed Throughflows on Motion Induced by Enclosed Rotating Disks"
SM Thesis, M.I.T., Course I, June 1962

W.D. Ernst, "A Solution for the Flow Fiel Produced by an Enclosed Rotating Disk with Net dial Flow"
SM Thesis, M.I.T. Course I, June 3

V.V. Asbedian, "Unsteadiness and Close C ance Torque for an Enclosed Rotating Disk w a superposed Throughflow"
SM Thesis, M.I.T. Course I, August 1963

Two technical reports summarize the findings as follows:

J.W. Daily and R.E.A. Arndt, "Enclosed Rotating Disks with Superposed Throughflow: A Survey of Basic Effects"
M.I.T. Hydro.Lab.Tech. Report No. 53, June 1962

J.W. Daily, W.D. Ernst and V.V. Asbedian, "Enclosed Rotating Disks with Superposed Throughflow: Mean Steady and Periodic Unsteady Characteristics of the Induced Flow"
M.I.T. Hydro.Lab Tech. Report No. 64, April 1964
(This is the present report)

Portions of the material in these two reports appeared in the above theses.

ABSTRACT

This is a report of a study of enclosed rotating disks with radial outward throughflow superposed on the fluid motion induced by the disk. The report presents information on the flow mechanics in the axial clearance space between the disk and stationary endwall including mean steady velocity distributions and unsteady periodicities. Also included are data on the interactions between fluid and boundaries as evidenced by torque transmission (disk friction) and by radial pressure gradients. A theoretical analysis is presented to predict the steady state values of torqye and pressure distribution and is compared with experimental results. Quantitative measurements of unsteadiness and periodicities which result under some conditions are analyzed and compared with previous smoke visualization data.

TABLE OF CONTENTS

VI Experimental Results

APPENDIX

DEFINITIONS AND NOTATIONS

A = empirical constant in equation for K_r

a = disk radius

b = disk thickness

c = spacing between disk tip and spacer ring (ft)

C_m = torque coefficient = $M/\frac{1}{2}\rho\omega^2 a^5$ for 2 sides of disk

D = probe tip diameter

f = frequency (cps)

g = gravitational acceleration (ft/sec^2)

K = that fraction of disk speed, ωr, at which the core rotates

K_r = K at radius r

K_o = K for zero throughflow

M = torque on both sides of disk (ft. lb)

n = number of cells in vortex system

p = pressure (lb/ft)^2

p_o = $\dfrac{\rho K_0^2\omega^2 a^2}{2}$

Q = volumetric throughflow <u>for one side of disk</u>.

r = radius

R = gas constant in Eq. (47)

$\mathbb{R}$ = Reynolds number $(\omega a^2)/\nu$

$\mathbb{R}_p$ = pipe Reynolds number used in evaluating Eq. (45)

$\mathbb{R}_r$ = Reynolds number $(\omega r^2)/\nu$

s = axial spacing (ft)

$\mathbb{T}$ = throughflow number $\left(\frac{Q}{\omega a^3}\right)\left(\frac{\omega a^3}{\nu}\right)^{1/5} = \left(\frac{Q}{\omega a^3}\right)\mathbb{R}^{1/5}$

(Note: this is the throughflow number defined in ref. (6) multiplied by $\mathbb{R}^{1/5}/2$)

DEFINITIONS AND NOTATIONS (Cont.)

U = tangential velocity in core (ft./sec)
u = tangential velocity (ft/sec)
u^* = local friction velocity = $\sqrt{\tau_{\gamma}/\rho}$
v = radial velocity (ft/sec)
V = radial velocity in the core (ft/sec)
v_o = reference radial velocity in boundary layer at disk (ft/sec)
$v_o{}^*$ = reference radial velocity in boundary layer at wall (ft/sec)
W = total velocity in the core relative to the disk surface
w = axial velocity (ft/sec)
y = axial distance from wall
Y' = coefficient in boundary layer thickness equation (51)
z = axial distance from disk
α = angle of local velocity (degrees)
α' = constant in boundary layer thickness assumption
β = core angular velocity
γ = specific weight (lbs/ft^3)
δ = boundary layer thickness at disk
δc = effective center correction in Eq. (49)
θ = boundary layer thickness at stationary endwall
ν = kinematic viscosity of fluid (ft^2/sec)
ρ = mass density of fluid (slugs/ft^3)
τ_r = radial component of shearing stress (lb/ft^2)
τ_{t_d} = tangential component of shear stress at rotating disk (lb/ft^2)
τ_{t_s} = tangential component of shear stress at stationary disk (lb/ft^2)
τ_{r_d} = radial component of shear stress at rotating disk (lb/ft^2)

DEFINITIONS AND NOTATIONS (Cont.)

τ_{r_s} = radial component of shear stress at stationary disk (lb/ft^2)

ω = disk angular velocity (radians/sec)

Subscripts

a = for r = a

abs = absolute = relative to fixed axes

o = for Q = 0 (except as noted)

Q = a function of Q

r = a function of r (except as noted)

rel = relative to disk

tip = at disk tip

t = a function of temperature

LIST OF FIGURES

I. INTRODUCTION

A. OBJECTIVE AND CONTENTS

This is a report of a study of enclosed rotating disks with radial outward throughflow superposed on the fluid motion induced by the disk. The report presents information on the flow mechanics in the axial clearance space between the disk and stationary endwall, including mean steady velocity distributions and unsteady periodicities. Also included are data on the interactions between fluid and boundaries as evidenced by torque transmission (disk friction) and by radial pressure gradients. A theoretical analysis is presented to predict the steady state values of torque and pressure distribution and is compared with experimental results. Quantitative measurements of unsteadiness and periodicities which result under some conditions are analyzed and compared with previous smoke visualization data.

B. DESCRIPTION OF THE DISK PROBLEM

Enclosed rotating disks simulate conditions frequently found in various types of rotating machinery. Examples include the shrouds and seals of compressors, centrifugal pumps and gas and hydraulic turbines. For these and for many other cases involving enclosed rotating members, the relation between induced flow-circulation and throughflow, on one hand, and power loss, on the other, is not clearly understood. These are factors that often are critical to the efficiency and effectiveness of rotating devices.

The fluid mechanics of the flow about a rotating disk is part of the more general problem of three-dimensional boundary layer flow. When a disk is rotated in a fluid there is a thin zone close to the disk in which, due to the centrifugal forces, there is a pumping action causing fluid to move radially outward. This is shown schematically in Fig. 1. The combination of a radial flow and the induced rotating flow produce a skewed boundary layer. In a skewed boundary layer the total velocity vector does not lie in a single plane. Such a boundary layer on the disk has the form of Fig. 2. Note that the plane in which the total velocity vector lies is warped. When the disk is totally enclosed in a housing continuity requires a net flow radially inward along the stationary endwalls of the housing as indicated in Fig. 1. This results in a similar skewed boundary layer on the stationary surfaces also. The fluid which is pumped radially outward received a net increase in angular momentum whereas the fluid which returns along the endwalls undergoes a net loss momentum. The end result is an equal and opposite torque on the disk and housing respectively. When there is a net flow through the system the boundary layers are modified and become more skewed. The flow recirculation inward at the endwall may or may not exist and the torque on the housing will differ from that on the disk by an amount depending on the tangential momentum flux carried out by the throughflow.

Skewed boundary layers exist on many rotating and non-rotating surfaces other than the simple case mentioned above. Examples are: flow over a delta type aircraft wing, the stationary and rotating blades of gas compressors and turbines and flow in curved ducts.

Depending upon the geometric and hydrodynamic parameters the flow in the axial clearance space between disk and housing will consist of two separated boundary layers with a rotating core of fluid between (like the example in Fig. 1) or of merged boundary layers with an inflexion point between. Each of these two regimes may persist with laminar or turbulent flow. It should be expected that throughflow would have a modifying effect. Moreover, a preliminary qualitative survey (6) showed that with throughflow and certain test conditions periodic fluctuations occur in the flow, the frequency of which is related to the rotational speed and throughflow rate.

Enclosed disk cases without throughflow have been treated in detail by prior investigations. The present problem concerns the various modifications of the fluid mechanics which occur when throughflow is introduced.

C. SCOPE OF INVESTIGATIONS AND RANGE OF VARIABLES

The experimental equipment used in this study is described in Section IV. It consists of a smooth disk rotating in a right-circular cylindrical housing with provisions for adjusting the axial clearance between disk and stationary endwalls and for adjusting throughflows which are admitted through annuli near the rotating axis and discharge from annuli at the outer periphery.

The experimental program included:

1. Comprehensive measurements of the mean steady values of the following, each as a function of axial spacing, Reynolds number and throughflow:
   - a) Disk friction torque
   - b) Boundary layer velocity profiles and their variation radially
   - c) Radial distribution of pressure

2. Measurements of velocity fluctuations and periodicities for the case of turbulent flow with separated boundary layers as functions of Reynolds number and throughflow.

The experimental variables for each type of test are summarized in Table I. The experimental results were analyzed with the aid of analog and digital computing equipment.

Equations were derived for predicting the core rotation, the torque and the radial pressure distributions for turbulent flow with separated boundary layers. Digital computer evaluations of the relations were performed for comparison with the experimental data.

TABLE 1

Experimental Variables

(Disk radius: a = 9.0625 inches)

	Fluid	Observ. Method	Inlet Geom.	B.L. Regime	Axial Spacing s/a	Radial Position r/a	Axial Position y/s	Disk Speed rpm	Reynolds Number $\mathbb{R} = \frac{\omega a^2}{\nu}$ (Nominal) x 10^{-5}	Throughflow (one side) Q = cfm std.air = cfs water (Nominal)	Throughflow Number $\mathbb{T} = (\frac{Q}{\omega a^3})\mathbb{R}^{1/5}$ (Nominal)
Mean Velocity Surveys	Air	Pitot	B	III	0.0138	0.469 0.648 0.828	Full Transverse	0 800 2000	0 2.9×10^5 6.9×10^5	26 0, 3, 13,26	0 0 to 0.15 0 to 0.044
	Air		B	IV	0.055	0.648	0.5	2000	6.9×10^5	0 to 26 (10 values)	0 to 0.065
						0.828	0.5	2000	6.9×10^5	0 to 26 (13 values)	0 to 0.065
	Air		B	IV	0.069	0.469 0.648 0.828	Full Transverse	800 2000	2.9×10^5 6.9×10^5	0,3,13,26	0 to 0.15 0 to 0.044
	Air		A	IV	0.069	0.469 0.648 0.828	Full Transverse	2000	6.9×10^5	0,3.4	0, 0.009
Torque	Water		A	III	0.0138			400 to 1200 (9 speeds)	2.6 to 8.5×10^6	0 to 0.045 (8 values)	0 to 0.08
				IV	0.0276			100 to 1200 (6 speeds)	5.8×10^5 to 7.3×10^6		
					0.069			100 to 1400 (6 speeds)	5.8×10^5 to 8.3×10^6		
					0.1241			300 to 1200 (5 speeds)	1.8 to 7.3×10^6		

TABLE 1 (Cont'd)

Fluid	Observ. Method	Inlet Geom.	B.L. Regime	s/a	r/a	y/s	rpm	$\mathbb{R}$ = (nominal)	Q (nominal)	[illegible] = (nominal)
Pressure Meas.										
Water		**A**	III	0.0138 0.069 0.1241	0.331 0.552 0.712 0.991 Spacer ring		0 to 1400 (6 speeds)	1.8 to $8.5\text{x}10^6$	0 to 0.044 (8 values)	0 to 0.08
Fluctuation Data										
Air	Smoke	**A**	IV	0.069	0.441		760 to 2100 (11 speeds)	2.9 to $6.9\text{x}10^5$	2.8, 7.2	0.007 to 0.04
Air	Hot Wire	**A**	IV	0.069	0.469	0.863	300 to 2000 (11 speeds)	1 to $6.9\text{x}10^5$	0, 1.6, 2.4, 4.9	0 to 0.06
					0.469	0.49 to 0.99	1000	$4 \text{ x } 10^5$	2.6, 13.5	0.0125 to 0.065
					0.648	0.49 to 0.99	2000	$6.9 \text{ x } 10^5$	2.4, 3.4	0.0065 to 0.009
					0.648	0.863	600 to 2000 (6 speeds)	2.1 to $6.9\text{x}10^5$	2.4, 4.9	0.0065 to 0.035
					0.828	0.863	800 to 2000 (5 speeds)	to $6.9\text{x}10^5$	2.4, 4.9	to 0.035

II. LITERATURE REVIEW

The following review is concerned primarily with the relatively few previous investigations that have treated aspects of throughflow effects and unsteadiness of enclosed disk flow. Moreover, interest is centers on the turbulent flow regimes. Related previous works include many experimental and theoretical studies of free and enclosed disks without superposed throughflow. The Bibliography in Section VIII contains the significant examples and thorough summaries of these will be found in references (7) and (8). Only a few of the main points of the most basic cases will be repeated here.

A. STUDIES WITH NO THROUGHFLOW

The first solution to the turbulent flow over a free disk was made by Von Karman (15) when he developed the boundary layer momentum theory, and used this, along with the 1/7 power law approximation for the tangential velocity, to solve for the torque. Radial pressure gradient was assumed to be zero. Upon assuming tangential and radial velocity distributions, he proceeded to find a functional form for a reference radial velocity in the boundary layer and boundary layer growth.

For the enclosed disk with separate boundary layers, Schultz-Grunow (27) by making three additional assumptions, was able to solve the equations for torque on the wall and disk simultaneously to obtain a solution for K, the ratio of core angular velocity to disk angular velocity, which could be substituted in the expression for shear stress to determine torque. These assumptions were: a constant core rotation with no radial flow between the boundary layers, a series solution for the reference radial velocity in the boundary layer, and a boundary layer on the stationary wall. His results for the torque coefficient (both sides of the disk), boundary layer thickness and core angular velocity ratio are

$$C_m = \frac{0.0622}{\mathbb{R}^{1/5}} \qquad (1)$$

$$\delta = \frac{0.1025\ r}{\mathbb{R}_r^{1/5}} \qquad (2)$$

$$K = \frac{\beta}{\omega} = 0.512 \qquad (3)$$

where

$\mathbb{R} = \frac{\omega a^2}{\nu}$ = Reynolds number based on disk radius a

$\mathbb{R}_r = \frac{\omega r^2}{\nu}$ = local Reynolds number on disk

β = angular velocity of core between boundary layers

ω = disk angular velocity

These relations showed no effect of gap width between disk and housing.

In an analysis of the Navier-Stokes equations of the flow produces by coaxial disks when one is stationary, K. Stewartson (31) predicted that there will be no rotation of the core fluid between the disks and no torque on the stationary disk. However, Batchelor (2), using physical arguments and the general properties of the governing equations, concluded that, in almost all cases, the main body of the fluid will be rotating.

Soo (30) reported a solution for turbulent flow with merged boundary layers. Assuming boundary layer symmetry, the fluid velocity midway between disk and endwall should be

$$u = \frac{\omega r}{2} \qquad (4)$$

The resulting relation for moment coefficient for both faces of the disk was

$$C_m = \frac{0.0622}{\left(\frac{s}{a}\right)^{1/4} \mathbb{R}^{1/4}} \qquad (5)$$

where s is the axial spacing.

Daily and Nece (7,8) were able to verify, theoretically and experimentally, the existence of four regimes of flow with an enclosed disk. They are:

<u>Regime I</u> - close clearance laminar case of two merged boundary layers giving a continous (linear in limit) variation of tangential velocity across the spacing between the disk and the housing.

<u>Regime II</u> - separate laminar boundary layers on the disk and housing, separated by a rotating core, with boundary layer radial flow outward along the disk and inward along the housing wall.

<u>Regime III</u> - turbulent flow with merged boundary layers

<u>Regime IV</u> - separate turbulent boundary layers on the rotating disk and housing again separated by a rotating core, and with a radial secondary flow along disk and wall.

The analysis of Daily and Nece made similar physical assumptions to those of Schultz-Grunow except that the effect of the cylindrical casing was taken into consideration. Their conclusions from theory and experiment for the turbulent flow cases were:

> Regime III, merged boundary layers: Soo's relation [Eq. (5)] predicted values which were 7 to 15 percent higher than experimental. Fitting the data empirically gave
>
> $$C_m = \frac{0.080}{(s/a)^{1/6}\,\mathbb{R}^{1/4}} \tag{6}$$
>
> Regime IV, separate boundary layers: Relations for the moment coefficient and boundary layers thickness were established that take into account the influence of relative gap width. They are :
>
> $$C_m = \frac{C}{\mathbb{R}^{1/5}} \quad , \quad C = \Phi(s/a) \tag{7}$$
>
> $$\delta = \frac{A_4\, r}{\mathbb{R}_r^{1/5}} \quad , \quad A_4 = \Phi(s/a) \tag{8}$$
>
> C and A_4 were solved as functions of K and are given in references (7) and (8).

Picha and Eckert (23) performed an experimental study of the air flow between two coaxial disks. It was reasoned that if the flow in the core, i.e. the flow outside the boundary layers on the disk, was known, then the integrated momentum equations could be solved for boundary layer thickness and shear stress. The study was carried out with the aid of smoke injection as a flow visualization tool and with velocity measurements. Both shrouded and unshrouded disks were used. The disks were rotated also with arbitrary velocities. It was found that, when the disks were rotated with equal and opposite speeds, the core was stationary. Rotating the disks in the same direction results in a very stable core at the disk centerline. A study of the flow between two unshrouded disks rotating at the same angular speed indicated that the core consisted of a forced vortex at the inner radii and a free vortex at the outer radii. Other results indicated that the angular speed of the core relative to the angular speed of the disk is relatively constant over a wide range of Reynolds number. Large random velocities were also observed in the core when the disks were unshrouded.

Further studies were made by Welsh and Hartnett (37) on the same configuration used by Picha and Eckert. Velocity profiles in the boundary layer flow on the disks were obtained for the tangential and radial directions. Experimental correlation with the theory of Cochran (3) was obtained for laminar flow on both a single disk and opposed disks. Measurements in the turbulent boundary layers indicated the boundary layer thickness to be 50°/o thinner than predicted by von Kármán for the free disk case. A 1/7 power law was found to give a satisfactory fit to measurements of the tangential component in a turbulent boundary layer on the rotating disk.

Theodorsen and Regier (35) made experiments on a 24-inch diameter free disk. Transition to turbulence was deduced from a plot of the local drag coefficient, which in turn is related to the torque coefficient, as a function of the Reynolds Number. A sudden increase in the drag coefficient, indicating transition, is noticed at a Reynolds number, $\frac{\omega a^2}{\nu}$, of about 310,000. This value was confirmed with hot-wire measurements. A study was made of the effect of roughness on transition. Measurements indicated a maximum reduction of the transition Reynolds number to 220,000. An early onset of turbulence was best achieved by a high pressure air jet directed at the center of the disk. It is interesting to note that a Reynolds number, using the theoretical laminar boundary layer thickness, δ, as a length parameter, will have the value $\frac{\omega r \delta}{\nu} = 1440$ at transition. This is close to the value for pipe flow.

Further experiments on the problem of instability of a laminar boundary layer on a rotating disk are reported by Gregory, Stuart, and Walker (11). Their interest in flow about a rotating free disk was aroused because a very simple model of the three-dimensional boundary layer exists on the rotating disk. The China Clay method was used by them to visualize the transition to turbulence in the flow close to the disk surface. A system of vortices, having equiangular spirals for their axes, was observed in the zone of instability. This observation was correlated with a theoretical analysis of the nature of instability in the flow. A value of the transition Reynolds number of 2.8×10^5 was obtained.

Smith (29) also investigated the nature of instability on a smooth steel disk rotating in air. He obtained a value of the Reynolds number at transition of 3.1×10^5. This compares favorably with the values of 2.8×10^5 and 3.1×10^5 obtained by Gregory, Stuart, and Walker and Theordorsen and Regier respectively. Smith found the frequency of the disturbance leading to transition to be approximately a constant times the disk angular velocity and to occur for Reynolds numbers in a narrow range below the Reynolds number of transition.

Maroti, Deak, and Kreith (20) performed experiments using a plastic disk rotating between two stationary disks. Smoke injection and cotton tufts were used to visualize the flow. When the diameter of the stationary disks was greater than the diameter of the rotating disk a periodically fluctuating flow field was observed. A linear correlation of the fluctuation frequency with the disk speed was obtained. Axial spacing was observed to effect the variation of frequency with the disk speed.

B. STUDIES WITH THROUGHFLOW

It appears that the only paper available giving extensive theoretical treatment to net radial outflow is that of Soo (30) who obtained a solution for small throughflows in the laminar close-clearance case. He found the torque independent of the throughflow, and the radial pressure variation to be a function of $Q/s\omega r^2$.

Jimbo (13), using tapered disks, investigated the effects of net radial inflow on disk friction, and on radial distributions of pressure and of average tangential velocity. A simple theoretical solution showed an effect of tangential velocity at inlet but gave no effect of axial spacing. A limited amount of experimental data supported the latter finding of zero axial spacing effect but showed only fair agreement with the predicted magnitudes.

In a qualitative survey made as part of the present study, Daily and Arndt (6) observed periodic fluctuations by using smoke as the flow visualization tool. They found no periodicities below some finite speed (approximately 600 rpm for $s/a = 0.2207$ and 800 rpm for $s/a = 0.069$) and outside the range of throughflow rates of from 5 to 25 cfm. They deduced that the fluctuations, which had a frequency of about half the frequency of the disk revolutions, were associated with a cellular type of instability. Based on these observations unsteady flow measurements included in this report were made. The preliminary study also included a few velocity measurements which established that basically the same four flow regimes reported by Daily and Nece (7) were applicable with a small net throughflow present.

C. OTHER RELATED WORK

Reiner (25) in the course of investigating certain pumping phenomena and related stress-strain effects constructed a special <u>centripetal</u> air-pump consisting essentially of a rotating disk closely spaced to a stationary plate. With very close axial clearances (of the order of 0.02 to 0.50 mm) and at high speeds air was drawn in a <u>centripetal</u>

direction into the gap. He attributed this to non-Newtonian properties, that is that cross stresses resulted in reversal of the normal centrifugal radial pressure gradient. Taylor and Saffman (34) concluded it to be a compressibility effect which existed because of minute variations in the axial clearance due to manufacturing imperfections. Later investigations by Reiner (25a) and Taylor (in a lecture on his current research, MIT October 1963) indicate the effect may occur with incompressible fluids.

Such centripetal effects are not believed important in the experiments reported here since the axial clearance was large in all cases (1/8" greater).

Other related work includes the vast literature on three-dimensional boundary layers. A few items having special significance to the disk problem are included here.

E.S. Taylor (32) presents a general outline of the structure of a three-dimensional boundary layer and the two basic methods of causing skewing. He discusses the mechanism of separation also. Experimental results by Johnston (14) and Senoo (28) are cited as illustrations.

A more elaborate survey of the various solutions of skewed boundary layer flow is given by Cooke and Hall (5). In this paper the full boundary layer equations in orthogonal curvilinear coordinates are described, along with the corresponding momentum integral equations. Several examples of solution of these equations for laminar flow are given. A description of the analogy to the axially symmetric boundary layers is also explained. Such an analogy exists when the cross flow velocities are small compared to the main flow velocities. The inertia terms for the cross flow become small compared to the other terms in the equation for the main flow direction. This reduces the momentum equation in the main flow direction to that of the axially symmetric boundary layer.

Of particular interest is the description of the empirical techniques required for turbulent flow. Basically these methods involve making appropriate assumptions for shear stress, shape factor, and velocity profiles. Substitution of these expressions into the momentum integral equations will lead to a solution for boundary layer growth, from which the numerical value of shear stress can be determined.

A more thorough analysis of the calculation of a skewed turbulent boundary layer is given by Cooke (4). He explains in more detail the techniques as set forth in the paper by Cooke and Hall.

In a recent paper, Olsson (22) performed a successful calculation of the boundary layer on a stationary blade of an axial flow compressor. In this particular case the cross flow was small compared to the main flow and the momentum integral equations are greatly simplified.

III EQUATIONS FOR THROUGHFLOW BEHAVIOR

A. GENERAL

Of the two turbulent flow cases, Regime IV with two separate boundary layers and a rotating core between is the more prevalent. Except for very small clearances, Regime III with merged turbulent boundary layers will not occur. In this chapter wewill consider the effects of superposed radial throughflow on the steady state Regime IV shear stresses and pressure distributions.

The physical model used as a basis for an examination recognizes the interdependence of the boundary layers and the properties of the rotating core which separates them. The core corresponds to the "frictionless" freestream flow of a simple boundary layer, but being no longer independent the determination of its properties becomes of key importance. For enclosed disks without throughflow a satisfactory model is to treat the core as a solid body rotation. Measured radial-pressure distributions confirm this and the successful theoretical solutions use this model [e.g. references (8), (27)]. With throughflow, however, solid body rotation does not occur in the core. Pressure measurements have shown (6) that core rotation must be a function of radius if the model of separate boundary layers with a rotating core is to apply. Velocity profiles included in this report confirm this. As a consequence, the determination of relations giving K_r is a basic step since torque and the radial gradient of pressure depend on K_r. Thus the objectives are to express as functions of throughflow and Reynolds number

K_r = core tangential velocity $U/\omega r$ as a function of radius

M = torque on the disk

p_r = core pressure as a function of radius

B. APPROXIMATE EQUATIONS FOR CORE ROTATION

Simple relations for the case of separate boundary layers (Regime IV) with throughflow can be made if it assumed that the fluid enters without rotation at the inner radius and leaves at the outer radius with the angular momentum per unit volume $\rho K_0 \omega a^2$ which the zero throughflow rotating core possesses. We begin by making two additional assumptions:

(a) No variation in velocity over the width of the core.

(b) The percentage increase in disk shear torque with net throughflow Q is the same over the entire disk.

Using the subscript zero to denote quantities without throughflow we will approximate the ratio of torques (on two faces of the disk) at the same Reynolds numbers as

$$\left.\frac{M}{M_o}\right|_{a\,t\,r} = \frac{2\int_o^r \tau_{t_d}\, 2\pi r^2 dr}{2\left[\int_o^r \tau_{t_d}\, 2\pi r^2 dr\right]_o} \approx \frac{2\,\rho\,Q\,K_o \omega\, r^2 + \frac{1}{2}\, C_{m_o} \rho\omega^2 r^5}{1/2\; C_{m_o}\, \rho\,\omega^2 r^5} \qquad (9)$$

where

τ_{t_d} = shear stress at rotating disk

Q = net throughflow volumetric rate in the clearance apace on one side of the disk.*

By assumption (b)

$$\left.\frac{M}{M_o}\right|_{a\,t\,r} \approx \frac{\tau_{t_d}}{[\tau_{t_d}]_0} \qquad (10)$$

and we write

$$\frac{\tau_{t_d}}{[\tau_{t_d}]_0} \approx C_1 \frac{Q}{\omega r^3} + 1 \qquad (11)$$

$$= C_1 \frac{Q}{\omega a^3} \left(\frac{a}{r}\right)^3 + 1$$

In general C_1 depends upon chamber dimensions (axial spacing ratio in this case) and Reynolds number.

Now consider the two cases of low and high net throughflows.

---

*Note: Reference (6) used Q = total flow rate past both sides of disk.

For low throughflow rates make the additional assumptions

(c) The boundary layer thickness is primarily a function of r and can be represented by

$$\delta = C_2 \, r^{1/n} \tag{12}$$

both with and without throughflow

(d) The shear stress is described by the Blasius type power law relation

$$\tau_{t_d} = C_3 \, \rho \, W^{7/4} \left(\frac{\nu}{\delta}\right)^{1/4} \tag{13}$$

(e) Relative to the disk, the total velocity W can be approximated as

$$\begin{aligned} W &= [U^2 + V^2]^{1/2} \\ &= [(\omega r - K_r \omega r)^2 + V^2]^{1/2} \\ &\approx (1 - K_r)\omega r = \omega r - U \end{aligned} \tag{14}$$

Substituting Eqs. (13) and (14) into Eq. (11) gives

$$\frac{C_3 \, (1 - K_r)^{7/4}}{C_{3_0} (1 - K_o)^{7/4}} \approx C_1 \frac{Q}{\omega r^3} + 1$$

or for $C_3 \approx C_{3_0}$

$$\begin{aligned} \frac{(1 - K_r)^{7/4}}{(1 - K_o)^{7/4}} &\approx C_1 \frac{Q}{\omega r^3} + 1 \\ &= C_1 \frac{Q}{\omega a^3} \left(\frac{a}{r}\right)^3 + 1 \end{aligned} \tag{15}$$

In keeping with the assumed power-law boundary layers we can assume a Reynolds number effect that is represented by making C_1 proportional to $\mathbb{R}^{1/5}$, where $\mathbb{R} = \omega a^2/\nu$. The spacing ratio effect should be small so long as Regime IV type flow is well established. The equation can be represented in the general form

$$B\,(1 - K_r)^n = G\,\frac{Q}{\omega a^3}\,\mathbb{R}^{1/5}\left(\frac{a}{r}\right)^m + 1 \tag{16}$$

where B, m, n are constants and G depends on K_o.

Equation (16) gives K_r as a decreasing non-linear function of the <u>throughflow number</u>

$$\mathbb{T} = \frac{Q}{\omega a^3}\,\mathbb{R}^{1/5} \tag{17}$$

It is derived assuming low throughflows. For high throughflows it will not hold as it will give negative values for K_r. A relation which will give the same trends for low flows as Eq. (15) or (16) and allow extrapolation to high rates is

$$K_r = \frac{K_o}{C_1'\,\frac{Q}{\omega a^3}\left(\frac{a}{r}\right)^m + 1} \tag{18}$$

where C_1' is a function of Reynolds number and the exponent m is close to 3. In Section VI of this report the experimental data is represented approximately by replacing C_1' with $A\,\mathbb{R}^{1/5}$, where A = constant, and setting m = 13/5. With these substitutions and using the definition of Eq. (17) we write

$$K_r = \frac{K_o}{A\,\mathbb{T}\left(\frac{a}{r}\right)^{13/5} + 1} \tag{19}$$

In Eqs. (16) and (19) the effect of axial spacing does not appear explicitly. However, both relations are dependent on K_o, which depends in turn on spacing ratio s/a. Both theoretical and experimental values of K_o are known to decrease with increasing values of s/a. [See references (7) and (8)].

C. TORQUE

Torque as a Function of $\mathbb{T}$: Using Eq. (9) the percentage increase in torque with throughflow can be expressed as a function of the throughflow number $\mathbb{T}$ as follows:

From Eq. (9) for a disk of radius a

$$ {}^{o}/o\ \text{Increase} = 100 \times \frac{2\,\rho\, Q\, K_o\, \omega\, a^2}{1/2\; C_{m_o}\, \rho\, \omega^2\, a^5} $$

$$ = 100 \times \frac{4\,K_o}{C_{m_o}} \frac{Q}{\omega\, a^3} \qquad (20) $$

As presented in reference (6) using empirical values for C_{m_o} from reference (7, 8), namely

$$ C_{m_o} = \frac{0.102\ (s/a)^{1/10}}{\mathbb{R}^{1/5}} \qquad (21) $$

gives

$$ {}^{o}/o\ \text{Increase} = \frac{K_o}{0.0205} \frac{\mathbb{R}^{1/5}}{(s/a)^{1/10}} \frac{Q}{\omega\, a^3} \times 100 \qquad (22) $$

or

$$ {}^{o}/o\ \text{Increase} = 4860 \frac{K_o}{(s/a)^{1/10}} \mathbb{T} \qquad (23) $$

Torque as a Function of K_r: An alternate approach to the computation of the torque with throughflow is integrate the shear stress for the throughflow condition. This involves expressing the shear stress in terms of the boundary layer profile and hence in terms of the core rotation velocity. Solution then requires an expression for the core rotation K_r, preferably an explicit expression such as Eq. (19).

The torque on both sides of the rotating disk is

$$M = 2 \int_{o}^{a} 2 \pi r^2 \tau_{t_d} \, d r = C_m \frac{\rho}{2} \omega^2 a^5 \qquad (24)$$

The Blasius shear stress relation converted for use on a disk with a skewed boundary layer may be expressed as

$$\tau_{t_d} = \left[\frac{u_{rel}}{W} 0.0225 \, \rho \, W^{7/4} \left(\frac{\nu}{z}\right)^{1/4} \right]_{z \to 0} \qquad (25)$$

where

W = velocity relative to disk at a distance z from the disk

$= (u^2_{rel} + v^2_{rel})^{1/2}$ (26)

$u_{rel} = r\omega - u_{abs} = r\omega - r\omega \, [1 - \eta^{1/7} + K_r \, \eta^{1/7}]$ (27)

$v_{rel} = v_{abs} = v_o \, \eta \, 1/7 \, (1 - \eta)$ (28)

$\eta = \frac{z}{\delta}$ (29)

Assume that the boundary layer thickness δ depends only on core rotation and not on the net throughflow. The boundary layer thickness of skewed boundary layers on an enclosed disk without throughflow is known to be of the form

$$\delta = \alpha' f(1 - K_o) \frac{r}{\left(\frac{\omega r^2}{\nu}\right)^{1/5}}$$

[e.g. see references (7) (8) (27)]. Experimental results reported in reference (7) vary closely with $f(1-K_o) = (1-K_o)^2$. Letting $\alpha' = 0.526$, the coefficient used in (27), we write for the throughflow case

$$\delta = 0.526 \, (1 - K_r)^2 \frac{r}{(\omega r^2/\nu)^{1/5}} \qquad (30)$$

Assume now that the reference velocity v_o is nearly independent of core rotation and can be written as

$$v_o = 0.162\, \omega r \tag{31}$$

where the coefficient 0.162 again is that used in (27).

Now introducing Eqs. (26) to (31) into Eq. (25) gives for the disk surface shear stress

$$\tau_{t_d} = 0.0267\, \rho\, \nu^{1/5} \omega^{9/5}\, r^{8/5}\, (1 - K_r)^{5/4}[1+(\frac{0.162}{1 - K_r})^2] \tag{32}$$

Using Eq. (24) the torque coefficient can be written as

$$C_m = [\frac{0.663}{a^{23/5}\mathbb{R}^{1/5}}] \int_o^a r^{18/5} (1 - K_r)^{5/4}[1 + (\frac{0.162}{1 - K_r})^2]^{3/8} dr \tag{33}$$

In Eq. (33 C_m is a function of K_r which depends, in turn, on throughflow number $\mathbb{T}$ and spacing ratio s/a. If the relation for K_r is known C_m can be computed. As an example, Eq. (19) is used and the percentage increase in torque computed and compared with experimental values in Section VI. The program for the digital computer solution used is given in the appendix.

D. PRESSURE DISTRIBUTION

The pressure gradient dp/dr can be related to change in radial linear momentum flux. Assume that the principle momentum change occurs in the core. Then we may write

$$\rho\, r\, d\, r \frac{U^2 s}{r} + (\tau_{r_s} - \tau_{r_d})\, r\, d\, r - s\, r \frac{dp}{dr} dr$$

$$= \frac{d}{dr} (\rho\, r\, s\, V^2)\, dr \tag{34}$$

where τ_{r_s}, τ_{r_d} are radial shear stress components on stationary endwall and disk respectively, U, V are tangential and radial core velocities and s is the axial spacing between disk and endwall (see Figure 1).

Substituting $U = K_r \omega r$, $V = \frac{Q}{2\pi r s}$ and dividing by $\rho r s dr$

$$\frac{(K_r \omega r)^2}{r} + \frac{(\tau_{r_s} - \tau_{r_d})}{\rho\, s} - \frac{1}{\rho}\frac{dp}{dr} = \frac{1}{r}\frac{d}{dr}\left[\frac{1}{r}\left(\frac{Q}{2\pi s}\right)^2\right] \qquad (35)$$

Integrating from a to r

$$\int_a^r K_r^2\, \omega^2 r\, dr + \int_a^r \frac{\tau_{r_s} - \tau_{r_d}}{\rho\, s}\, dr - \int_a^r \frac{1}{\rho}\frac{dp}{dr}\, dr$$

$$= \int_a^r \frac{1}{r}\frac{d}{dr}\left[\frac{1}{r}\left(\frac{Q}{2\pi s}\right)^2\right] dr \qquad (36)$$

Note that

$$\int_a^r \frac{1}{r}\frac{d}{dr}\left(\frac{1}{r}\right) dr = \int_a^r \frac{-1}{r^3}\, dr = \frac{1}{2}\frac{1}{r^2}\Bigg|_a^r \qquad (37)$$

also

$$\int_a^r K_r^2\, \omega^2\, r\, d\, r = \frac{K_r^2 \omega^2 r^2}{2}\Bigg|_a^r - \cancel{\int_a^r \frac{\omega^2 r^2}{2}\, 2\, K_r\, \frac{dK_r}{dr}\, dr} \qquad (38)$$

Let the last term of Eq. (38) be approximately zero for low through-flow numbers. Then Eq. (36) becomes

$$\frac{p}{\rho}\Bigg|_a^r = \frac{K_r^2 \omega^2 r^2}{2}\Bigg|_a^r - \frac{1}{2}\left(\frac{Q}{2\pi r\, s}\right)^2\Bigg|_a^r + \cancel{\int_a^r \frac{\tau_{r_s} - \tau_{r_d}}{\rho}\, dr} \qquad (39)$$

Neglecting the last term in Eq. (39) we can rearrange to give

$$\frac{p_r - p_a}{\rho} = \frac{1}{2}\,(K_a \omega a)^2 \left[\left(\frac{K_r r}{K_a a} \right)^2 - 1 \right] + \frac{1}{2} \left(\frac{Q}{2\pi a s} \right)^2 \left[1 - \left(\frac{a}{r} \right)^2 \right] \qquad (40)$$

The rise in pressure between r = 0 to r = a which occurs when Q = 0 is

$$\frac{p_o}{\rho} = \frac{1}{2}\,(K_o \omega a)^2 \qquad (41)$$

Normalizing Eq. (40) by dividing by Eq. (41) gives

$$\frac{p_r - p_a}{p_o} = \left(\frac{K_r}{K_o} \right)^2 \left[\left(\frac{r}{a} \right)^2 - \left(\frac{K_a}{K_r} \right)^2 \right] + \frac{1}{K_o^2} \left(\frac{Q}{2\,\pi a^2 s \omega} \right)^2 \left[1 - \left(\frac{a}{r} \right)^2 \right] \qquad (42)$$

The first right hand quantity gives a component due to the rotary motion of the core. It depends on K_r and hence strongly on throughflow number $\mathbb{T}$. The second right hand quantity gives a component due to the radial "source" flow as measured by the <u>source flow number</u>

$$\bar{Q} = \frac{Q}{2\,\pi\, a^2\, s\, \omega} \qquad (43)$$

Symbolically, then, we can write

$$\left. \frac{p_r - p_a}{p_o} \right|_{\text{Total}} = \left. \frac{p_r - p_a}{p_o} \right|_{\mathbb{T}} + \left. \frac{p_r - p_a}{p_o} \right|_{\bar{Q}} \qquad (44)$$

All the terms in Eq. (44) will be negative quantities as the equation is written.

As in the case of the torque the solution of Eq. (42) requires an expression for K_r. Again, computations were made using Eq. (19) and are compared with experimental results in Section VI.

IV EXPERIMENTAL EQUIPMENT

A. GENERAL DESCRIPTION

General views of the test stand are given in Figs. 3 and 4. The basic equipment is essentially the same as that used by Daily and Nece (7,8) and consists of a bronze disk enclosed in a cylindrical housing of variable axial length. The disk is driven through a two-inch diameter stainless steel shaft by a 7 1/2 hp, 220 volt, 100 to 2200 rpm dc motor. Torques are measured by means of a strain-gage bridge bonded to the walls of a cavity in the disk and of the shaft.

For the study reported here modifications were made to the housing to permit circulation of a net throughflow. As described in detail in reference (6) provisions were incorporated for admission of fluid near the axis to the axial space between disk and endwall, for collection in a peripheral annulus and for uniform withdrawal from the annulus through eight exhaust ports. With these modifications a disk diameter of 18-1/8 inches was used leaving a radial clearance between disk tip and cylindrical wall of 1/16 inch. External circuits were provided for bringing equal amounts of fluid to each side of the disk. A schematic drawing of the test stand and the external circuit for liquid throughflow is shown in Fig. 5.

Instrumentation includes smoke flow visualization equipment, velocity probes, hot wire anemometry and strain gage excitation and recording equipment.

B. TEST STAND

Test Chamber: A section through the test chamber and details of the disk shaft assembly are shown in Figs. 6 and 7. The 1/8" annular clearance gaps for fluid withdrawal at the outer radius can be seen on each end of the cylindrical surface. Two throughflow inlets at the inner radius are shown also. The front and rear coverplates will accept different inserts so that the transition from axial to radial flow may be varied. Two geometries were used which are shown as A and B in Fig. 8. Initial experiments reported in reference (6) were performed with geometry B. Concern (later invalidated) that the sharp edged openings might be the cause of the large scale periodicities observed in the flow lead to the revision called geometry A. For both geometries all surfaces are smooth and all joints match without discontinuity.

The cylindrical wall of the test chamber is a machined bronze insert into a cast iron outer housing. The axial length of this ring insert spaces the coverplates which serve as endwalls. By varying the spacer ring thickness and/or the disk thickness various axial spacing-ratios may be obtained as given in Table 3.

TABLE 3

Axial Spacing Ratios

(Disk radius: $a = 9.0625$ inches)

Spacer Ring Length (inches)	1/4-Inch Disk Axial Spacing (inches)	1/4-Inch Disk Spacing Ratio s/a	1/2-Inch Disk Axial Spacing (inches)	1/2-Inch Disk Spacing Ratio s/a
0.750	0.250	0.0276	0.125	0.0138
1.500	0.625	0.0690	0.500	0.0522
2.500	1.125	0.1241	1.000	0.1103
4.500	2.125	0.2345	2.000	0.2207

For visual observations a 1-inch thick lucite cover plate served as the outer endwall. Ports of 1/32-inch diameter were provided for smoke injection and were located at the radii shown in Table 4a. The ports were inclined at 30° to the wall of the cover plate in the direction of rotation so as to minimize interference with the disk-induced flow.

Velocity surveys with pitot tube and hot wire probes were made using a bronze cover plate. The radial positions of the measuring tip of the probes are given in Table 4b.

Provisions for pressure measurements were made in both the transparent and bronze cover plates. The radial positions of piezometer holes (1/8 inch in bronze cover and 1/16 inch in transparent cover) are shown in Table 4c. Also 0.020-inch piezometer holes were provided in the spacer rings at the disk tip centerline to allow the measurement of a reference pressure in the 1/16-inch radial clearance space.

TABLE 4

Measuring Stations in Front Cover Plate

(Disk radius: a = 9.0625 inches)

	Radius (inches)	Radius Ratio r/a
(a) Smoke Injection Ports Transparent Cover: 1/32-inch ports at 30° to wall surface	4	0.441
	6	0.662
	8	0.883
(b) Probe Stations for Pitot Tubes and Hot Wires Bronze Cover	4.25	0.469
	5.875	0.648
	7.50	0.828
(c) Pressure Piezometer Holes Bronze Cover: 1/8-inch holes Transparent Cover: 1/16-inch holes	3	0.331
	5	0.552
	7	0.772
	9	0.991

Note: 0.020-inch holes also provided in spacer rings at disk tip centerline to measure pressure in 1/16-inch radial clearance space.

The two-inch stainless steel drive shaft is connected to the dc motor by means of a flexible coupling to eliminate vibration and is securely fastened by fixed-end pillow blocks to a fixed base on which the test chamber itself is mounted. These pillow blocks have a maximum runout of 0.001-inch and are bolted and pinned to their supports. In preparation for experimental measurements, the shaft was fixed in all three dimensions, and the housing was shimmed, adjusted, and pinned so that it was symmetrical with respect to the end of the shaft with a minimum deviation obtainable of 0.002-inch. The face of the bronze disk was then scraped until it mated perfectly to the end of the stainless steel shaft with a wobble of less than 0.002-inch for the 1/4-inch disk and 0.0015-inch for the 1/2-inch disk, and a deviation in tip clearance of 0.002-inch. The segmental spacers, rear cover plate, spacer ring and front cover plate, having tolerances of 0.001-inch, are then assembled respectively.

Throughflow Circuits: The throughflow arrangements for air consisted of an open circuit in which a turbine compressor supplied air through two separately metered lines to the two sides of the disk. By this means balanced flow rates were maintained into the two sides of the disk. Discharge from the exit annulus was through the eight ports into the atmosphere. The compressor was rated at 50 cfm at 20.8 inches of water. Flow metering was by 3/4 inch orifices. A large 1 to 10 inclined manometer and a precisely calibrated rotometer were used to calebrate the orifices in place. During testing the pressure difference across the orifices was read with inclined manometers arranged to give a reading error of less than one percent.

For the liquid throughflow circuit, a closed system was used since it eliminated problems of contamination, temperature, flow measurement, and pressurization. The system consisted of a pump, reservoir and air pressure supply, heat exchanger, two separate metering runs, valves and bypass lines for control of flow rate, various temperature wells and air bleeds, and a manifold to collect liquid from the eight spacer ring connections (see Figs. 4 and 5).

The pump was chosen to duplicate the range of throughflows obtained with air, and has a maximum capacity of 40 gpm at 100 feet. During a run, the reservoir was pressurized so as to maintain a constant pressure at the strain gage section which is necessary for calibration. During initial filling of the system, the reservoir was pressurized so that air could be removed from the system at all points. When actually running, the outlet from the pressurized reservoir was connected by means of valves and 1/4-inch tubing to eliminate surging to the inlet of the pump, since this was the region of lowest pressure. Care had to be taken that all air was removed from the system so that the water viscosity could be maintained. The heat exchanger was allowed to operate with the maximum cooling water possible since, for low throughflows and high rotating speeds the temperature rise of the water in one pass through the chamber was as high as $7^{\circ}F$, and a great deal of cooling water was needed to keep the temperature of the liquid in the test chamber constant.

The liquid coming from the heat exchanger was divided into two parts and passed through the orifices in the separate metering runs. By keeping tolerances small in the design and manufacture, a single calibration curve of Δh vs. Q was attained for both orifices so that the flow rates to the front and rear of the disk could be balanced, simply by adjusting the flow rate for equal Δh's. Coarse adjustment of the total flow rates could be made by a valve placed at the pump outlet, and fine adjustment by a valve placed in a pipe line which bypassed the disk itself. Flow rates to the front and rear of the disk were balanced by separate valves. The manifold and piping between it and the spacer ring were designed such that there would be equal head loss for all rates of flow in each of the eight connections to maintain a velocity distribution at the disk periphery that was axially symmetric.

C. INSTRUMENTATION

Torque Measuring System: The torque instrumentation was designed to provide an accurate measurement of torque on the disk with no correction for shaft, bearing, or slip ring being necessary [see references (7) and (8)]. Four SR-4 strain gages are bonded inside the shaft in a hollow section (Fig. 7) which is on the disk side of any seals or bearings. The strain gage bridge has four leads which run inside the shaft to two slip rings mounted outside the test chamber. The bridge is excited through two silver-graphite composition brushes by two 6-volt storage batteries in parallel (Fig. 9). The other two slip rings are used to obtain the bridge balance signal which is attenuated and fed to a dc galvanometer of 0.0028 micro amp/mm sensitivity. A modification was provided in the circuitry such that the slip rings could be bypassed, and a five-prong plug connection could be made directly to the bridge for calibration.

Because of the necessity to measure the difference in small signals, many precautions had to be taken in the calibration procedure. During preliminary calibrations, it was determined that changes in resistance of the slip rings themselves were sufficient to produce the bridge unbalance observed for different positions of the shaft. On the most sensitive scale used for torque measurement, the difference was 2 percent of full scale reading. Also, depending on the point at which the balance was made, the average reading displayed on the galvanometer for finite rotation might or might not correspond with the balance position of zero rpm. This occurrence was eliminated by fixing a point on the shaft where all balances for zero rotation were taken, and determining the correction necessary to have zero mean bridge balance for zero torque and finite rotation. This correction is known as the index correction. In order to have agreement between the bridge balance for zero rotation and finite rotation, the same pressure at the strain gage section was maintained.

It proved necessary also to make corrections for temperature variations at the strain gage cavity. Although the strain gages are mounted at 45 degree angles to the shaft axis to eliminate axial forces, the shaft may expand laterally with temperature and produce a spurious torque indication. Calibrations were performed to determine this temperature effect. The strain gages are located in a section of the shaft which is directly exposed to the fluid being circulated into the clearance space on the back side of the disk (see Figs. 6 and 7). Consequently, during tests the temperature of the fluid was used as the basis of applying temperature corrections.

The voltage of the battery at the time of the run was corrected for any change in strength since the torque bridge calibration, by multiplying the deflection due to torque by the ratio of the battery strength at calibration, to the battery strength at the time of the run. The calibration value was taken from the current through a fixed wirewound resistor read on the galvanometer. This is the battery strength correction.

The actual calibration of the strain gage bridge itself was made by attaching the disk and a lucite moment arm to the end of the shaft with the external casing in place, and placing a pure couple on the shaft through frictionless pulleys. Various couples were used until a full calibration of all scales was obtained for both increasing and decreasing weight. What first was thought to be a hysteresis loop turned out to be a stretching of the string used to hang the weights, which was replaced by wire. Of course, the biggest question mark in the entire calibration procedure is not whether the calibration itself is good, but that the bridge balance for zero torque stays the same for zero rpm and finite rpm.

Velocity Probes and Traverse Control Unit: Two velocity probes were used in this program. A directional tube for establishing total velocity vector orientation is a two-hole cobra probe with the tubes ground to an angle of 45° with the flow. A pitot-state-tube determines the local magnitude. These probes were indexed for direction and axial position by means of a traverse control unit. Photographs of a probe and of the arrangement when mounted in the control unit are shown in Figs. 10 and 11. Probes and traverse unit are described in detail in references (7) and (8) and briefly in the following.

The directional probe is a two-hole cobra probe with the tubes ground off at an angle of 45° with the flow. The velocity probe is of similar dimensions having two 0.0135-inch static pressure openings, one on either side of the impact hole. The distance of 0.105 inch from the tip to the static opening is three times the 0.035-inch diameter of the individual tubes at the tip. The relative dimensions of this tube are comparable to a standard Prandtl-pitot tube. Both probes were constructed as to be interchangeable in the traverse control unit.

The directional probe was calibrated in a 8 by 14-inch wind tunnel operated at standard conditions with a velocity of 100 feet per second. At that time, using an inclined manometer, the sensitivity of the probe was found to be 1/4 of a degree. However, using more sensitive pressure sensing equipment than previously used, the sensitivity was in some cases as high as 5 minutes of angle. Calibration of the pitot-static tube in a free surface water tunnel indicated a tube coefficient very close to unity. A coefficient of unity was therefore assumed throughout this investigation.

The velocity probe traverse control unit is so constructed that the tip of either the velocity or directional probe may rotate about a point. The entire unit containing the probe rotates in any one of three machined holes in the brass front cover plate, being held against the face of the plate by clamps. The inner face of the base assembly is flush with the inside surface of the cover plate. The assembly was rotated by a worm in a bracket which is mounted on the front of the cover plate. This bracket also held a 135° segment of calibrated plate from a surveying transit. A 1-minute vernier was mounted on another bracket attached to the body of the traverse control device. Axial motion was achieved using a knurled nut and spindle device. The end of the spindle was attached to the head block of the probe. The perpendicular distance of the probe from the face of the cover plate was measured with a dial indicator attached to the end of the traverse control unit. This indicator read to 0.001 inch. Each probe was set in its own teflon bushing through which it slid. This provided both lateral support and acted as a seal. Both teflon bushings were a press fit in the control unit. Angular alignment was provided by having the head block of the probes slide in a machined slot in the traverse control mechanism.

Velocity-Pressure Transducer System: The transducer used consists of a bellows-diaphragm pressure cell coupled to a Schaevitz Linear Variable Differential Transformer which produces 700 mv output for 10 inches of water pressure. The circuitry of the system is shown in Fig. 12. In operation excitation of the primary circuit was by a Hewlett-Packard Audio Oscillator at 7.4 volts and 1000 c.p.s. The output signal from the secondary coils of the transformer was first amplified 10 times by a Ballantine Decade Amplifier. The amplified signal was then rectified by a full wave rectifier constructed at the Hydrodynamics Laboratory. The resulting DC signal was read on a Leeds-Northrup Galvanometer, having a 100 millimeter scale and a sensitivity of 0.0028 microamperes per millimeter of deflection. By introducing different values of resistance into the galvanometer circuit various values of pressure will cause a full scale deflection.

Four scales were used in this test program, having the ranges of pressure (in inches of manometer fluid, specific gravity 0.812) of 0 to 0.03351 inch, 0 to 0.514 inch, 0 to 1.730 inch, 0 to 10.733 inches. This corresponds to a range of velocity in standard air of 0 to 10.9, 0 to 45.2, 0 to 78.4, and 0 to 195 feet per second. The calibration of the transducer was accomplished by simultaneously measuring static pressure with the transducer and a micro-manometer. The plot of pressure vs. galvanometer reading indicated the sensing device to be truly linear. Experimental scatter was less than 1°/o. This precision indicated that some confidence may be placed in the velocity measurements since velocity is proportional to the square root of the pressure.

Smoke Flow-Visualization: The equipment and procedures for visual observations are described in detail in reference (6). The smoke generator consisted essentially of an electrically heated stainless steel coil through which a mixture of filtered kerosene and air is fed to produce a dense, dry white smoke. Smoke injection into the disk clearance space was through the 1/32-inch ports at a 30° angle to the cover plate wall at the locations given in Table 4.

Hot Wire Anemometry: For measurements of flow unsteadiness a hot wire anemometer was used. It is a constant temperature type manufactured by Leslie T. Miller. The system consists of two transistorized units, a model M-5 hot wire amplifier and a Model L-3 linearizer, in the circuit shown in the schematic of Fig. 13. The amplifier contains the bridge circuit (of which the hot wire is one leg), a differential amplifier and a power amplifier. The linearizer contains two squaring circuits in series with an attenuator and dc offset between them. A plus 6 and minus 6 volt transistorized fail safe low ripple power supply is used to drive the two units.

The probe consists of a 0.109-inch diameter column to which two prongs (sewing needles) are attached as shown in Fig. 14. The prongs are spaced at 0.16-inch and 0.0015-inch diameter platinum wire spans the gap at their free tips. In construction the wire is copper plated with a 0.080-inch bare spot and then soldered in place with the bare spot centered between the needles. These probes were mounted in the same traverse control units used with the velocity probes. As shown, two configurations were used, For boundary layer measurements the wire was parallel to the disk to give directional sensitivity and to enable closer approach. For measurements of the large scale fluctuations in the core directional sensitivity was eliminated by mounting the wire normal to the disk.

With both units there are two types of adjustments possible. The first requires the removal of the transistors and the internal adjusting and locking of various components of the circuitry. These procedures are covered in the operating manual and are not included here. The other requires only the manipulation of certain exterior dials with simultaneous checks using a voltmeter, oscillator and oscilloscope. Figure 15a is a photograph of the hot wire control box with the controls labelled.

On the amplifier the only adjustment necessary is P2. This sets the amount of overheat on the wire. The values indicated on the scale are exactly twice the resistance of the wire which balances the differential amplifier and bridge. The scale is off by a factor of 2 because an extra 75 ohms resistor was soldered into the bridge to allow the bridge to operate with hot wires having a cold resistance of ≤ 13 ohms. The wires used throughout the experiment had a cold resistance of from 8 to 11 ohms. The amplifier is very stable and does not drift.

On the linearizer there are 6 external adjustments possible although in practics, for the same range of velocities, only three are made, i.e., P1, P3 and P6.

In the first and second squaring circuits, P1 and P5 respectively adjust the circuitry to produce a wave form of twice the input frequency. For these two circuits, P2 and P6 respectively adjust the dc output to provide zero volts output for zero input. Between the first and second stages there is an attenuator, P4, to prevent overloading the second stage. The external resistor P0 does the same thing for the first stage. The offset between stages one and two are adjusted by P3 to provide a voltage to null the output of the amplifier for zero velocity.

The hot wire was calibrated in terms of the mean-steady core velocity between disk and endwall. Conditions known from pitot probe traverses were reidentified from speed and radial pressure gradient measurements taken with the hot wire in place. This permited calculation of the core velocity as essentially equal to $K_r wr$. Calibrations produced a linear relation between core velocity and voltage output.

Analog Computing Equipment: The hot wire data were tape recorded and analyzed by analog equipment available in the M.I.T. Hydrodynamics Laboratory. The units employed and their functions are described in the following:

The recorder is a Precision Instrument PS-200A magnetic tape portable. It is an FM type which can record and reproduce with a frequency response from dc to a maximum of 10 KC for a speed of 60 inches per second. In our case we recorded and reproduced at 1-7/8 inches per second which a corresponding frequency response from dc to 312 cps. The instrument has six different speeds from 1-7/8 ips to 60 ips and an overall accuracy of 1^{o}/o of full scale.

The recorded data are reduced using a Technical Products Company TP 625 wave analyzer system. As indicated in the block diagram of Fig. 15b it consists of one TP 626 oscillator, two TP 627 analyzers (each with one TP 218 H 2 cps filter and one TP 218 D 50 cps filter), one TP 645 multiplier and one TPA 11526 (Moseley 135 R) X-Y plotter. This system is capable of producing a power density spectrum of one signal or the vector product of two separate signals. For the present work, only the power density spectrum was determined.

The first process in the analysis is to transform the random function from the time domain to the frequency domain, that is, to decompose the random function into its frequency components. This process involves the use of narrow band wave filters and may be accomplished by using the TP-627 analyzer. The second process is that of squaring the transformed function and the third process is averaging. For these two steps the multiplier is used. After these processes are carried out the power spectral density function is automatically presented on the X-Y plotter.

The TP-627 unit functions as a constant bandwidth (2 cps bandwidth was used in the present case) analyzer in conjunction with the TP-626 oscillator to determine the frequency (1 cps) and amplitude of the individual components of a complex wave within the frequency range of 2 to 25,000 cps. The multiplier produces the instantaneous square of the analyzer output, which is then averaged over a selected time of from 0.001 to 100 seconds. For this study an averaging time of 5 seconds was used.

5 Miscellaneous Equipment

A General Radio Type 1531-A Strobotac was used to determine the rotational speed of the disk. While performing a routine check of the instrument it was noted that, for some unexplained reason, it gave readings which were approximately 7-1/2 per cent higher than the true readings. Thereafter the Strobotac was used to "stop" the rotating shaft and the number of strob-light flashes counted using a photocell and a Hewlett-Packard digital counter. In this manner the rotational speed to an accuracy of better than one percent was easily obtained.

For the torque data the temperature was measured at four points in the throughflow circuit and at two points inside the housing. The thermometers used were fractional mercury thermometers whose smallest increments were 0.1° C.

In order to read the instantaneous mean velocity flow as indicated by the hot wire, a Hewlett-Packard 405C/CR automatic DC digital voltmeter was used. The voltmeter does not continuously monitor its input voltage and requires only about 0.2 seconds to make a single measurement. During the measurement time it zero-sets itself, makes a measurement, checks range, and if necessary, changes range. The 405C is capable of selecting its range and polarity automatically to display voltages from 100 millivolts to 999 volts to three significant figures and has a sampling control which determines the rate at which measurements are repeated. The accuracy of the instrument is 0.2°/o of reading +1 count.

V EXPERIMENTAL PROCEDURE AND DATA REDUCTION

A GENERAL

The experimental program included the four areas of disk friction torque, velocity profiles across the clearance space s and their variation radially, radial distribution of pressure and hot wire measurements of large scale unsteadiness in the rotating fluid. Each was determined as a function of rotating speed and throughflow for different axial spacings between disk and endwall.

The range of test variables for the several types of measurements are given in Table I on page 4 of this report.

The raw data were compiled and reduced in the following manner:

B TORQUE

Data Taking: The torque measurements included here were obtained using water. All data presented are for disk speeds of 300 rpm or greater where the disk friction torques exceeded 2.0 ft. lb. The corresponding lower limit for Reynolds number is approximately 2 x 10^6. Below this limit experimental errors existed which were attributed to thermal effects on the straingage cavity dimensions and consequent appearance of "apparent torques". As discussed in Section IV-C the temperature of the shaft was assumed to be equal to the temperature of fluid entering the back clearance space. At low torques a few degrees difference from equilibrium temperature values caused large percentage effects.

The majority of data were obtained by setting a speed and varying the throughflow up to a maximum and then down to zero in discrete intervals. This procedure was repeated for each speed and all s/a ratios. Before commencing a run, the following steps were taken:

(a) The system was bled of air, and the shaft rotated to an index mark.

(b) The throughflow pump and heat exchanger coolant pump were allowed to operate until all temperature stabilized as evinced by a constant temperature throughout the system.

(c) With either zero throughflow or for the throughflow set to the desired value, the bridge was balanced as closely as possible, and the galvanometer adjusted to zero after the pressure at the strain gage section was adjusted to 8 inches of mercury. This pressure was set at the 3-inch radius and maintain the same for all speeds and throughflows.

(d) The temperature of the strain gage section and of the exit fluid were noted as well as the galvanometer deflections for each scale to be used in the run (usually only one) for a zero throughflow, a mean throughflow and a maximum throughflow. A battery strength reading was taken using the most sensitive operating scale (scale 4) of the galvanometer.

The shaft was set in rotation and for each point in the run, the number of flashes per second corresponding to the required rpm was set on the strobotac and Hewlett-Packard counter light-cell combination, and the motor speed was adjusted until the shaft appeared stationary, indicating it was synchronized with the strobotac. The throughflow rate was adjusted to the proper value. During the run, any deviations from this fixed rpm and throughflow were corrected immediately.

Upon completion of the above steps, the following was obtained for each of the test points:

(a) The galvanometer reading.

(b) The temperatures at the chamber inlet, outlet, seven-inch radius, nine-inch radius, and strain gage section.

(c) Another torque rading after fine adjustment of rpm and Q. This is done to check for reading error, etc.

(d) A check of the galvanometer zero

(e) This procedure is then repeated for the next point.

Upon completion of a run, all steps of the initial procedure are repeated except that the bridge balance is not adjusted.

Torque Data Reduction: Averaging of the two readings of torque gives a value to which the bridge balance correction, the index correction, the temperature correction, and the battery strength correction may be applied. Corrections for bridge balance are taken as a linear change if there is any difference between the bridge balance before or after a run. The index correction is a constant for each scale, with the maximum correction being one mm on Scale 4. Temperature corrections are based on the change in temperature at the strain gage from that observed at initial and final balancing. The battery strength correction is simply a multiplicative factor which is the ratio of battery strength at time of calibration to battery strength at time of trial. After these corrections are made, the adjusted reading is used to compute the torque in foot pounds.

Using the thermometer reading at the exit as the liquid temperature, the values of $\mathbb{R}$, $\rho/2\ \omega^2 a^5$ and were computed. A gross moment coefficient was found by dividing the measured torque by $\rho/2\ \omega^2 a^5$. Subtracting a correction for friction at the disk tip, $C_{m_{tip}}$, from this value gave the net moment coefficient C_m for the two sides of the disk. The computation for $C_{m_{tip}}$ was based on the assumption of turbulent between the disk tip and the spacer ring. Using Darey-Weisbach friction factors by the method given in detail in references (7) and (8) the correction is expressed as a coefficient

$$C_{m_{tip}} = \frac{f \pi b}{8 a} \qquad (45)$$

where

a = disk radius
b = disk thickness
f = a function of $\mathbb{R}_p = 4.27 \times 10^{-3} \frac{\omega}{\nu}$

The experimental data are presented as curves of C_m versus Reynolds number for various throughflow rates and axial spacing ratios. The data are presented also as percent increase in torque coefficient versus dimensionless throughflow parameters. In general these percentages were evaluated from data taken all on the same day so errors in the torque differences due to variations in calibrations and other experimental factors would be minimized. The reference C_{m_o} for zero throughflow used to compute the percentages was obtained by linear extrapolation of plots torque versus throughflow back to zero throughflow. In most cases the agreement with measured zero-throughflow torque was good. In some cases the measured value was slightly higher or lower than the extrapolated. However, the extrapolation was adopted for the computation as giving the most consistant results.

C VELOCITY PROFILES

Data Taking: Before each test run the motor and electronic equipment were allowed to warm up for at least 1 hour. Oscillator output was adjusted to the required frequency and voltage. The transducer null was adjusted to as low a value as possible. This was accomplished by turning a knurled nut at the back of the instrument, moving the coils of the transformer relative to the core. At null position the transducer produced a net reading on the galvanometer for zero pressure differential. This reading was cancelled by changing the potential on one side of the galvanometer input with an auxilliary voltage source.

Each run consisted of two parts; a determination of flow direction and a measurement of the total velocity. First the directional probe was placed in the traverse control mechanism. The tip of the probe was brought as close as possible to the surface of the mechanism which is flush with the wall when installed. Careful measurement with a depth micrometer was made of the distance from the outer edge of the tip to the wall. Half the thickness of the probe is subtracted from this measured value, giving the distance from the wall to the centerline of the probe tip. This distance was set on the Ames dial at the other end of the control mechanism. In this manner the actual distance from the wall to the centerline of the probe may be read directly on the Ames dial. A minimum reading of 0.020 inch was attainable. The assembled traverse control mechanism, with probe in place was placed in a machined hole in the cover plate and rotated until index marks on the cover plate and the unit were lined up. This indicated that the probe was aligned in the tangential direction. The vernier plate in the protractor was then adjusted to read zero. Tygon tubing was used to connect the pressure taps of the probe to the pressure ports of the transducer. Readings of flow direction were taken at even increments of distance from the wall. At each setting the probe was rotated until a zero pressure differential was read on the galvanometer. The resulting angle of inclination was recorded. After every two or three readings, a check of the galvanometer zero reading was made by disconnecting the pressure leads to the transducer. The electronic circuitry remained exceptionally stable throughout this investigation and no corrections for drift were necessary.

The procedure used for the total velocity probe was essentially the same as for the directional traverse. At each point the probe was oriented at the measured angle obtained with the directional probe and the stagnation pressure read on the galvanometer. Care was taken to exactly reproduce the same rate of disk speed, throughflow, and fluid temperature as was used during the directional traverse. The procedure for reduction of data is given in the following section.

Velocity Data Reduction: The raw velocity data consist of the flow direction in degrees and a stagnation pressure reading in millimeters of galvanometer deflection. Since the pressure sensing system was linear, it was relatively easy to reduce the galvanometer reading to a value of total velocity. Thus, the total velocity was obtained by multiplying the square root of the galvanometer reading by appropriate constant. The value of velocity obtained was corrected for temperature since the temperature is the chamber was different from 60°F. A simple correction is obtained from the equation of state:

$$\frac{p}{\gamma} = h_{60} = (520)R \quad \text{(R is the gas constant)} \qquad (46)$$

$$h_t = RT = R[t + 460] \qquad (47)$$

where

t = temperature, ^{o}F.

Then

$$\frac{v_t}{v_{60}} = \frac{h_t}{h_{60}} = \frac{t + 460}{520} \qquad (48)$$

At temperatures of 80^{o} to 90^{o}, which were encountered during the test program, this correction amounts to from 2 to 3 $^{o}/o$. The total velocity was reduced to its tangential and radial components using the measured value of the skew angle, α. The tangential component is obtained by multiplying the total velocity by cos α, and the radial component by multiplying by sin α. The radial and tangential components of velocity were normalized with respect to velocity at the disk surface, ωr.

All the data areplotted as computed by the above procedure in sets of curves of the skew angle α, radial velocity $v/\omega r$, and tangential velocity $u/\omega r$ all versus the relative distance from the stationary end wall y/δ. These diagrams are useful for determination of general trends in flow circulation and core rotation. Within the boundary layers on the disk and endwall, however, the velocities computed directly from the probe readings are known to contain errors due to the finite size of the probe tip. Consequently in the analysis of the boundary layers the data was also examined for the effects of the shear field and boundary proximity on the probe response by estimating the displacement of the probes effective center. For this the method of Mac Millan (18) was used. Mac Millan's equation for the effective correction is

$$\frac{\delta c}{D} = \frac{\delta_1}{D} + \frac{\delta_2}{D} \qquad (49)$$

$$= 0.15 + f\,(z/D,\ u^{*}D/\nu) \qquad (49a)$$

where

δc = correction to distance z

D = probe tip diameter

z = distance from boundary to centerline of probe.

u^{*} = local friction velocity

In this relation the term $\delta_1/D = 0.15$ is the correction for shear field effect and is a shift always toward the higher velocity region. The term $\delta_2/D = f(z/D,\ u^{*}D/\nu)$ is the wall proximity effect and is a shift toward the wall. For flow past a stationary boundary and using a stationary probe, δ_1 and δ_2 are of opposite signs. For the moving disk and stationary probe, δ_1 and δ_2 are both shifts toward the disk. The corrections are given in the diagrams of Fig. 16 which are adapted from Mac Millan. In applying to the present experiments the friction velocity was approximated using the 1/7 power law relation

$$u^{*} = 0.15\ W^{7/8}\,(\nu/\delta)^{1/8} \qquad (50)$$

where

W = total velocity outside the boundary layer relative to the boundary

= approximately $(\omega r - K_r \omega r)$ for the disk

δ = boundary layer thickness defined by subtracting an estimated shear field effect D/2 from the thickness determined from the measured tangential velocity profile.

D. PRESSURE

Data Taking and Reduction: Comprehensive pressure measurements with air have been reported already in reference (6). In those air experiments the pressure p_r at radius r was measured with reference to an arbitrary datum. The data as measured were plotted versus $(a^2 - r^2)$ and extrapolated to $r = 0$ and $r = a$. The extrapolated value at $r = a$ then replaced the arbitrary datum pressure as the reference value giving $(p_r - p_a)$. All data were made dimensionless by dividing by the centrifugal pressure at $r = a$ due to core rotation for zero throughflow, namely $p_o = - \rho (K_o \omega a)^2/2$.

Further measurements using water were taken simultaneously with torque measurements. For these the pressure in the disk tip radial clearance space (see Table 4) was used as reference during measurement and for plotting data. These differences between disk tip pressure and the pressure at each of four other radii were obtained simultaneously on four separate mercury-water U-tube manometers. As for the measurements reported in reference (6) the raw data were plotted versus $(a^2 - r^2)$ for each value of Reynolds number and throughflow rate. Such a plot gives a straight line for zero throughflow. With throughflow a smooth curve results which allows extrapolation to $r = 0$. The data is finally represented in dimensionless form by dividing by the zero throughflow centrifugal pressure at $r = a$.

E. FLOW PERIODICITIES

Data Taking and Analysis: Visual observations with smoke injection apparatus and fluctuation measurements with hot-wire apparatus were obtained using air. In general the hot wire data were obtained by setting a value of throughflow and varying the disk speed with the hot-wire set at a particular position in the axial clearance space. Before starting a run the following steps were taken:

(a) The hot-wire circuit was balanced (see Section IV-c)

(b) Equal throughflow rates were established to both sides of the disk.

(c) The strobotac was adjusted to give a count on the digital counter corresponding to the disk speed.

(d) The reference frequency was set on the oscillator. This reference value was necessary in order to distinguish between the different points on the tape. (Two of the seven possible channels were used recording the signal and the reference frequency on the tape.

(e) The zero of the hot-wire circuit was checked for possible drifting.

The speed was then varied and for each speed the following data taken:

(a) A three minute tape record of the signal.

(b) Signal amplitude from a cathode ray oscilloscope.

(c) Digital voltmeter records of hot-wire output from which mean local velocity could be determined.

Throughout a test run checks were made of the disk speed and zero of the hot-wire circuit and any deviations from their fixed positions were corrected immediately.

After a run the tape recorder, which is portable, was carried to the wave analyzer system for analysis. The system, which had been allowed to warm up for at least two hours, was checked and adjusted to give the proper frequency response. The signal from the tape recorder was then fed into the analyzer and the gain of the analyzer set for 100°/o. Approximately two and a half minutes of the three minute tape was required by the analyzer to make a plot, from 0 to 30 cps, of the power density spectrum.

The graphs plotted by the analyzer are then studied and the peaks, indicating a concentration of power at that frequency, recorded. These peaks represent the frequency of the periodic fluctuations.

VI EXPERIMENTAL RESULTS

A. INTRODUCTION

In presenting the experimental results information on the mean steady velocity profiles and boundary layer growth will be discussed first. This is done because of their bearing on the proper understanding of core rotation and its relation to wall shears and pressure distributions in the axial clearance space.

It has been noted that two versions of the passage geometry at the inlet to the clearance space were used during the experiments (see Fig. 8 and Table I). Both were modifications of the simple, completely enclosing, right circular cylinder employed by Daily and Nece. As will be pointed out, some differences in flow features were obtained with the geometry changes. However, the effects of throughflow follow the same trends with each. As indicated in Table I a comprehensive set of velocity surveys was obtained for a very close clearance and a moderate clearance with geometry B. These data give a general picture of the throughflow effects and are presented in the following.

B. VELOCITY PROFILES AND BOUNDARY LAYER GROWTH - GEOMETRY B

General: Fig. 17 through 32 display the velocity distribution in the space between the disk and the stationary endwall obtained with geometry B. Reading from top to bottom on each plot the variation of skew, radial velocity, and tangential velocity are plotted versus the relative distance from the stationary endwall, y/s. The data for each particular combination of Reynolds number, rate of throughflow, and spacing are given on the same plot for three different relative radii, $r/a = 0.469$, 0.648, and 0.828.

Before discussing the data in detail a general survey will be useful. Note that without throughflow there is a net radial flow outward close to the disk and a net flow inward close to the wall. For the wider spacing a core exists with essentially zero radial outflow and a constant value of $u/\omega r$. This agrees with the concept of solid body rotation as set forth in the theoretical treatment of the problem. Note that the radial velocity increases rapidly close to the wall. Since the probe was thick compared to the boundary layer thickness it was not possible to get readings of velocity close enough to the wall to clearly define the peak of the radial velocity profile. It is important to note that this peak is very close to the wall. With an increase in throughflow the boundary layer is thickened on the rotating disk as shown in Fig. 28. This process continues with increasing throughflow until the boundary thickness varies inversely with radius, which is displayed in Fig. 30. Note that when there is a net flow through the system, a reduction of the tangential components of velocity occur in the core. This is also true for the close clearance flow. The largest reduction in tangential velocity occurs at the inner radius. It is this reduction in core velocity with increasing throughflow that is the mechanism for the observed decrease in radial pressure gradient. Equation (16) which was derived assuming 1/7 power law velocity profiles expresses the core rotation in the form

$$B(1 - K_r)^n = G \frac{Q}{\omega a^3} \mathbb{R}^{1/5} (\frac{a}{r})^m + 1$$

This relation indicates K_r must decrease as Q increases. Similarly, K_r must decrease as r decreases. This is exactly what is observed. Moreover, as we shall see, by varying the powers m and the coefficients B and G the above equation can represent the experimental data. The important fact to be gleaned from this is that a simple theory base on pipe flow data for shear stress is able to predict the trend. It would then be logical to believe that the tangential velocity profile may be expressed in terms of a 1/7 power law. Fig. 37 illustrates that to a rough approximation this is true. The velocity relative to the disk has been plotted dimensionlessly as a function of the dimensionless distance z/δ from the disk. However, it is important to note that the Reynolds number is still rather low and the velocity distribution does not follow a definite power law. With increasing throughflow, and hence increasing turbulence, the data tend to more closely follow the expected 1/7 power law. At the outer edge of the boundary layer the data for all rates of throughflow do roughly follow a 1/7 power law.

Regime III - $s/a = 0.0138$, $\mathbb{R} = 2.95 \times 10^5$: Before discussing results with the small spacing we should emphasize the fact that the clearance, s, is 0.091 inch and the probe thickness is 0.035 inch. This will certainly lead to errors due to local acceleration of the flow around the probe. However, the data indicate the difference between close clearance and separate boundary layer flow.

Reference should be made to Figs. 17, 19, 21, and 23. The first thing that meets the eye on inspection of these Figures is the fact that flow is definitely of the close clearance type, i.e. the boundary layers on the rotating disk and stationary endwall are merged. No core flow exists.

Inspection of the radial profile for zero throughflow in Fig. 17 indicates that greater radial outflow and radial inflow velocities exist at the inner radii. In other words, the radial velocity does not appear to be a unique function of y/δ, where δ in this case is one half the clearance space, s/2. Further, it appears from the radial velocity plots that the amount of fluid circulating is a constant from the inner to the outer portion of the disk, i.e. it is the same magnitude out on the disk and in at the endwall. If we assume $v = F(z)$ to be the same except for a constant then it is readily seen that for a constant rate of flow, Q, the normalized radial velocity, $v/\omega r$, must vary inversely as the radius squared, i.e. $\frac{v}{\omega r} \sim \frac{1}{r^2}$. Examination of the profiles will show this to be true. This is exactly opposite to what is found for the large spacing and is also contradictory to the present approximate theory.

The superposition of a low rate of throughflow, Q = 6.2 cfm, influences the flow field to a great extent. This is shown in Fig. 19. Note that at r/a = 0.469, the radial velocity profile closely resembles that for pipe flow. At this point the radial velocities are very large in comparison to the tangential components. With increasing radius the velocities decrease as would be expected, but the peak of maximum radial velocity shifts closer to the disk with increasing radius. A reduction in the tangential component of velocity at the center of the clearance space is evident. This reduction is greatest at the inner radius. Steeper velocity gradients result on the disk and lesser velocity gradients at the stationary wall.

An increase in the throughflow rate to 25.6 cfm [Fig. 21] results in a significant change in the flow. There is no radial flow inward anywhere in the chamber. The radial velocity profile at r/a = 0.469 resembles that of fully developed pipe flow. With increasing radial distance the point of maximum radial velocity shifts towards the disk surface. A further reduction in the tangential velocities outside the boundary on the rotating disk is also evident. At r/a = 0.469, $\frac{u}{\omega r}$ is reduced to zero outside the rotating disk boundary layer. Note also that the boundary layer has thickened considerably. Further scrutiny indicates that the boundary layer thickness appears to decrease with increasing radius. Computations of boundary layer thickness which appears later in this discussion indicate that this trend may be predicted theoretically. It should be mentioned at this point that throughout this investigation the boundary layer thickness of the radial profile always appeared to be greater than for the tangential profile. In other words when there are imperceptible gradients of velocity in the tangential direction there are perceptible gradients in the radial direction.

A further increase in throughflow rate to 52.0 cfm brings about even further change in the flow field, as shown in Fig. 23. Note that there is a still greater increase in the tangential velocity gradients on the rotating disk. However, the mechanism for the increased gradient is now a decrease in the boundary layer thickness, since the velocity outside the boundary layer is already zero. The radial velocity profiles resemble those for pipe flow throughout the clearance space between the rotating disk and the stationary endwall. Note that the peak of the profile still tends towards the rotating disk with increasing radius.

The data indicate, as would be expected for close clearances and low disk speed, that the effect of throughflow is of paramount importance. With no throughflow a circulation exists with outward flow at the disk and inward flow at the wall. The quantity of flow circulated appears to be a constant with radius indicating negligible axial flow except close to the axis of rotation and close to the disk periphery where the flow must change direction. With throughflow superposed this circulation is disrupted. There is indication that an axial flow now exists over the whole disk since the peak radial velocities approach the disk with increasing radius.

$\underline{\text{Regime III - } s/a = 0.0138,\ \mathbb{R} = 6.9 \times 10^5}$: In conjunction with this portion of the discussion, reference should be made to Figs. 18, 20, 22, and 24.

When there is zero net throughflow a close clearance type of flow exists such that the boundary layer thickness is constant at s/2. There is a similar circulation of radial flow as was observed at the lower Reynolds number. Note that again the rate of flow is the same over the disk and roughly of the same magnitude as for $\mathbb{R} = 2.95 \times 10^5$. Since velocity measurements could not be made any closer to the disk, it is difficult to judge the actual magnitude of any circulation flow. One discrepancy that exists is the fact that the tangential components of velocity are not similar. It would be supposed from the theory for this Regime III type flow that the profiles would be similar, having a velocity of $1/2\omega r$ at the center of the space between the disk and the wall. Note however, that there is a reduction in the centerline velocity with decreasing radius. Although all precautions were taken to entirely seal the housing in which the disk rotates when taking data for zero throughflow, the tangential velocity profiles correspond to those expected if there were a slight amount of fluid pumped through the system. If such a leakage occurred it could not be detected through examination of the radial velocity profiles.

The introduction of a low rate of throughflow, 6.4 cfm, produces a reduction in the tangential components of velocity outside of the boundary layer on the rotating disk. As previously mentioned Eq. 15 predicts this reduction of tangential velocity.

Inspection of the data for higher rates of throughflow will indicate other interesting features of this problem. Note that at Q = 23.7 cfm in Fig. 22 that there is no radial inflow close to the stationary wall. The radial velocity profile is not symmetrical, with the point of maximum radial velocity occurring close to the disk. Further reduction in the tangential components of velocity is also evident as would be expected.

Further increase in the throughflow rate to 51.2 cfm produces some interesting changes in the flow field as shown in Fig. 24. At r/a = 0.469 the radial velocity profile has the appearance of that observed for pipe flow. With increasing radius the profile flattens out and the point of maximum velocity shifts closer to the disk surface. This phenomenon is not a function of the geometry. Reference to Fig. 33 where the velocity data obtained for zero disk speed is plotted, will show that within reason the velocity profile is symmetrical at all radii. Therefore this shifting of the radial velocity profile with increasing radius has to be associated with the influence of the rotating disk.

It is interesting to note that a 1/7 power law may be deduced for the tangential component of velocity, even though there is not sufficient velocity data in the boundary layer. This may be inferred from the fact shown in a later section that the shear stress on the disk is apparently predicted from the Blasius expression for shear stress, from which in turn a 1/7 power law may be deduced.

Regime IV - $s/a = 0.069$, $\mathbb{R} = 2.95 \times 10^5$: The data for these conditions are given in Figs. 25, 27, 29 and 31.

First we note that with zero throughflow the profiles are similar. The boundary layer thickness is a constant over the disk. Such a situation is typical of laminar flow. Figures 35 and 36 compare the radial and tangential velocity profiles respectively with the theoretical laminar flow profiles on a free disk. Figure 35 shows the similarity of the radial profile with the theory of a free disk. There is a rather large experimental scatter when $z/\delta < 0.2$. In this particular case this corresponds to a distance of about 0.02 inch from the disk. When compared with the probe thickness of 0.035 inch, the experimental scatter is not an unexpected result. The important point to observe is that the radial velocities are of the same magnitude.

For the free disk the variation of the tangential component of velocity, which gives rise to the radial secondary flow, varies from 0 to ωr through the boundary layer. The equivalent variation through the boundary layer on the enclosed rotating disk is from $K\omega r$ to ωr. Therefore it would seem reasonable that the secondary flow would vary in a different fashion. On Fig. 36 the non-dimensional tangential velocity component relative to the rotating disk, $[1 - (u/\omega r)]/[1 - K_r]$, is plotted as a function of the relative distance through the boundary layer, z/δ. The theory for a free disk, due to Cochran, is also plotted on the diagram. For the free disk the normalized velocity relative to the disk reduces to $[1 - \frac{u}{\omega r}]$. The agreement is only fair, for the data seem to indicate a steeper velocity gradient near the wall than for the theory. As was the case with the radial profile the experimental scatter is large close to the wall. However, with appropriate corrections to the data to account for the discrepancy that the velocity appears to fall to zero at some distance from the wall, it would seem that the free disk profile is a fair approximation to the observed velocity distribution for the enclosed disk.

It is interesting to note at this point that laminar flow type boundary layers at this high a Reynolds number is not in agreement with the observation made with a smoke tracer. The smoke injection studies indicate that transition to turbulence should occur somewhere between $r/a = 0.648$ and 0.828 where the local Reynolds number, $\frac{\omega r^2}{\nu}$, is 1.24×10^5 and 2.03×10^5 respectively. The flow, however, appears to be laminar over the whole disk. As discussed in reference (6) the comparison of observed transition points using smoke tracers on the disk with the instability points reported in reference (11) for a free disk lead to the conclusion that the beginning of turbulence seen with smoke was actually the instability point triggered by the turbulent smoke jet. This is shown in Fig. 37 where the points of observed transition are plotted on a diagram of a/s vs. the local Reynolds number. For a/s = 14.5 the experimental observation is at $\mathbb{R}_L = 1.3 \times 10^5$ which corresponds to approximately $r/a = 0.648$. If the dotted curve on the same diagram is used, which is the experimental curve shifted to correspond with the observed point of transition as found by Gregory, Stuart, and Walker (11) on a free disk, a value of the local Reynolds number of 2.4×10^5 is deduced. The flow, therefore, should be laminar at the three radii of velocity measurements. All this seems to indicate that the probe has less effect on the transition to turbulence in the boundary layer flow than does a fairly high velocity jet of smoke. In some slight fashion this correlates with the observations of Theodorsen and Regier on a free disk (35). They noticed that a jet of air had a greater effect on transition to turbulence than did the addition of roughness protrusions on the surface of the disk.

Further inspection of Fig. 25 for zero throughflow will indicate that the boundary layer thickness on the stationary wall is approximately twice that on the rotating disk. The actual value predicted by Daily and Nece (7) is $\theta/\delta = 1.70$. This is certainly fair agreement. Another point to be made is the typical hump in the tangential velocity profiles. This hump is not predicted by the theory, but has been observed previously (7). Another fact that should be brought out at this point is that if the velocity profiles are similar and the boundary layer thickness is constant, then the radial flow in the boundary layers increases with increasing radial distance. Similarly the flow inward on the stationary wall decreases with decreasing radius. This leads to the conclusion that there must be an axial flow towards the disk over the whole disk area.

As shown in Fig. 27 the introduction of a low rate of throughflow, Q = 6.2 cfm, produces a distinct change in the flow pattern. This was also evident in the smoke studies reported in reference (6). Note that the boundary layer thickness has remained constant over the whole disk, suggesting that flow is still laminar. There is a radial flow outward in the core at $r/a = 0.469$. At $r/a = 0.648$, however, all radial flow outward is in the boundary layer on the rotating disk. The amount of radial inflow is also significantly greater with increasing radial distance. It must therefore be deduced that an axial flow toward the disk occurs at the outer radii. A typical reduction in the tangential component of velocity in the core is evident as Eq. (15) predicts. However, at this low Reynolds number there is no quantitative agreement with the expressions. At this point flow is still laminar in the boundary layer and no agreement with a theory based on turbulent flow should be expected.

An increase in the rate of throughflow to 25.7 cfm produces an even greater reduction in the tangential component of velocity in the core. This is shown in Fig. 29. The greatest reduction from that at the lower rate of flow now occurs at $r/a = 0.648$. A reduction in the core rotation to close to zero at $r/a = 0.469$ has already occurred with a lower rate of flow. An increase in the boundary layer thickness is evident indicating that the flow has become turbulent. The maximum radial velocities still occur close to the disk. A radial inflow exists at the outer portion of the stationary wall with no inflow being observed at $r/a = 0.469$. Therefore an axial flow towards the disk over the outer portion of the disk appears to be present.

The effect of increasing the flow rate to Q = 52 cfm is shown in Fig. 31. Backflow along the stationary wall has essentially disappeared.

It is interesting to note in passing that the periodic fluctuations observed and discussed in a later section disappear at approximately the same rate of throughflow at which the radial inflow creases. The radial profile now approaches that of pipe flow. However, the point of maximum radial velocity occurs closer to the disk with increasing radius. The core rotation is essentially zero throughout the chamber as the tangential velocity profile plotted in Fig. 31 indicates. The velocity profiles are characteristic of turbulent flow.

Observation of the velocity field at this spacing and Reynolds number permits several conclusions to be made about the flow. A laminar flow exists at Reynolds number as high as 3×10^5. This laminar flow can exist even though there is a turbulent flow in the core. An axial flow in the core moving towards the disk apparently exists for all rates of radial outflow. This is different from what is deduced for flow in close clearance.

Regime IV - $s/a = 0.069$, $\mathbb{R} = 6.9 \times 10^5$: The velocity profiles for this spacing and disk speed are plotted in Figs. 26, 28, 30 and 32.

The difference in the boundary layer flow at the higher disk speed is evident. Boundary layer thickness increases with increasing radial distance, which is the expected result for turbulent flow. The boundary layer on the disk at zero throughflow is approximately 50% thicker than predicted theoretically. This comparison is made in Table 5. When the dimensionless tangential velocity relative to the disk, $[1 - (\frac{u}{\omega r})]/[1 - K_r]$, is plotted versus the relative distance, z/δ, through the boundary layer, it becomes evident that the velocity profiles are similar at the outer radii. Such a correlation is made in Figs. 38 and 39 where the data are presented as measured by the velocity probe, and in Fig. 40 where the data have been corrected for the effective center of the probe. In the latter z_c is the corrected distance from the disk surface which was computed using the method of Mac Millan (18) as described in Section V-c. The curves in all three figures show that for $z/\delta > 0.3$ to 0.4 the agreement with a 1/7 power law is very good. For $z/\delta < 0.3$ there is a deviation from the 1/7 power law. Measurements of the boundary layer on a free disk made by Welsh and Hartnett (37) follow a similar pattern. The profile observed at $r/a = 0.469$ is not similar to that observed at the outer radii. This is to be expected since the local Reynolds number at this point is 1.52×10^5, indicating that a zone of transition or laminar flow is present at this point.

Fig. 40 also shows directly how the profile changes with local Reynolds number $\mathbb{R} = (\frac{\omega r^2}{\nu})$. At $\mathbb{R}_r = 1.5 \times 10^5$, the flow is distinctly laminar, while at $\mathbb{R}_r = 6.7 \times 10^5$, it is turbulent and closely follows a 1/7th power law. At $\mathbb{R}_r = 2.9 \times 10^5$, the point usually taken as the transition from laminar to turbulent flow, the profile is of intermediate form indicating that this $\mathbb{R}_r$ for transition is approximately correct.

As was indicated by the flow visualization study [reference (6)], the superposition of a low rate of throughflow, as shown in Fig. 28, has little effect on the mean flow pattern when the disk rotation is high. A significant radial inflow is evident along the stationary wall. All radial outflow including the net flow through the disk chamber is in the boundary layer at the rotating disk. Note that a significant reduction in core rotation is already evident. It is this reduction in core rotation which is the mechanism for the decrease in the pressure gradient with increasing throughflow.

Besides the reduction in core rotation, the rate of throughflow has a noticeable effect on the boundary layer growth. An interesting effect is shown in Fig. 30, where Q = 25.7 cfm. Note that the boundary layer thickness decreases with increasing radius.

Another observation to be made at this spacing is the persistance of a radial inflow even when the net rate of flow through the system is high. The amount of backflow decreases with decreasing radius, again indicating an axial flow in the core towards the disk. The influence of the rotating disk is also evident in the shifting of the point of maximum velocity towards the disk with increasing radius.

It is interesting to note that at high Reynolds numbers a 1/7 power law approximately satisfies the observed velocity distribution in the tangential direction. An approximation of the observed boundary layer thickness is possible using the theory developed for separate turbulent boundary layers and zero throughflow. A prediction of the observed change in core reduction is possible using momentum principles and a shear stress expression developed for pipe flow. Such conclusions should be useful in the design of turbomachinery where turbulent flow is prevalent.

Boundary Layer Growth on Rotating Disk: The boundary layer development is primarily a consequence of the tangential shear component. Only small effects are observed in the radial velocity profiles. Therefore, the significant thickness is measured by the location where the tangential velocity departs from the care tangential velocity. Of course, it is this layer which is most directly related to wall shear and disk friction torque. Relations providing good predictions of the growth of the tangential layer were given by Daily and Nece (7,8) for the Regime IV case of enclosed disks with zero throughflow. These were based on power law velocity profiles and are of the form

$$\frac{\delta}{r} = \frac{Y'}{\left(\frac{\omega r^2}{\nu}\right)^{1/5}} \qquad (51)$$

The coefficient Y' is shown theoretically, and confirmed experimentally, to be a function of the core rotation. As we have seen in the previous paragraphs the effect of superposed throughflow on the tangential velocity profiles is primarily a modification of the core rotation. The general form of the profile is preserved. This suggests that the same type relation for the thickness δ may apply if the coefficient is appropriately adjusted to account for core rotation with throughflow. This possibility is examined by considering the boundary layer on the rotating surface using the following procedure.

For zero throughflow the coefficient in the above equation (designated as Y' for the disk) is tabulated[*] in reference (7) as a function of core rotation K_o. Applying the equation to cases with throughflow the coefficient is assumed to be the same function of K_r as Y' is of K_o. The resulting computed values for the case of $s/a = 0.069$ and $\mathbb{R} = 6.9 \times 10^5$ are shown in Table 5.

Also shown in Table 5 are experimental thicknesses δ as determined from the measured profiles, first without correction and then including a correction for the shear field and wall proximity by the method of Mac Millan (18) described in Section V. The table shows reasonable agreement between the experimental values and those computed by the above procedure.

Using the data in Table 5 a diagram showing how the boundary layer grows with radius can be constructed. This is shown in Fig. 41 as dimensionless thickness $\delta\, \mathbb{R}^{1/5}/r$ versus core relative velocity $(1-K_r)$. Also shown are curves of the theoretical turbulent boundary layer of Daily and Nece (7,8) according to Eq. (51) and curves for $\delta\, \mathbb{R}^{1/5}/r = 0.526\,(1-K_r)^2$ and $0.40\,(1-K_r)^2$. In general, the experimental data test follows the trend given by $0.40\,(1-K_r)^2$. The fit is better after correction for the displacement of the effective center of the probe. The theoretical relation of Daily-Nece deviates at high values of $(1-K_r)$, i.e. at very low values of K_r, which corresponds to increasingly high throughflow rates. Otherwise this relation holds quite well also.

---

[*] Y' in Table 2, p. 39 of reference (7).

TABLE 5

Boundary Layer Computations - Rotating Disk

$s/a = 0.069 \qquad \mathbb{R} = 6.9 \times 10^5$

				Theoretical				Experimental			
								Uncorrected		Corrected Shear and Wall Effects	
Q	$\mathbb{T} = \left(\frac{Q}{\omega a^3}\right)\mathbb{R}^{1/5}$	r/a	$\mathbb{R}_r \times 10^{-5}$	K_r	Y'_r	δ/s (s/a=0.0665)	δ (inches)	δ (inches)	$\frac{\delta\,\mathbb{R}_r^{1/5}}{r}$	δ (inches)	$\frac{\delta\,\mathbb{R}_r^{1/5}}{r}$
0	0	0.469	1.52	0.367	0.156	0.101	0.061	0.07	0.179	0.06	0.154
		0.648	2.90	0.42	0.139	0.110	0.060	0.10	0.138	0.09	0.124
		0.828	4.74	0.42	0.139	0.127	0.077	0.12	0.219	0.11	0.200
3.3	0.010	0.469	1.52	0.207	0.249	0.161	0.097	0.10	0.256	0.09	0.230
		0.648	2.90	0.357	0.163	0.127	0.077	0.098	0.208	0.09	0.192
		0.828	4.74	0.410	0.143	0.127	0.077	0.11	0.200	0.10	0.182
13	0.040	0.469	1.52	0.038	0.485	0.315	0.190	0.20	0.51	0.19	0.48
		0.648	2.90	0.189	0.267	0.209	0.126	0.12	0.255	0.11	0.234
		0.828	4.74	0.341	0.169	0.154	0.093	0.12	0.22	0.11	0.202
26	0.079	0.469	1.52	0.038	0.485	0.315	0.190	0.16	0.410	0.15	0.380
		0.648	2.90	0.081	0.406	0.320	0.193	0.16	0.349	0.15	0.327
		0.828	4.74	0.200	0.254	0.234	0.141	0.16	0.292	0.15	0.274

Note: $s/a = 0.069$ is nominal value; for these tests actual value is $s/a = 0.0665$.
All values of $\mathbb{R}$ Q $\mathbb{T}$ are nominal.

C. CORE ROTATION

The velocity profiles described in the previous section have demonstrated that with throughflow core rotation velocity ratio is always a function of radius, i.e. $K = K_r$, and that it decreases with increasing throughflow rate and decreasing radius as predicted by the elementary theory which resulted in Eq.(15). This equation should not be expected to hold exactly since it is based on the assumption that the boundary layer growth remains substantially unchanged with throughflow. We have seen this is not the case. Never-the-less it is instructive to examine the core rotation data in the frame work of the relations.

Figures 42 to 44 show core rotation measured with geometry B plotted in the form of log-log diagrams of the Eq. (15) relation

$$\left\{ \left(\frac{1 - K_r}{1 - K_o}\right)^{7/4} - 1 \right\} \text{ versus } \frac{Q}{\omega r^3}$$

for the higher Reynolds number, $\mathbb{R} = 6.9 \times 10^5$. Although Eq. (15) was developed for the Regime IV condition of separate turbulent boundary layers, data for both Regime IV and the close clearance Regime III are included. The latter for $s/a = 0.0138$ is shown in Fig. 42 where K_r is obtained from the tangential velocity profile using the value at the midpoint of the clearance space. Fig. 43 is for $s/a = 0.069$ also obtained from the velocity profile data. Fig. 44 is for $s/a = 0.0552$ for which K_r was determined from a single velocity measurement at the midpoint of the clearance space.

In Fig. 42 for the close clearance, the data for the largest radius, $r/a = 0.828$, and the lower throughflow rates are correlated well by a relation of the form of Eq. (15). This is surprising since a rotating core does not exist. The data plots linearly with a slope of unity for $Q/\omega r^3$ less than about 0.015. The line is represented by

$$\left(\frac{1 - K_r}{1 - K_o}\right)^{7/4} - 1 = 55 \frac{Q}{\omega r^3} \qquad (52)$$

At smaller radii and hence larger values of $Q/\omega r^3$, the left hand term is proportional to $Q/\omega r^3$ raised to the power 0.386.

In Fig. 43 for $s/a = 0.069$ which gives Regime IV type flows, the data for the intermediate and inner radii, $r/a = 0.648$ and 0.469, with the lower throughflow rates are represented by

$$\left(\frac{1 - K_r}{1 - K_o}\right)^{7/4} - 1 = 43\,\frac{Q}{\omega r^3} \qquad (53)$$

In this case the left hand term is proportional to the 1.308 power of $Q/\omega r^3$ for the largest radius $r/a = 0.828$.

The results in Fig. 44 for $s/a = 0.0552$ are similar to those for $s/a = 0.0552$. The rotation at $r/a = 0.648$ is given by

$$\left(\frac{1 - K_r}{1 - K_o}\right)^{7/4} - 1 = 40\,\frac{Q}{\omega r^3} \qquad (54)$$

At $r/a = 0.828$ the left hand term is proportional to the 1.27 power of $Q/\omega r^3$.

In Section III an alternate relation for core rotation was expressed by Eq. (19), namely

$$K_r = \frac{K_o}{A\,\mathbb{T}\left(\frac{a}{r}\right)^{13/5} + 1}$$

In Fig. 45 the experimental results for the two cases $s/a = 0.0552$ and $s/a = 0.069$, both for $\mathbb{R} = 6.9 \times 10^5$ are shown plotted as K_r/K_o, versus the throughflow number $\mathbb{T}'$. Here K_r is the value determined from measurement and K_o is the ideal value 0.5. It is seen that the data plot approximately as hyperbolas which agree with the form of Eq. (19). On the same diagram theoretical curves are drawn for which the factor A in Eq. (19) was chosen to be 12.74. This value of A provides a good match with the experimental data at the middle radius $r/a = 0.648$. The experimental points are slightly greater than the theoretical at $r/a = 0.828$ and smaller at $r/a = 0.469$.

Actually the zero throughflow values of K_o are less than the ideal value by amounts depending on the chamber geometry and s/a ratio (as will be discussed shortly). Using smaller K_o values will raise the ratio K_r/K_o which is computed from the measured K_r values. Then in fitting Eq. (19) the constant A would be less than 12.74. For example, a $10^{o}/o$ decrease in K_o would reduce A by approximately $15^{o}/o$, when $r/a = 0.828$.

D. GEOMETRY EFFECTS - COMPARISON OF A AND B

The influence of the throughflow inlet geometry (A and B in Fig. 8) are shown in Figs. 46 and 47 where velocity traverses with geometry A are compared with the geometry B results discussed in the preceeding paragraphs. Two cases are shown, one for zero throughflow and one for Q = 3.35 cfm. The profiles at the top of each figure are for radial velocities v, while those at the bottom are for tangential velocities, u. Plotting $u/\omega r$ and $v/\omega r$ (where ωr is the disk velocity) against y/s (the relative distance from the stationary endwall) gives dimensionless graphs.

The main difference to be seen from these figures is a reduction in tangential velocity for both Q = 0 and Q = 6.7 cfm when geometry A is used. This is shown by the following tabulated values taken from the curves.

TABLE 6

Geometry Effects on Core Rotation

	Q = 0		Q = 3.35 cfs	
	K_{o_A}	K_{o_B}	K_{r_A}	K_{r_B}
r/a = 0.469	0.3	0.38	0.13	0.21
0.648	0.33	0.42		0.37
0.828		0.42	0.32	0.42

The trend with throughflow is the same, that is K falls below K_o and becomes K_r, a pronounced function of radius, as throughflow is established. There is a small effect on the disk boundary layer thickness δ, which would be determined from the tangential velocity profile, with geometry B giving a slightly smaller value.

The radial velocities show very little effect. In the wall region, especially near the stationary wall there appears to be a slight reduction in radial velocities. However, this difference is judged to be within the experimental accuracy of the measurements.

The absence of marked differences in mean velocity profiles and boundary layer thicknesses suggest that no major effect on unsteady fluctuations would be encountered. This proved to be the case. The same fluctuating flows observed with geometry B and reported in reference (6) were obtained with geometry A. These will be discussed in later paragraphs.

E. TORQUE

As indicated in Table 1 torques were measured with water at spacing ratios s/a = 0.0138, 0.0276, 0.069, 0.1241. In general the data were obtained on a grid of Reynolds numbers versus throughflow. The Reynolds numbers covered the range from about 2 x 10^6 to 10^7 and throughflow (one side of disk) from 0 to about 0.045 cfs. The corresponding throughflow number Π ranged from zero to 0.06. The three larger spacings resulted in Regime IV flow with separate boundary layers. Regime III flow occurred with the narrowest spacing. All these water measurements were made using the throughflow inlet geometry A shown in Fig. 8.

Zero Throughflow Measurements: The zero throughflow measurements were compared with previous conclusions from reference (8). This comparison provided an overall check of the measuring system. Figure 48 shows the information on a diagram of C_m versus Reynolds number. The present data are shown as test points. The previous results are represented by curves using the formulae derived in reference (8). For Regime III the reference curve is Eq. (16) the empirical relation from (8). Regime III is an uncertain region of operation and Eq. (16) was published only as the best fit for a small sample of data. The present data are approximated by Eq. (6). For Regime IV Eq. (7), the theoretical relation derived in (8), was used to compute reference curves for the s/a ratios of the present tests. Measurements from (8) were higher than the theoretical value by 6.7, 4 and 2 percent for s/a = 0.0278, 0.069 and 0.2411. The present data are higher than the theoretical Eq. (7) by 7, 4.5 and 1 percent for the same three s/a values respectively. Consequently, the agreement with earlier measurements is good.

The measurements of reference (8) were made with a passage geometry essentially that of B in Fig. 8, while the present measurements were with geometry A. The agreement of results indicates no major effect of geometry on the zero throughflow disk torque even though the geometry affects the core rotation. The measured torque is the intergrated value over the entire disk, but, never-the-less, is determined principally by the shear stress on the outer 10 to 15 percent of the disk radius. This is the region most affected by the flow circulation over the cylindrical portion of the enclosure and the region where the core rotation would be least affected by geometry changes near the axis.

Effect of Throughflow: Figures 49-52 show the torque coefficient C_m for constant throughflow rates Q versus Reynolds number. Each diagram is for one s/a ratio. These diagrams all show a systematic increase in C_m as Q is increased. This increase is dependent on spacing ratio and throughflow number as discussed in the following.

For one s/a ratio and a fixed disk speed the measured torque increase was practically linear with throughflow rate Q for $Q > 0$. A typical case is shown by the best-fit straight line in Fig. 53. From such plots the ratio $\Delta M/\Delta Q$ was determined graphically for each s/a and disk speed. Figure 54 shows this ratio plotted versus disk speed. On this basis the torque increase is slightly dpendent on spacing ratio by a percentage that seems to decrease with increasing disk speed.

For further analysis the percentage increase in torque coefficient was determined. In evaluating the experimental increase the zero throughflow coefficient was based on the torque given by the intersection of the best-fit straight line with the $Q = 0$ axis on plots such as Fig. 53. The percentage increases thus determined are plotted versus throughflow number $\mathbb{T}$ in Fig. 55.

Two methods of computing torque increases for correlation of experimental results have been presented in Eqs. (23) and (33). In both the major parameter is the throughflow number $\mathbb{T}$. In Eq. (23) an effect of s/a is represented since its development incorporated the equation for the zero throughflow moment coefficient which is dependent on s/a. In Eq. (33) the s/a effect does not appear explicitly but enters to the degree that K_r depends on s/a.

Figure 55 shows an overall correlation with $\mathbb{T}$. In addition there is evidence of a secondary effect of spacing ratio s/a. Considering the Regime IV data we see that for each s/a the points fall into a zone. Within the zone there is some divergence with speed (and hence Reynolds number) but in general the data for a fixed s/a can be represented by a single line. This suggests a relation of the form of Eq. (23). However, Eq. (23) predicts values that are too large in magnitude. Moreover, the effect of s/a is not given accurately by $(s/a)^{1/10}$. Empirically, the data in Fig. 55 is represented to within ± 5 percent by the relation

$$^{o}/o \text{ Increase} = 1390\, K_o \frac{\mathbb{T}}{(s/a)^{1/8}} \qquad (55)$$

where K_o is the theoretical value of K for $Q = 0$ as taken from reference (8) and listed below

TABLE 7

Values of zero-throughflow Core Tangential Velocity Ratio, K_o

[Reference (8)]

s/a	K_o
0.0276	0.475
0.0690	0.45
0.1241	0.42

Lines computed from the above equation are shown for s/a = 0.0276, 0.069 and 0.1241.

In Fig. 55 the s/a effect for the Regime IV cases causes approximately a 20 percent change in the increase over zero throughflow torque between s/a equal to 0.0276 and 0.1241. Ignoring the s/a effect the data can be represented to within ± 20 per cent of the increase magnitude by the relation

$$^{o}/o \text{ Increase} \approx 880\,\mathbb{T} \qquad (56)$$

We should note as an example here that the increase at $\mathbb{T} = 0.035$ is of the order of $30^{o}/o$ of the zero throughflow coefficient C_{m_o} and a $20^{o}/o$ variation of increase is only $6^{o}/o$ of C_{m_o} .

Data for the Regime III case obtained with s/a = 0.0138 are not represented by Eq. (55) which was derived for Regime IV conditions only. Moreover, they show more scatter and no definite trends of s/a or speed effects are discerned. However, as they fall in the midst of the Regime IV points Eq. (56) will represent the Regime III conditions also.

On Fig. 55 there is also a theoretical surve of percent increase computed from Eq. (33). To evaluate Eq. (33), K_r was expressed by Eq. (19)

$$K_r = \frac{K_o}{A\,\mathbb{T}\,(\frac{a}{r})^{13/5} + 1}$$

with $A = 12.74$ and $K_o = 0.5$, the same value used to match the equation to the core rotation data. Since K_o contains the only dependence on s/a the use of a single value eliminates this effect from the computation. The single line shown deviates from the empirical straight line relation and gives higher magnitudes until the throughflow number becomes large. The use of actual K_o values, which are about 10 percent less than 0.5, will shift the curve closer to the experimental results in the range of the bulk of the data. Reducing the constant A in accordance with the reduced K_o as discussed in connection with core rotation would also give this effect as well as modifying the curvature of the theoretical line.

F. RADIAL DISTRIBUTION OF PRESSURE

In reference (6) pressure measurements were reportet for a range of disk speeds and throughflow rates and several axial spacings using air. Samples of data are reproduced in Figs. 56 to 67 where the dimensionless pressure $(p_r - p_a)/p_o$ is shown as a function $(1 - r^2/a^2)$. These curves were obtained by plotting values for the pressure measuring stations and extrapolating to zero radius $[(1 - \frac{r^2}{a^2}) = 1.0]$. On these diagrams the 45° line represents the parabolic distribution of solid body (forced vortex) rotation. The results are interpreted as follows:

(1) For zero throughflow the pressure varies with radius parabolically.

(2) Except at very low disk speeds (Reynolds numbers) or very small axial clearances, throughflow causes the tangential whirl to decrease so that K becomes K_r a function of radius and dp/dr is reduced from the forced vortex. This "regular" behavior is illustrated clearly in Fig. 58. Deviations from this regular behavior occur in Figs. 56, 57 and 59.

(3) For very large throughflow velocities, as occur with very small s/a, the effect of the radial velocity can be overriding and the pressure gradient tends toward that expected for a frictionless source flow. This is the case for $s/a = 0.0138$ and $\mathbb{R} \leq 4.8 \times 10^5$ as shown in Figs. 56 and 57.

(4) For very low disk speeds, even very small throughflow rates will essentially eliminate the tangential whirl. When the radial velocities are also small no perceptible radial pressure gradient will be observed. This would be the case illustrated by $s/a = 0.0276$ at the low $\mathbb{R} = 1.7 \times 10^5$ in Fig. 59

The motion in the rotating core is essentially some combination of a vortex and a radial source flow and the theoretical expression of Eq. (42) describes the two effects. In Eq. (42) the first right hand term can be considered the contribution of a vortex component as modified by throughflow from a simple forced vortex of angular velocity $K_o \omega$. The second term gives the contribution of the source flow component. As the throughflow number increases the magnitude of the first term becomes smaller (absolute value) so that the departure from the forced vortex pressure distribution becomes greater. As the source flow number $\bar{Q}$ increases the second right hand term becomes larger (absolute value). Since $\bar{Q} = Q/(2\pi a^2 s \omega)$ the small axial spacings contribute to a more pronounced source flow effect.

Plots of the terms in Eq.(42) [using the symbols of Eq. (44)] are given in Figs. 68 to 70. Figure 68 is the first term for several values of $\mathbb{T}$ ranging from zero to 0.18. For $\mathbb{T} = 0$ the distribution is that of a forced vortex. Figure 69 shows the second term for source flow numbers $\bar{Q}$ ranging from zero to 0.2. For $\bar{Q} = 0$ there is no contribution. For $\bar{Q}$ finite and $r = 0$ the solution has the singular point. Thus, as $r \rightarrow 0$ high negative values are computed. Combining both terms of Eq. (42) will lead to a of diagram for each throughflow number of the type of Fig. 70 which is for the particular throughflow number $\mathbb{T} = 0.09$.

It will be noted that the curves in Fig. 68 are similar to the "regular" curves of measured pressure distribution shown, i.e. those for which the throughflow influences the core rotation K_r but has not become the predominant effect . Behavior of the type observed for large $\bar{Q}$ values in Fig. 56 is modelled in Fig. 70. As we have seen, the source flow effect was important only for the narrower spacering and lower disk speeds in the air tests. For all the other air data and for subsequent water data the magnitude of $\bar{Q}$ was small enough to have little effect on the distribution except possibly near the axis where the curves shown in Figs. 56 to 67 were obtained by extrapolation.

A comparison of experimental data with the theoretical Eq. (42) is shown in Fig. 71 where the quantity $(p_r - p_a)/p_o$ is plotted versus throughflow number $\mathbb{T}$ for one radius $r/a = 0.331$. The theoretical curve is computed using Eq. (19) with $A = 12.74$ and $K_o = 0.5$. Moreover, since all but a few of the experimental conditions involved values of $\bar{Q}$ small enough to give negligible effects the term due to source flow in Eq. (42) was omitted in computing the theoretical curve. The experimental data includes results from air tests (Figs. 56-67) which were made with geometry B (Fig. 8) and also data from water and air tests using geometry A. If is seen that the average curve of all the experimental data follows the form predicted by Eq. (42). However, the magnitude is different. Eq. (72) compares the theoretical and measured values for $r/a = 0.663$ and 0.883 with similar results.

In Fig. 71 differences due to the passage geometry do not show up in the experimental data. In Fig. 72 there is a trend for the geometry A data to show slightly lower magnitudes of $(p_r - p_a)/p_o$. This is consistent with the lower core rotations observed with geometry A.

G. UNSTEADINESS AND PERIODICITIES

Previous studies (6) using smoke-tracer flow visualization disclosed the existence of periodic unsteadiness for certain throughflows and rotating speeds. It was found that over a certain range of throughflows periodic fluctuations occurred. When inject smoke was observed with a Strobtac flashing at a frequency slightly different from the fluctuation frequency the smoke streakline appeared as a trail whipping out and curling back on itself. The analysis of observations for a wide range of throughflows and disk speeds with several axial spacings lead to the conclusion that a cellular vortex system was being observed. This system apparently was compared of several vortices moving in a circular path about the rotating axis at some fraction of the disk speed. For a clockwise rotation of disk a vortex would have a counter-clockwise sense about an axis perpendicular to the disk. Since the existence of a cellular type instability in axial spaces has special consequences in various kinds of machinery, its origin and more quantitative confirmation of its characteristics are important.

Geometry Effects: During the flow visualization studies, observations were made of the "scale" of the turbulent eddies or vortices making up the apparent cells by examining the fluctuations along a streakline. It was found that the scale was always larger with increased throughflow. One possible source of such an instability is flow separation where the throughflow emerges into the clearance space from the annulus at the shaft. With the geometry B (Fig. 8) employed for those studies, separation at the sharp corner of the annulus seemed quite possible. Consequently, a new inlet designated as A in Fig. 8 was designed to minimize this possibility. With the new geometry in place and operating under Regime IV conditions with $s/a = 0.069$ smoke visualization studies were repeated using air to answer the questions.

(1) Do the fluctuations still exist?
(2) If the fluctuations still exist, are the affected by the changed geometry?

The same kind of unsteadiness was observed with the new geometry. Photographs comparing the smoke streaklines for the same throughflow and disk speed obtained with the new geometry A and the old geometry B are given in Figs. 73 and 74. Using the same procedure as employed in reference (6) fluctuation frequencies were observed with a Strobotac. A comparison with the geometry B data taken from Fig. 21 of reference (6) is shown by the lower set of plotted points in Fig. 75.* It appears that not only are the fluctuations similar in the two cases but they are quantitatively the same. The two geometries are quite different and it appears that the observed instabilities are not dependent on the particular geometry of the inlet passages.

---

*Note that in Figs. 75, 76, 77 Q is given for two sides of the disk.

Hotwire Measurements of Unsteadiness: Quantitative measurements were continued with air using the hot-wire anemometer. The tape recorded data was analyzed as described in Section V-E give power density spectra like the example in Fig. 78.

Data were taken generally at a distance measured from the stationary endwall of y = 0.540 inches. This position near the outer edge of the disk bounded layer was in the zone of maximum fluctuations. At smaller y the fluctuations were the same frequency but contained less energy. Measurements were made for Q = 0, 1.6, 2.4 and 4.9 cfm, each for 11 speeds rangings from 300 to 2000 rpm. This set of throughflows was selected to include the range of no periodicities at lowest flows and to carry well into the range of stable periodicities as had been indicated by the observations in reference (6).

For $Q \leq 1.6$ cfm no distinct concentrations or peaks occurred in the power density spectra. For $Q \leq 2.4$ cfm distinct frequencies of energy concentration were observed. In general one predominant peak appeared. At frequencies below the main peak other lesser spikes occurred in some records as shown in Fig. 78. In most cases a higher frequency peak of small magnitude occurred which was of the same frequency as the disk speed. This is shown by the upper set of plotted points in Fig. 78. In addition, these disk speed frequencies were observed over the full half width of the gap, y = 0.300 to 0.605 inches at radii of 4.25 and 7.5 inches. It was concluded that the disk speed frequency probably indicated the existence of an imperfection or a wobble in the disk motion although measurements showed a disk wobble of less than 0.0075 inches at the 4.25 inch radius. Most of the data were taken at y = 0.540 inches which is near the edge of the disk boundary layer.

As throughflow or radius increases, the periodicity is obscured by increasing turbulent signals. This agrees with the visual observations reported in (6) that periodicities were distinct only for $Q < 13$ cfm and for the two inner smoke port radii of r = 4 and 6 inches. No periodicities were observed at the outer port of r = 8 inches.

The lower frequency peaks which occurred below the main peak (as mentioned above) were at 8 and 11 cps and were independent of disk speed, throughflow rate and probe position (both radial and axial). Investigation showed the same frequencies present when both the disk drive and throughflow blower were not operating but all other machinery and equipment were operating for taking signals in the normal way. It was concluded that these two frequencies were not connected with the observed periodicities. Moreover, the several agreements between the visually observed findings and the hotwire probe findings were gratifying. It was concluded that the presence of the probe had not destroyed the basic large scale periodic unsteady motion which the experiment sought to investigate.

From visual observations it was not clear whether the periodic fluctuations occurred primarily in the core flow or extended into the boundary layers. The construction of the hotwire probe prevented traversing the boundary layer on the stationary disk but a surveys were made from the center of the core to within 0.005 inches of the disk (from $y/s = 0.49$ to $y/s = 0.99$). The predominant frequency was found well into the disk boundary layer. The amplitude also increased as the boundary layer was penetrated.

As was found from the smoke observations, the frequencies of the periodic eddy motion observed with the hotwire varied linearly with disk speed but at different rates in lower and upper speed ranges. This is shown in Figs. 76 and 77 which are diagrams for the same s/a and same throughflow at $r/a = 0.469$ and 0.648. In reference (6) the postulated cellular system was a simple case which assumed an integral number of vortices translating in a circular path about the rotating shaft, probably at the velocity of the core fluid. For this model the linear frequency-speed relation was written in reference (6) as

$$f = n\,K'\omega + \text{constant} \qquad (57)$$

where

n = an integral number

ω = disk speed

K' = some fraction of disk speed

Differentiating we get

$$\frac{df}{d\omega} = K'n \qquad (58)$$

By this relation if K' is the core velocity ratio and the same function of r as K_r, $df/d\omega$ should increase with radius. The quantity $df/d\omega$ is the slope of the frequency-speed lines in Figs. 76 and 77. Comparing the two figures we see that $df/d\omega$ does not increase with radius. Approximate values are given in Table 7.

TABLE 7

Slopes of the Frequency-Speed Plots

Figures 76 and 77

	Q	Slope: $df/d\omega$ Low Speeds	High Speeds
$r/a = 0.469$ ($r = 4.25''$)	2.4	0.55	0.75
	4.9	0.52	0.75
$r/a = 0.648$ ($r = 5.875''$)	2.4	0.42	0.70
	4.9	0.46	0.80

In the high range of speeds the slopes for the two cases are close to being the same. In the low range the apparent trend is toward smaller slopes at the larger radius. This would indicate a constant or decreasing K' which is inconsistent with vortices moving at the core fluid velocity. Conversely estimating core velocities for inlet geometry B using Table 6 (B applies to Figs. 76 and 77) the computed number of cells is not the same for the two radii in either the lower or higher speed range. From visual observations, the two different slopes did not appear to signal a change in characteristics of the fluctuations. As a consequence, it is clear that the elementary model is incomplete. It is believed that the periodicities are influenced by the three-dimensional character of the system as a whole, including the boundary layers. This view is supported by fact that the fluctuation frequencies were measured in the boundary layer as well as in core, and that the amplitudes increased in the boundary layer. In fact, this, combined with the lack of effect of changing passage geometry, suggests the periodic motion is initiated by an instability in the boundary layer region.

The two slopes for the low and high speed ranges in Figs. 76 and 77 do indicate a change in the basic structure. By the elementary cellular model a jump in the number of cells is indicated. For Fig.76 the ratio from low to high speed is approximately 2:3. For Fig. 77 it is 4:3.

A qualitative view which emerges from these considerations begins with instabilities in the boundary layer periodically occurring in time and in angular position on the disk and endwall. Such disturbances would tend to be translated at less than the mean velocity in the core. Three-dimensional circulations would carry a disturbance into the core and impart the radial velocity component observed in the smoke streaklines.

VII CONCLUSIONS

In summary the conclusions from thus study are the following:

Geometry Effects: The inlet flow passage geometry affects the mean velocity characteristics by reducing the velocity of the rotating core and affecting the boundary layer thickness δ to a small extent. The geometry changes did not show a measureable effect on the disk torque which is due to an integration of shear stresses over the full surface of the disk. The pressure measurements showed no definite effect of the change of geometry other than that due to the reduced core rotation velocity. Periodic fluctuations as observed by smoke tracer technique exist and have the same general characteristics with both geometries tested. This leads to the conclusion that the inlet geometry is not the basic cause of the unstable motion.

Velocity Profiles and Core Rotation: The three-dimensional skewed boundary layer profiles occurring with zero throughflow persist in their general form with throughflow. The boundary layer thicknesses can be approximated closely by the relations developed in references (7) and (8) if they are evaluated using the core velocity obtained with throughflow. The core rotation angular velocity ratio K is reduced from the zero throughflow value K_o when throughflow is established. It becomes, also, a function of radius K_r with dK_r/dr greater at the smaller radii. For low throughflow rates the core rotation can be expressed as a function of the throughflow number $\mathbb{T}$ by an equation of the form

$$B(1 - K_r)^n = G\,\mathbb{T}\left(\frac{a}{r}\right)^m + 1 \qquad (16)$$

Alternately the approximate relation

$$K_r = \frac{K_o}{A\,\mathbb{T}\left(\frac{a}{r}\right)^{13/5} + 1} \qquad (19)$$

gives the form of the experimentally determined variation quite. No pronounced effect of s/a on K_r was observed.

Torque: The disk torque coefficient was found to increase with throughflow. The percent increase is approximately linear with throughflow number $\mathbb{T}$ divided by $(s/a)^{1/8}$. To within ± 20 °/o of the increase, the percentage increase is directly proportional to $\mathbb{T}$. The coefficient computed from Eq.(33), which includes assumed 1/7 root boundary layer profiles and the approximation of Eq. (19) for $\mathbb{T}$, does not give a linear increase of the torque increment with $\mathbb{T}$. The theoretical relation can be made to approximate the measured data in the low $\mathbb{T}$ range by another choice of the constant A in Eq. (19).

Pressure Distribution: Using the core rotation K_r from Eq.(19) in the radial momentum Eq. (42). The pressure distribution radially as measured at the endwall shows evidence of two influences: a source flow (radial flow) effect and a rotation (tangential velocity) effect. Equation (42) derived from the radial momentum equation using Eq. (19) for K_r describes these two effects theoretically. The experimental data follows the form of the theoretical expression but with different magnitudes. For a small effect of source flow component (the case for the great bulk of the experiments here) the theoretical expression gives a single line. The data for both air and water follow the trend of this line but with different magnitudes.

Periodic Unsteadiness: Hotwire measurements show predominant frequencies in the range of throughflows beginning with $1.6 < Q < 2.4$ cfm and extending up to about $Q = 13$ cfm. This is approximately the range in which periodicities are observed visually. Additional extraneous frequencies occur at 8 and 11 cps and at the disk speed frequency which do not appear to be associated with the visually observed fluctuations. The predominant frequencies increase linearly with speed, but at different rates in low and high speed ranges. As throughflow rate Q increases and radius r increases periodicities are obscured by general turbulence in the signal. Neither are they observed visually for high Q and outer radius. The fluctuation frequencies are observed in the disk boundary layer as well as the core and the fluctuations increase in amplitude with increased speed and as the boundary layer is penetrated. The two ranges of linear variation of frequency with disk speed are similar to the findings from visual observations, but the slope $df/d\omega$ apparently depends on radius. The latter is inconsistent with the simple cellular model proposed in reference (6). The overall conclusion is that the elementary model is incomplete and the vortex motion is highly three-dimensional. The periodicity probably originates inside the boundary layer, translates about the shaft at less that the mean velocity of the core fluid and has properties associated with its diffusion into the core and the effect of centrifugal pressures in creating radial velocity components.

VIII REFERENCES

(1) Balint, E., "Techniques of Flow Visualization", Aircraft Engineering, June, 1953.

(2) Batchelor, G.K., "Note on a Class of Solutions of the Navier-Stokes Equation Representing Steady Rotational-Symmetric Flow", Quart. Journal of Appl. Mech. and Math., Vol. 4, 1951, pp. 29-41

(3) Cochran, E.G., "The Flow Due to a Rotating Disk", Proc. Cambr. Phil. Soc. Vol. 20, 1933-34, pp. 365-375.

(4) Cooke, J.C., "Three Dimensional Turbulent Boundary Layers", Royal Aircraft Establishment, Farnsboro, England, T.N. No. Acro 2762, June 1961.

(5) Cooke, J.C. and Hall, M.G., Advisory Group for Aeronautical Research and Development, N.A.T.O., Report 273, April 1960.

(6) Daily, J.W. and Arndt, R.E.A., "Enclosed Rotating Disks With Superposed Throughflow: A Survey of Basic Effects", MIT Hydrodynamics Laboratory Tech. Rep. No. 53, June 1962.

(7) Daily, J.W. and Nece, R.E., "Roughness and Chamber Dimension Effects on Induced Flow and Frictional Resistance of Enclosed Rotating Disks", MIT Hydrodynamics Laboratory Tech. Rep. No. 27, 1958.

(8) Daily, J.W. and Nece, R.E., "Chamber Dimension Effects on Induced Flow and Frictional Resistance of Enclosed Rotating Disks", Trans. ASME Jr. of Basic Engineering, Vol. 82, No. 1, March 1960.

(9) Geis, T., "Similar Three-Dimensional Boundary Layers", NASA Technical Translation F-30, 1961.

(10) Goldstein, S., "On the Resistance to the Rotation of a Disk Immersed in Fluid", Proc. Cambr. Phil. Soc. Vol. 31, Part II, April 1935, pp. 232-241.

(11) Gregory, N., Stuart, J.T., and Walker, W.S., "On the Stability of Three Dimensional Boundary Layers with Application to the Flow due to a Rotating Disk", Proc. Royal Society of London, A, Vol. 248, No. 943, pp. 155-199, 1955.

(12) Hall, I.M., "The Displacement Effect of a Sphere in a Two-Dimensional Shear Flow", Jr. of Fluid Mech., Vol. 1, Pt. 2, pp. 142-162, 1956.

(13) Jimbo, H., "Investigation of the Interaction of Windage and Leakage Phenomena in a Centrifugal Compressor", ASME Paper No. 56-A-47, 1956.

(14) Johnston, J.P., "Three Dimensional Turbulent Boundary Layers", MIT Gas Turbine Laboratory Report No. 39, May 1957.

(15) Karman, T. von, "Ueber laminare und turbulente Reibung", Zeitschrift fuer Angewandte Mathematik und Mechanik, Vol. 1, No. 4, 1921, pp. 244-249, NACA T.M. 1092 (1946).

(16) King, L.V., "On the Precision Measurement of Air Velocity by Means of the Linear Hot-Wire Anemometer", Philosophical Magazine, Series 6, Vol. 29, 1915, pp. 556-577.

(17) Lighthill, M.J., "Contributions to the Theory of the Pitot Tube Displacement Effect", Aeronautical Research Council, FM No. 2529 (19,182), 1957.

(18) MacMillan, F.A., "Experiments on Pitot Tubes in Shear Flow", Aeronautical Research Council Technical Report R and M 3028, 1957.

(19) Mager, A., "Generalization of Boundary-Layer Momentum-Integral Equations to Three-Dimensional Flows Including Those of Rotating Systems", NACA Technical Note 2310, March 1951.

(20) Maroti, L.A., Deak, G., and Kreith, F., "Flow Phenomena of Partially Enclosed Disks", Trans. A.S.M.E., Jr. of Basic Engineering, Series D Vol. 82, No. 3, Sept. 1960.

(21) Mock, W.C., Jr., and Dryden, H.L., "Improved Apparatus for the Measurement of Fluctuations of Air Speed in Turbulent Flow", NACA Technical Report 448, 1932.

(22) Olsson, E.K.A., "Centrifugal Effect on the Boundary Layer of an Axial Turbo-Machine", Sc.D. thesis in Mechanical Engineering, 1962.

(23) Picha, K.G. and Eckert, E.R.G., "Study of the Air Flow between Coaxial Disks Rotating with Arbitrary Velocities in an Open or Enclosed Space", Proc. 3rd U.S. Nat. Congr. Appl. Mech., 1959, p. 791

(24) Pohlhausen, K. and Breiter, M.C., "Laminar Flow Between Two Parallel Rotating Disks", Aeronautical Research Laboratory, 62-318, 1962.

(25) Reiner, M. "A Centrifugal Pump Effect in Air", Proc. 9th Intl. Congr. of Applied Mech., Vol. 2, 1957, pp. 429-438.
also, Proc. Royal Society, Series A, Vol. 240, 1957, p.173

(25a) Reiner, M., "Research on Cross Stresses in the Flow of Rarefield Air", Report of the Techn. Research and Dev. Foundation, Ltd., Haifa, Israel, (U.S. Air Force Contr. AF 61(052)-223, Monitoring Agency, Doc. No. AFOSR 44), March 1961.

(26) Schlichting, H., "Boundary Layer Theory", 4th Edition, *McGraw-Hill*, New York, 1960.

(27) Schultz-Grunow, F., "Der Reibungswiderstand rotierender Scheiben in Gehäusen", *Zeitschrift fuer Angewandte Mathematik und Mechanik*, Vol. 15, pp. 191-204, 1935.

(28) Senoo, I., "Three Dimensional Laminar Boundary Layer in Curved Channels with Acceleration", *MIT Gas Turbine Laboratory Report No. 37*, Nov. 1956.

(29) Smith, N.H., "Exploratory Investigation of Laminar Boundary Layer Oscillations on a Rotating Disk", *NACA* Technical Note 1227, May 1947.

(30) Soo, S.L., "Laminar Flow Over an Enclosed Rotating Disk", Trans. *ASME*, Vol. 80, No. 2, 1958, pp. 287-296.

(31) Stewartson, K., "On the Flow Between Two Rotating Coaxial Disks", *Quart. Journal of Appl. Mech. and Math.*, Vol. 7, Pt. 4, 1954.

(32) Taylor, E.S., "The Skewed Boundary Layer", *Trans. ASME, Jr. of Basic Engineering*, Series D, No. 3, Vol. 81, Sept. 1959, pp. 297-304.

(33) Taylor, G.I., "Stability of a Viscous Fluid Contained Between Two Rotating Cylinders", *Phil. Trans. of the Royal Society of London*, Series A, Vol. 223, pp. 289-343, 1923.

(34) Taylor, G.I. and Saffman, P.G., "Effects of Compressibility at Low Reynolds Numbers", *Jr. Areo. Sci*, Vol. 24, 1957, pp. 553-562.

(35) Theodorsen, T. and Regier, A.A. "Experiments on Drag of Revolving Disks, Cylinders, and Streamline Rods at High Speeds", *NACA*, Technical Report 793, 1944.

(36) Thom. A., "The Flow at the Mouth of a Stanton Pitot", *Aero. Research Council* Technical Report R and M 2984, 1956.

(37) Welsh, W.E., Jr. and Hartnett, "Velocity Measurements in the Boundary Layer and in the Main Flow Between two Coaxial Disks Rotating with Equal Velocities in Air", *Proc. 3rd U.S. Nat. Congr. Appl. Mech.*, 1959, p. 847.

(38) Young, A.D. and Maas, J.N., "The Behavior of a Pitot Tube in a Transverse Total Pressure Gradient", *Aero. Research Committee* Technical Report R and M 1770, 1937.

(39) "Symposium on Flow Visualization", *Presentation Summaries*, A.S.M.E. Annual Meeting, Nov. 30, 1960.

(40) "Symposium on Measurement in Unsteady Flow", A collection of articles, ASME Hydraulic Division Conference, Worcester, Mass., May, 1962.

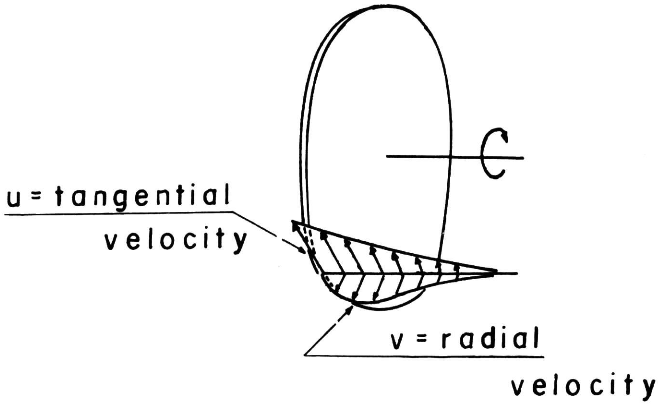

Fig. 2 Skewed Boundary Layer
on a Rotating Disk

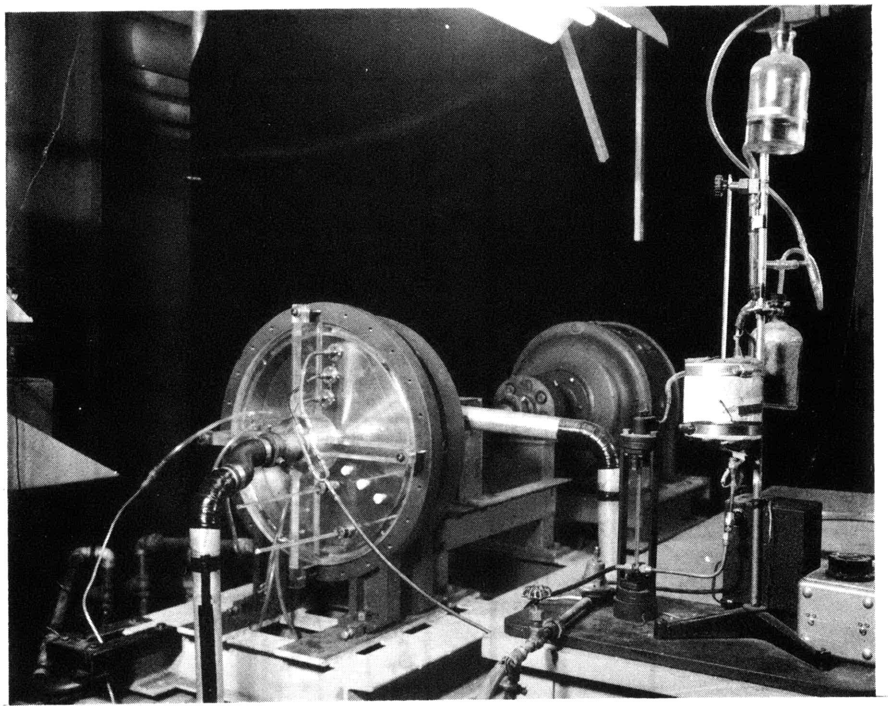

Fig. 3 General View of Test Setup with Piping
for Circulating Air and Arranged for
Smoke Flow-Visualization Studies

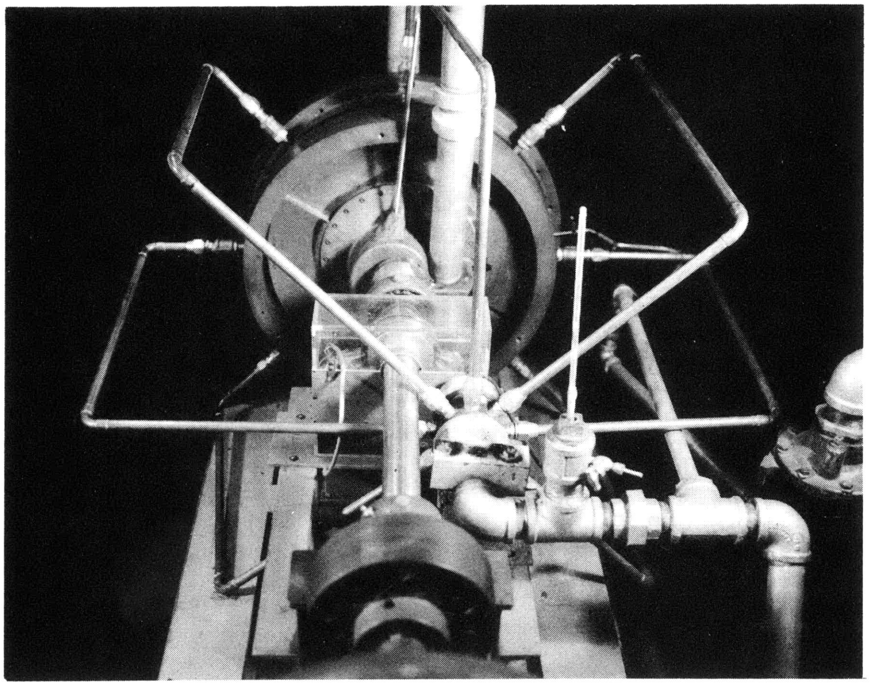

Fig. 4 General View of Test Setup showing Disk Housing from Rear with Piping for Circulating Liquid.

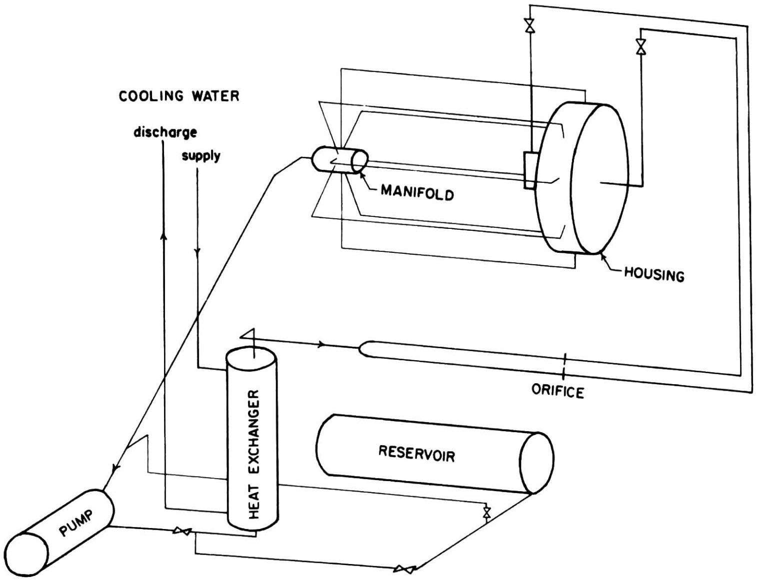

Fig. 5 Schematic of External Circuit for Liquid Throughflow

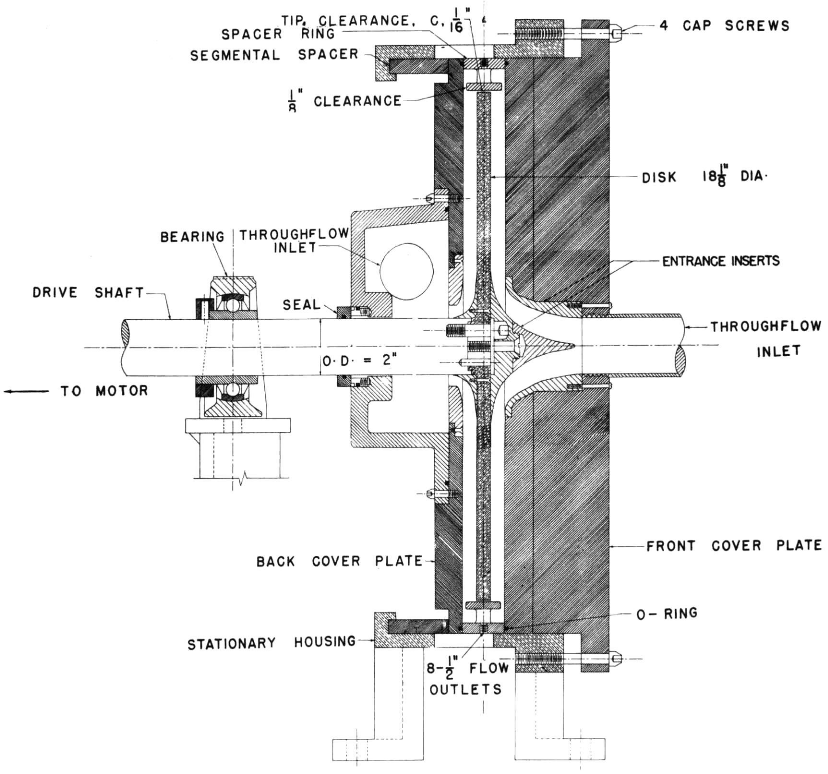

Fig. 6 Section of Test Chamber as Arranged for Circulating Throughflow (Geometry A)

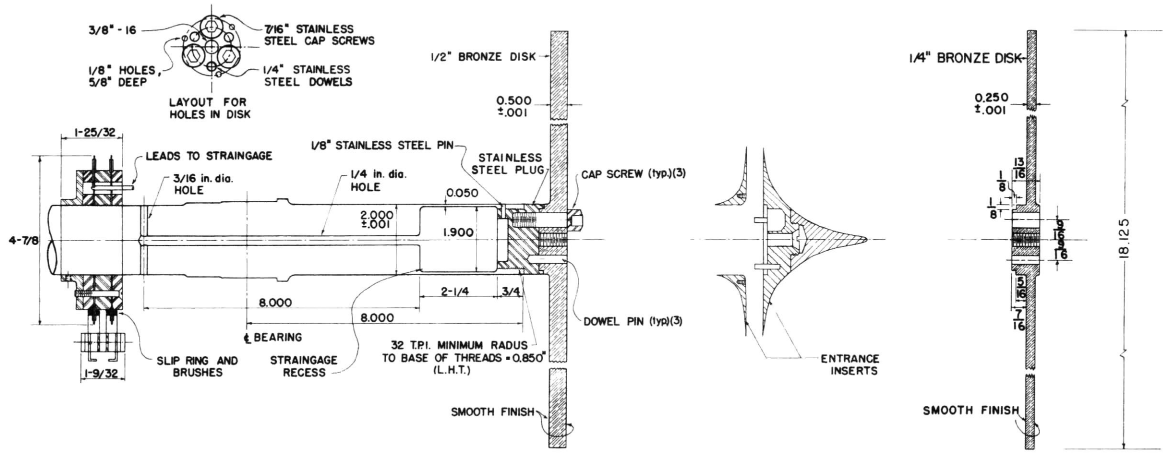

Fig. 7 Disk and Shaft Assembly

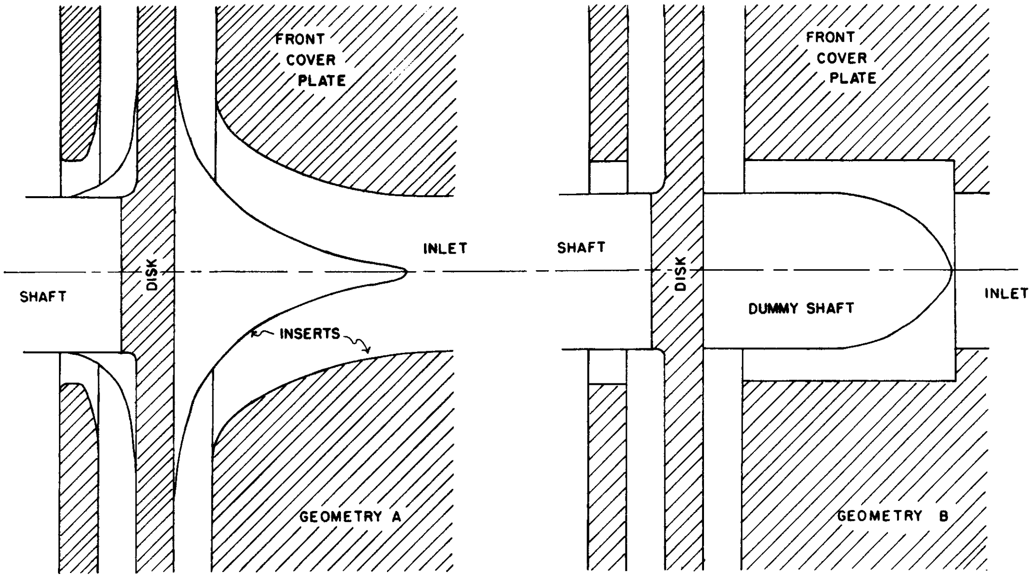

Fig. 8 Inlet Geometries A and B

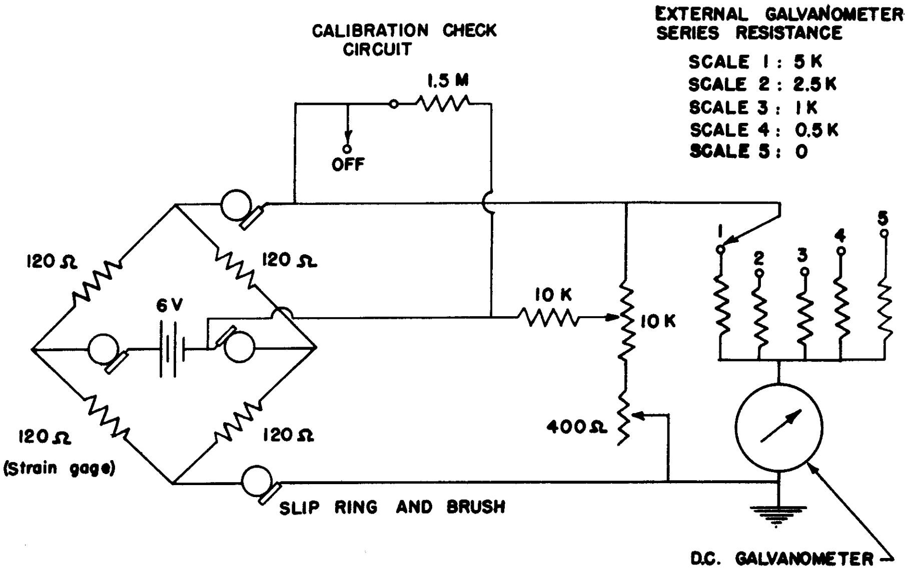

Fig. 9 Schematic of Torque Measuring Circuit

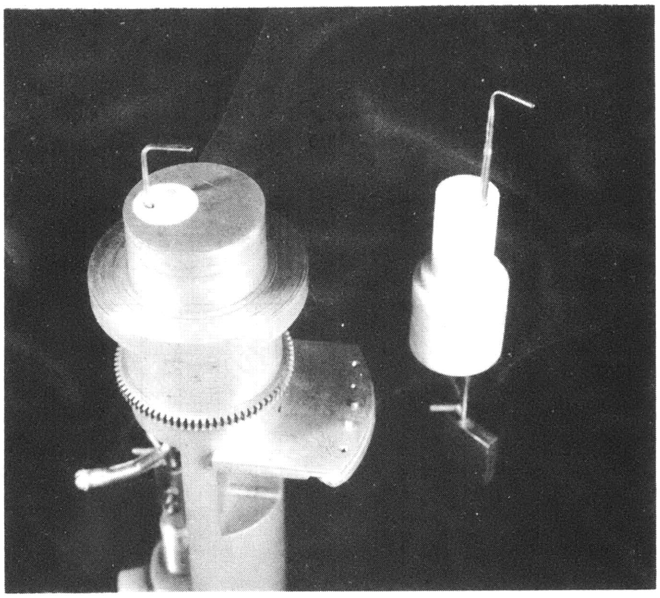

Fig. 10 Velocity Probes and Traverse Control Unit

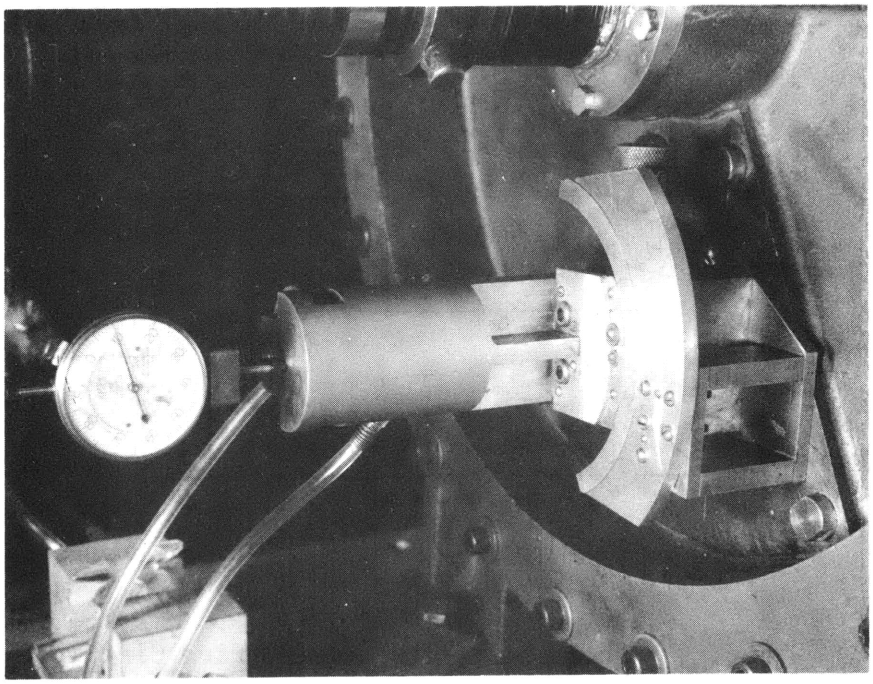

Fig. 11 Traverse Control Unit Mounted for Measurements

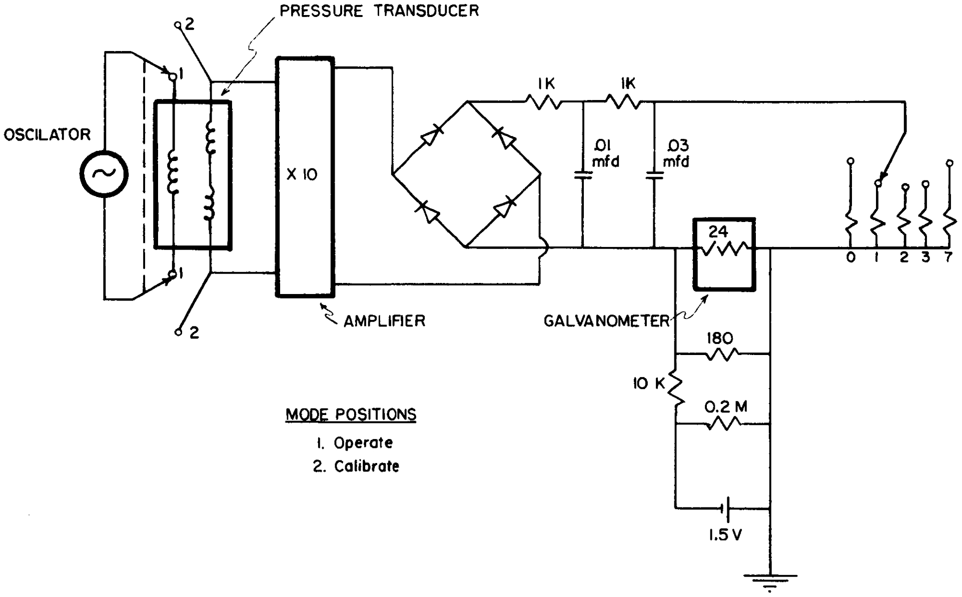

Fig. 12 Schematic of Velocity Measuring Circuit

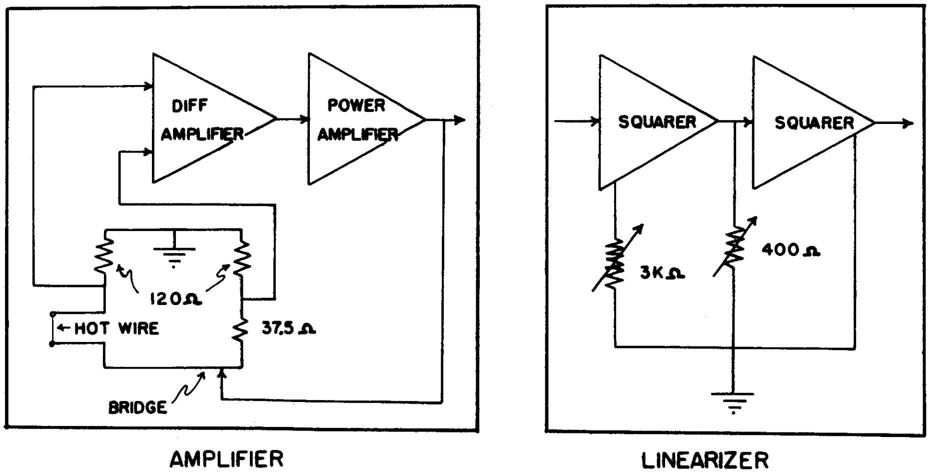

Fig. 13 Schematic of Hot Wire Circuit

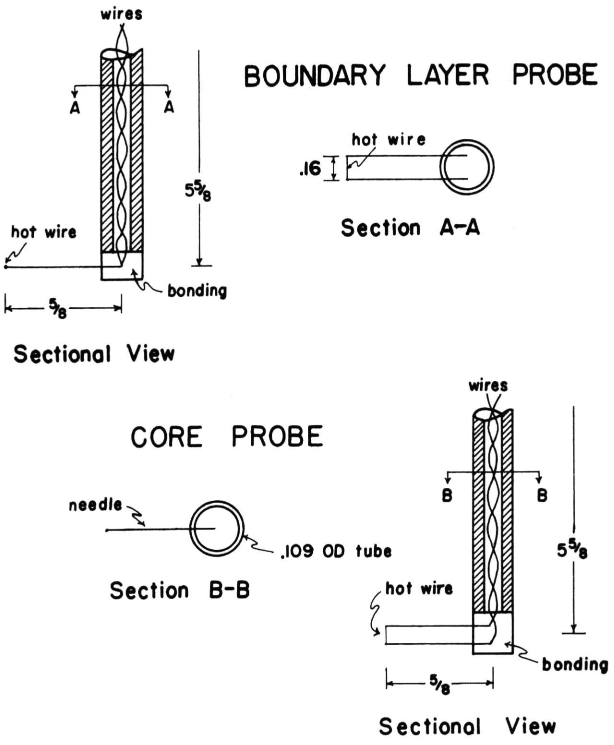

Fig. 14 Detail of Hot Wire Probe

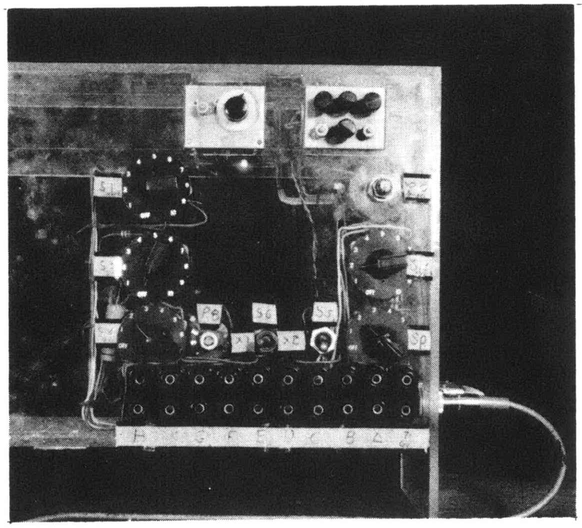

P2

P6 P4 P2

P5 P3 P1

Amplifier
Section
on Left

Linearizer
Section on
Right

PO

Hot Wire Switch

Power Switch

Fig. 15a Hot Wire Amplifier and Linearizer Controls

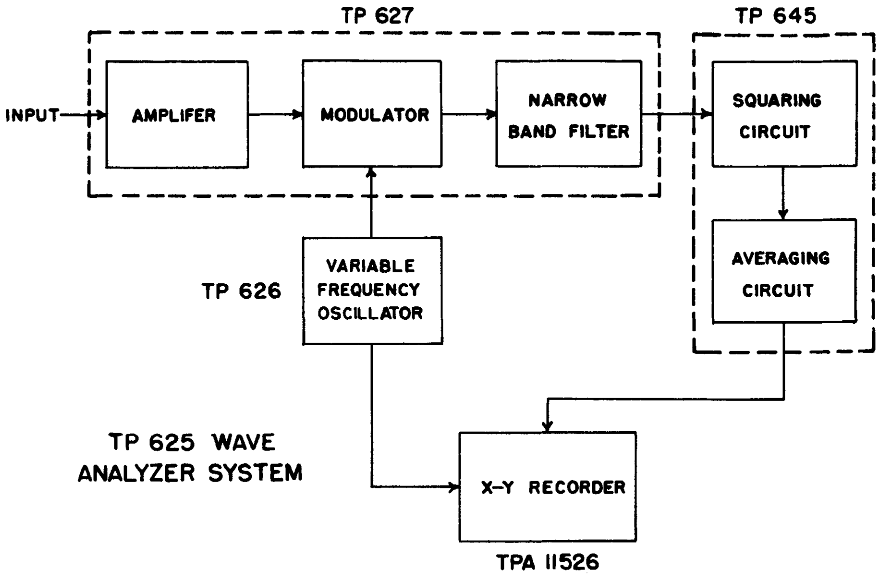

Fig. 15b Block Diagram of TP625 Wave Analyzer System

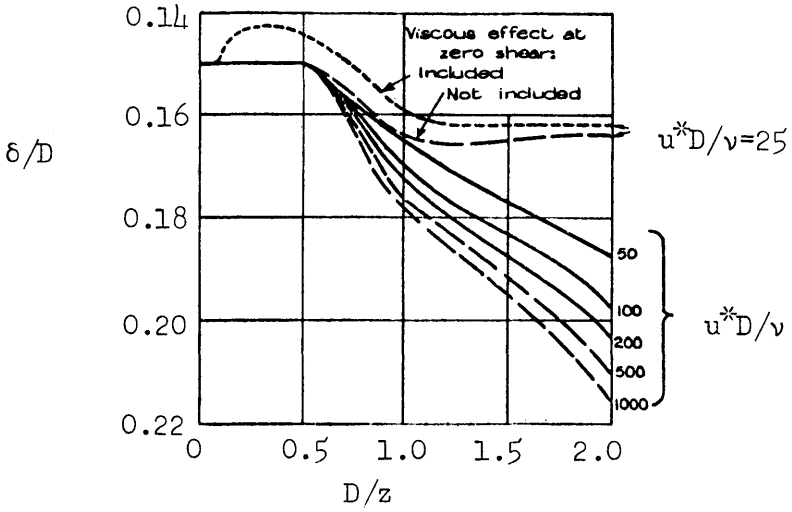

Fig. 16 Mac Millan's Effective Center Displacement Correction using Eq.(49)

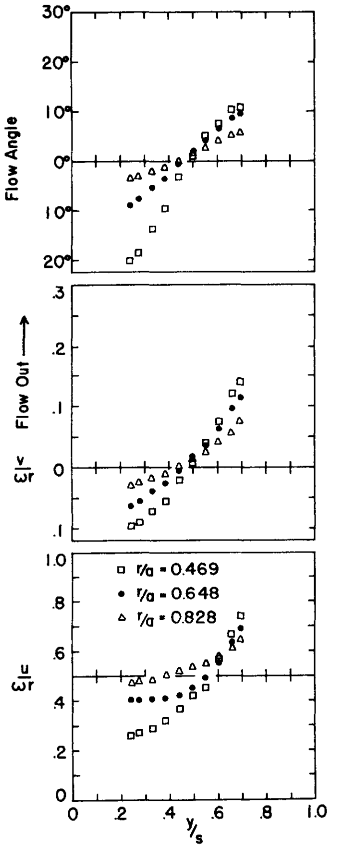

Fig. 17 Velocity Data
s/a = 0.0138
$\mathbb{R} = 2.95 \times 10^5$
Q = 0

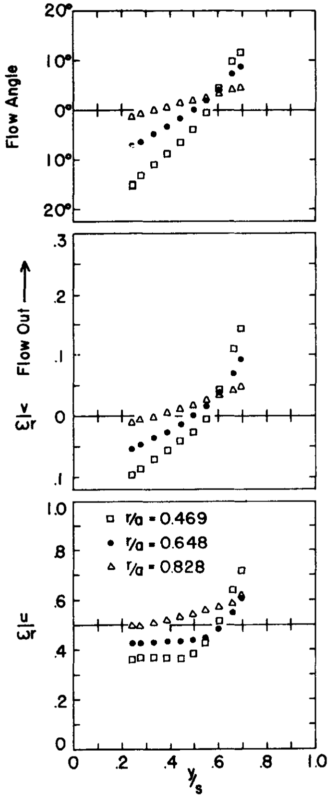

Fig. 18 Velocity Data
s/a = 0.0138
$\mathbb{R} = 6.9 \times 10^5$
Q = 0

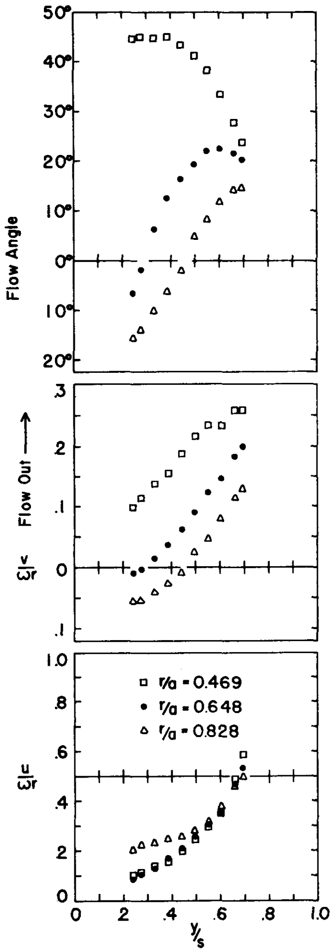

Fig. 19 Velocity Data
s/a = 0.0138
$\mathbb{R} = 2.95 \times 10^5$
Q = 3 cfm

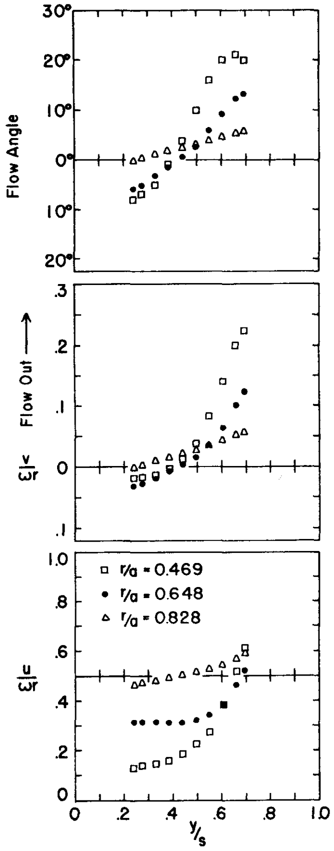

Fig. 20 Velocity Data
s/a = 0.0138
$\mathbb{R} = 6.9 \times 10^5$
Q = 3 cfm

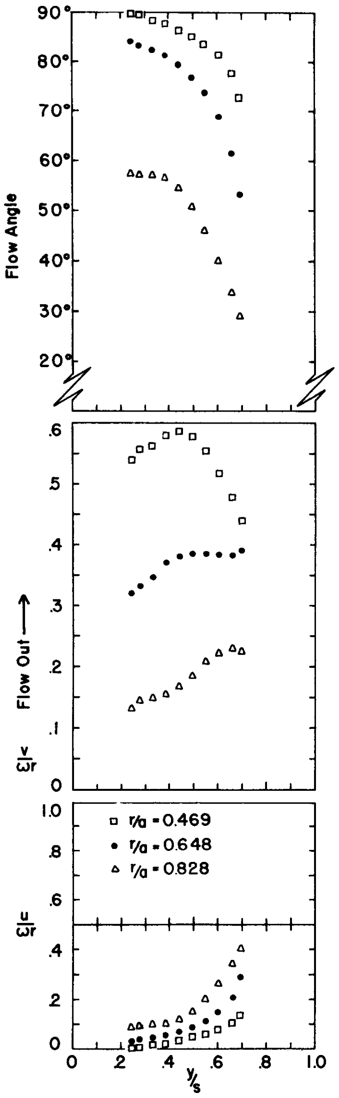

Fig. 21 Velocity Data
s/a = 0.0138
$\mathbb{R} = 2.95 \times 10^5$
Q = 12.9 cfm

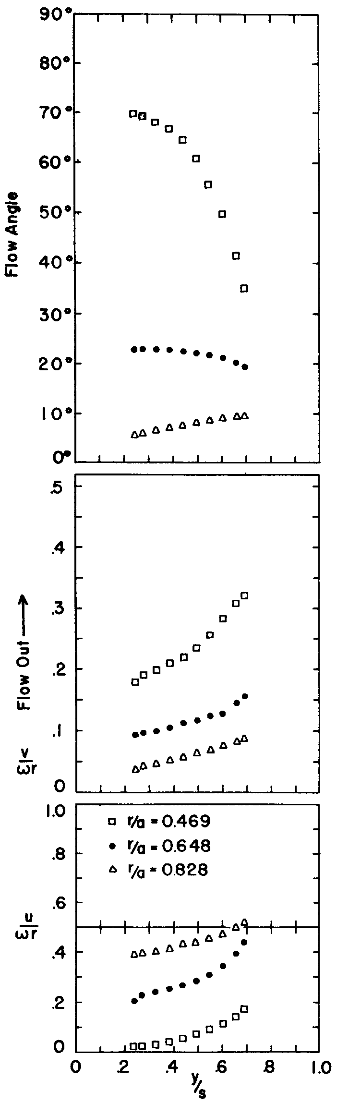

Fig. 22 Velocity Data
s/a = 0.0138
$\mathbb{R} = 6.9 \times 10^5$
Q = 12.9 cfm

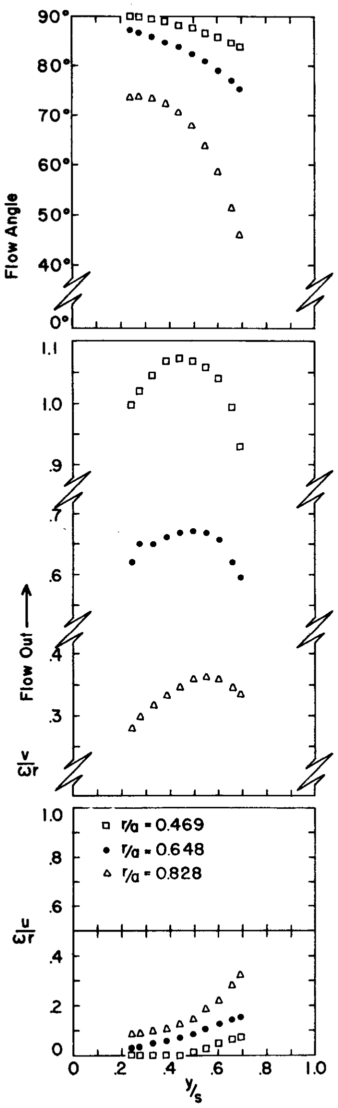

Fig. 23 Velocity Data
s/a = 0.0138
$\mathbb{R} = 2.95 \times 10^5$
Q = 26 cfm

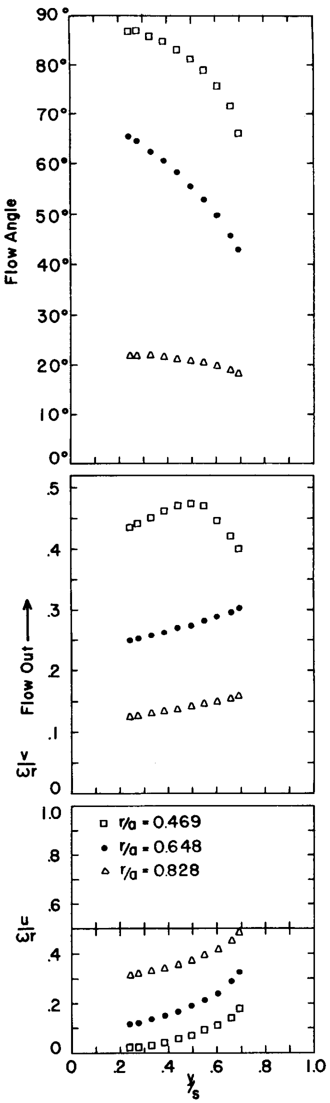

Fig. 24 Velocity Data
s/a = 0.0138
$\mathbb{R} = 6.9 \times 10^5$
Q = 26 cfm

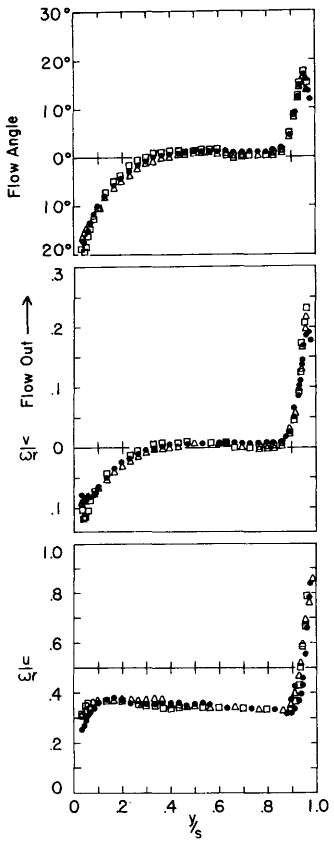

Fig. 25 Velocity Data
s/a = 0.0690
ℝ = 2.95 x 10^5
Q = 0

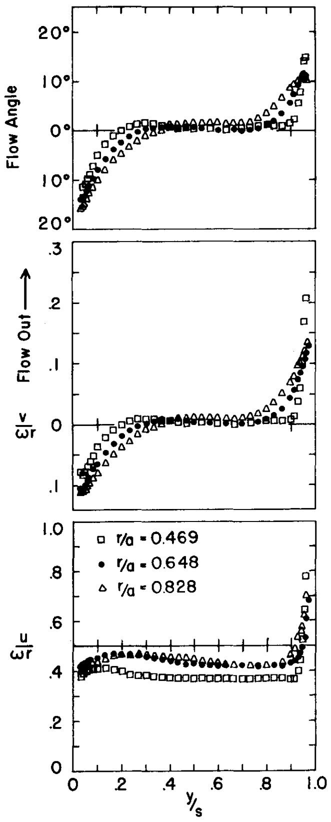

Fig. 26 Velocity Data
s/a = 0.0690
ℝ = 6.9 x 10^5
Q = 0

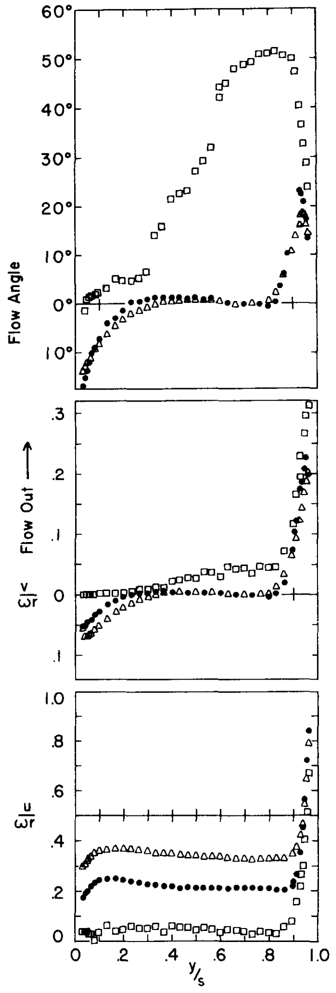

Fig. 27 Velocity Data
s/a = 0.0690
ℝ = 2.95 x 10^5
Q = 3.35 cfm

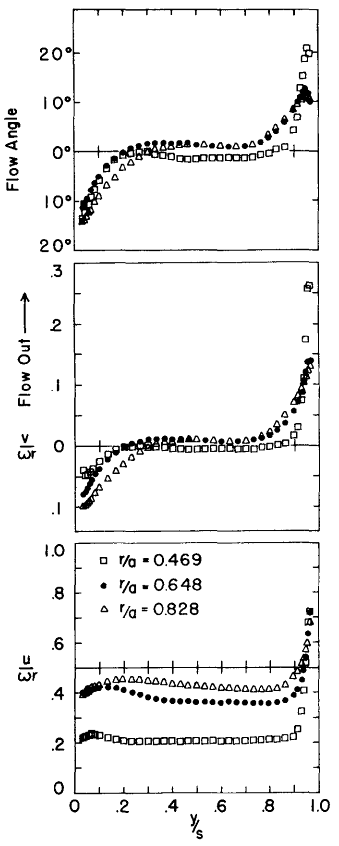

Fig. 28 Velocity Data
s/a = 0.0690
ℝ = 6.9 x 10^5
Q = 3.35 cfm

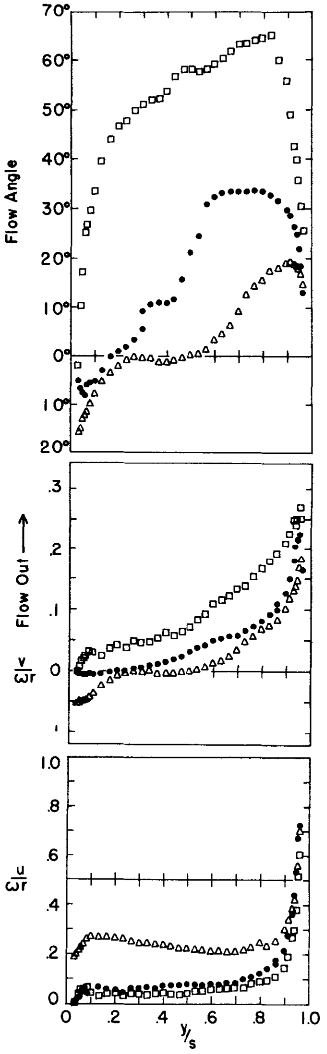

Fig. 29 Velocity Data
s/a = 0.0690
$\mathbb{R}$ = 2.95 x 10^5
Q = 12.9 cfm

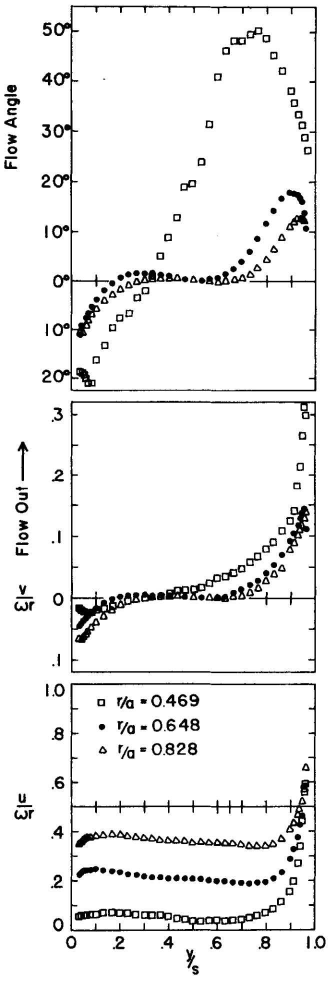

Fig. 30 Velocity Data
s/a = 0.0690
$\mathbb{R}$ = 6.9 x 10^5
Q = 12.9 cfm

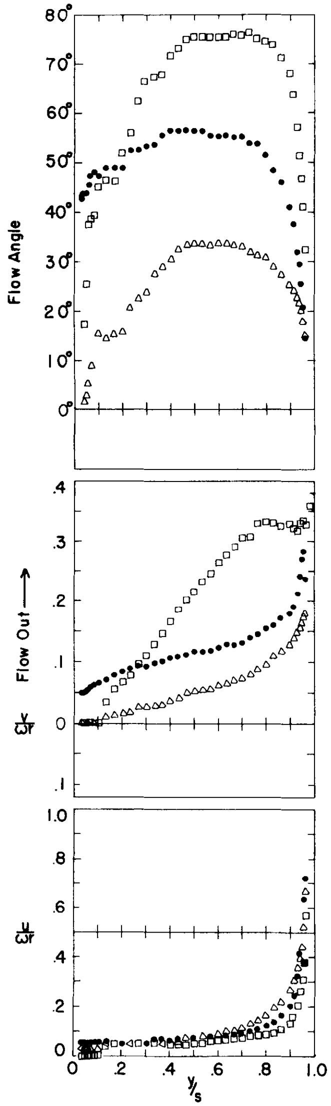

Fig. 31 Velocity Data
s/a = 0.0690
$\mathbb{R}$ = 2.95 x 10^5
Q = 26 cfm

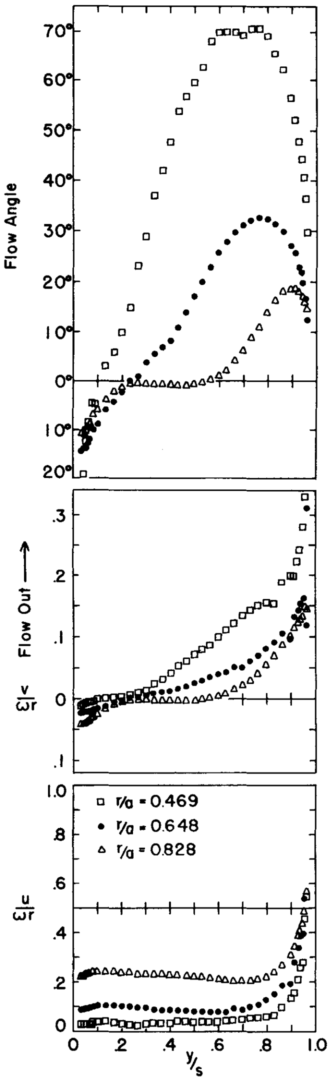

Fig. 32 Velocity Data
s/a = 0.0690
$\mathbb{R}$ = 6.9 x 10^5
Q = 26 cfm

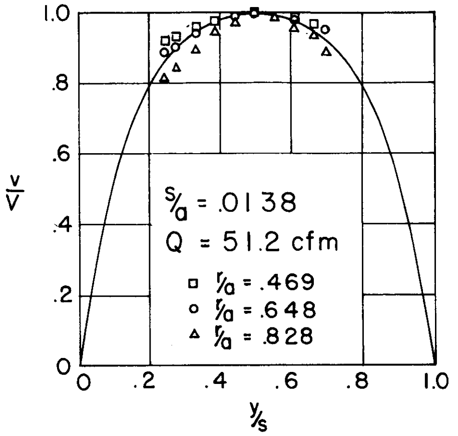

Fig. 33 Velocity Data
Zero Disk Speed
s/a = 0.0134

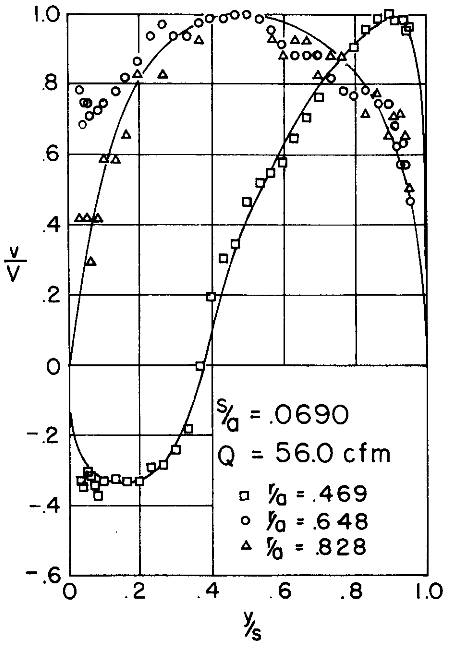

Fig. 34 Velocity Data
Zero Disk Speed
s/a = 0.069

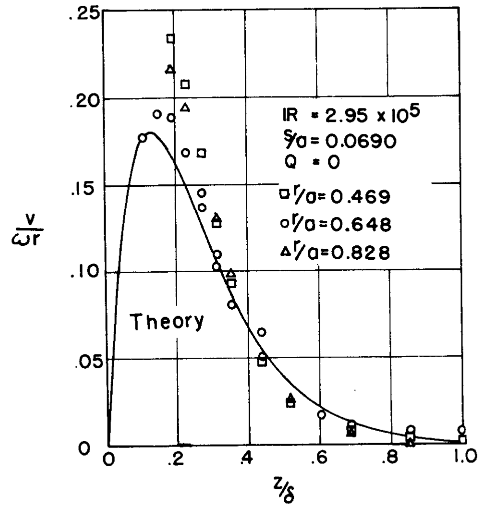

Fig. 35 Radial Profile
on Disk
Q = 0
s/a = 0.069

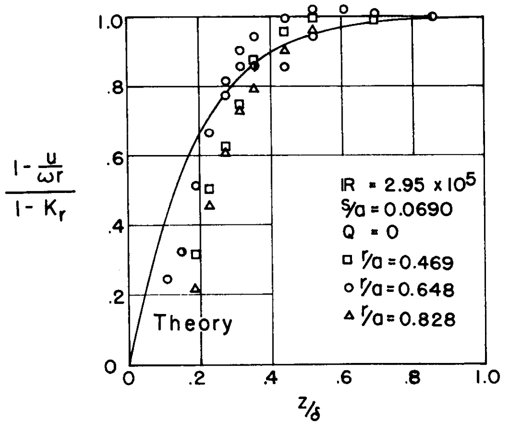

Fig. 36 Tangential
Profile on Disk
Q = 0
s/a = 0.069

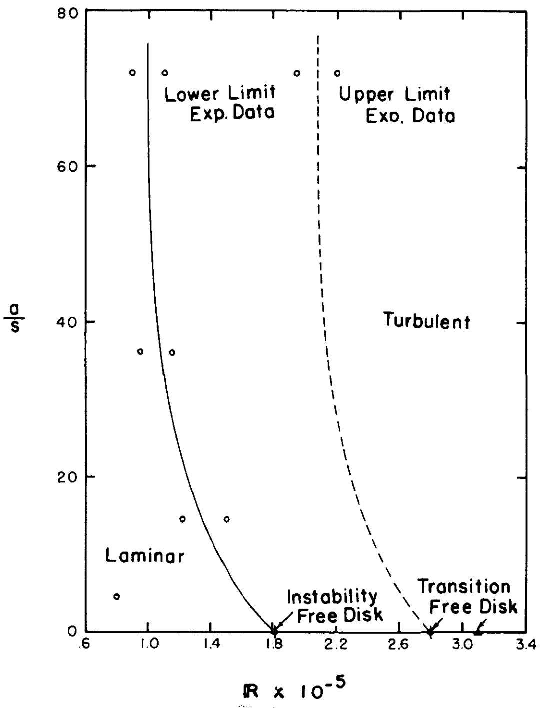

Fig. 37 Instability vs. Transition on a Rotating Disk

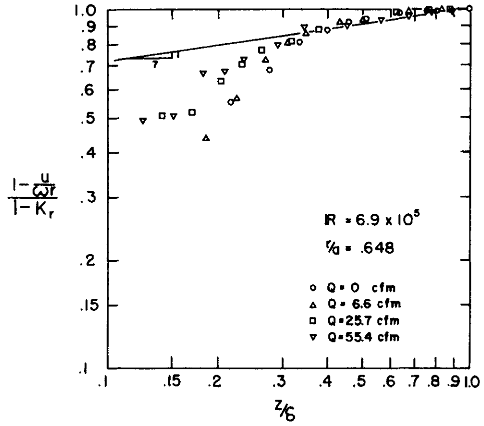

Fig. 38 Turbulent Tangential Velocity Profiles on Disk s/a = 0.069 r/a = 0.648

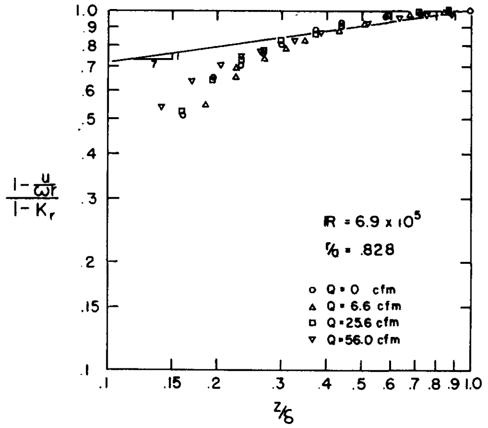

Fig. 39 Turbulent Tangential Velocity Profiles on Disk s/a = 0.069 r/a = 0.828

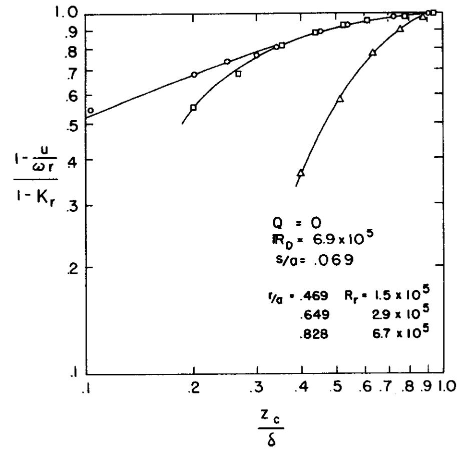

Fig. 40 Turbulent Tangential Velocity Profiles on Disk as Corrected for Probe Effective Center Displacement

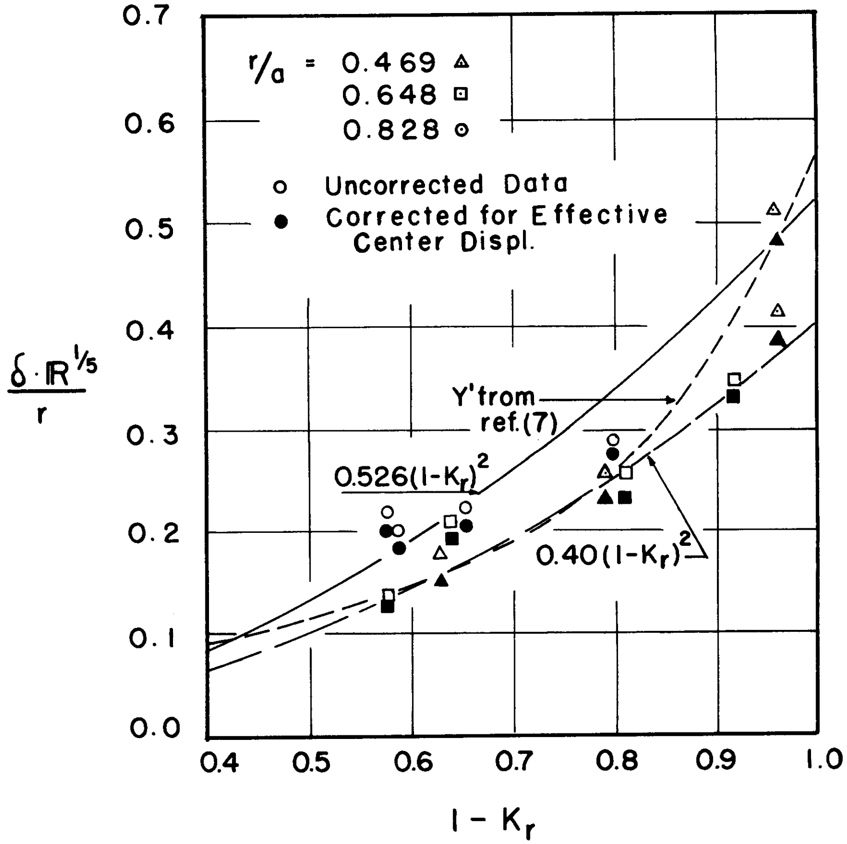

Fig. 41 Boundary Layer Growth as a Function of Core Rotation

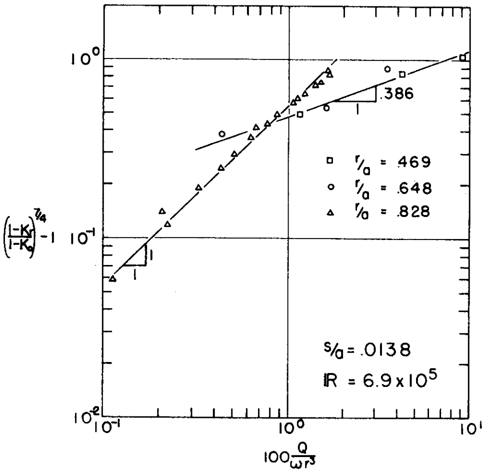

Fig. 42 Core Rotation
s/a = 0.0138 $\mathbb{R} = 6.9 \times 10^5$

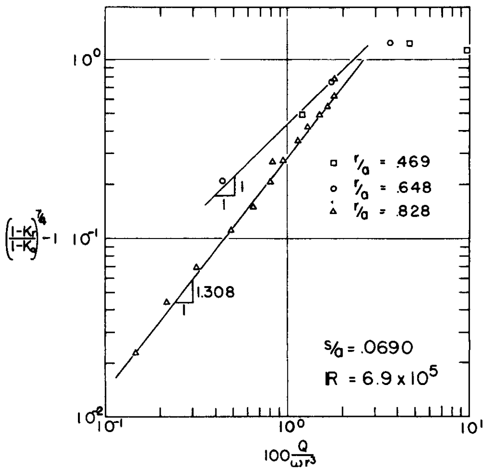

Fig. 43 Core Rotation
s/a = 0.069 $\mathbb{R} = 6.9 \times 10^5$

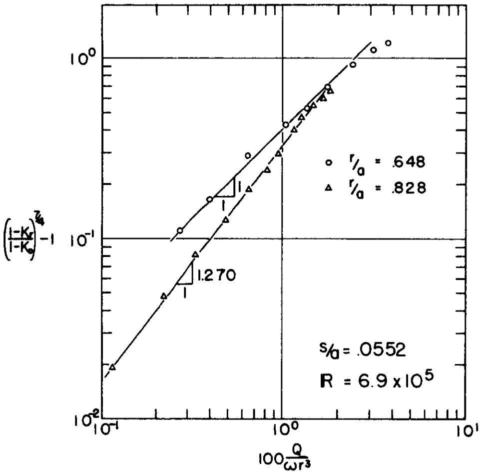

Fig. 44 Core Rotation
s/a = 0.0552 $\mathbb{R} = 6.9 \times 10^5$

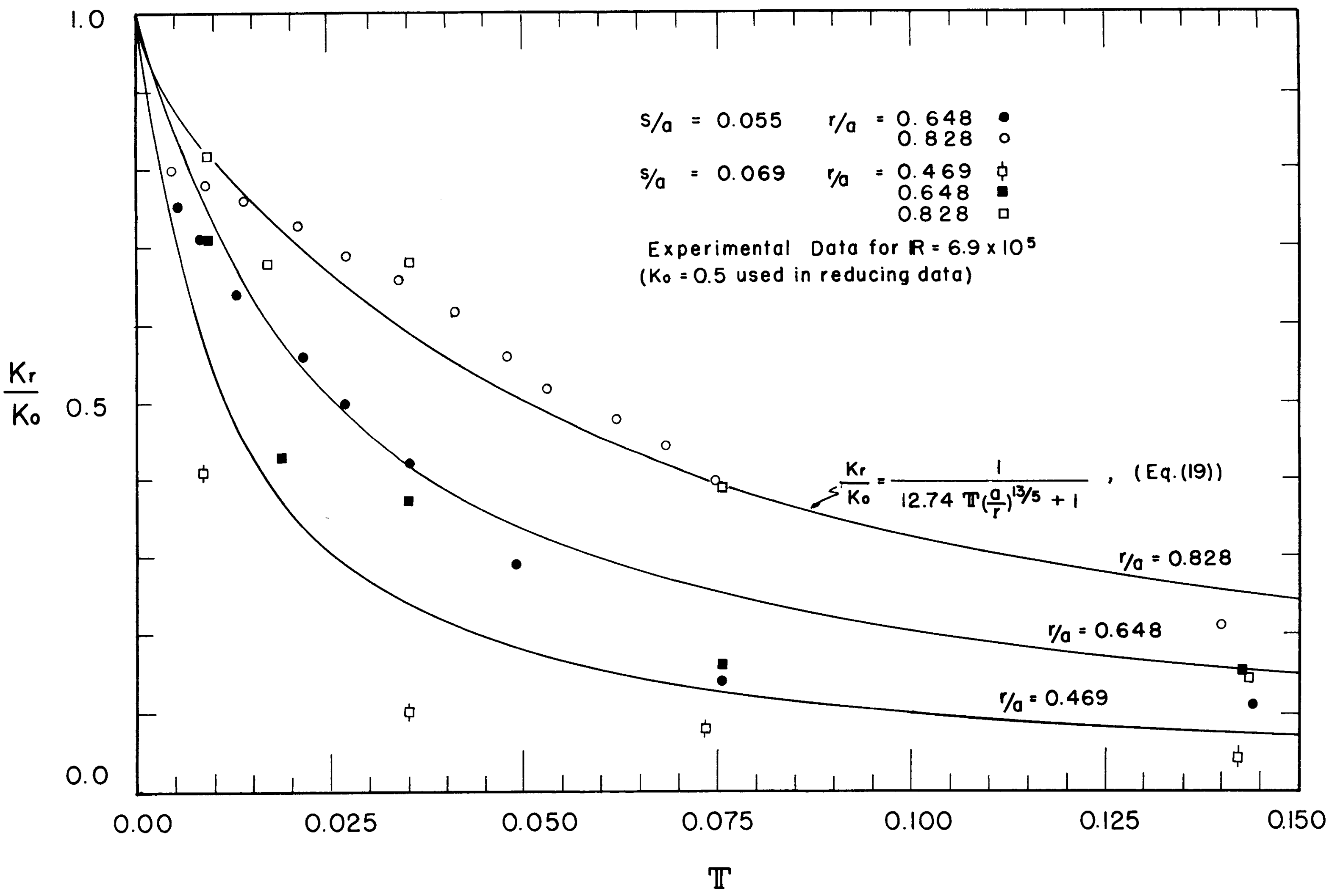

Fig. 45 Computed and Measured Core Rotation

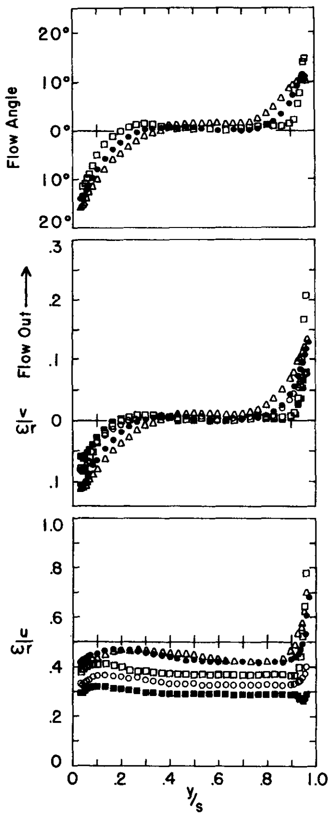

Fig. 46 Q=0

Geometry A

■ r/a=0.469

○ 0.648

▲ 0.828

Geometry B

□ r/a=0.469

● 0.648

△ 0.828

Velocity Profile Comparison

Geometries A and B
(See Fig. 8)

s/a = 0.069 $\mathbb{R} = 6.9 \times 10^5$

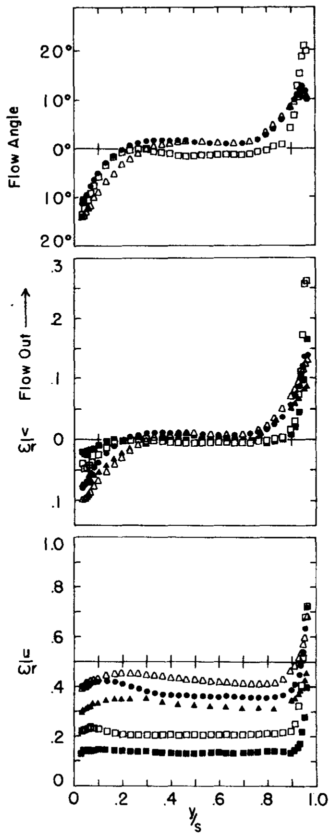

Fig. 47 Q = 3.35 cfm

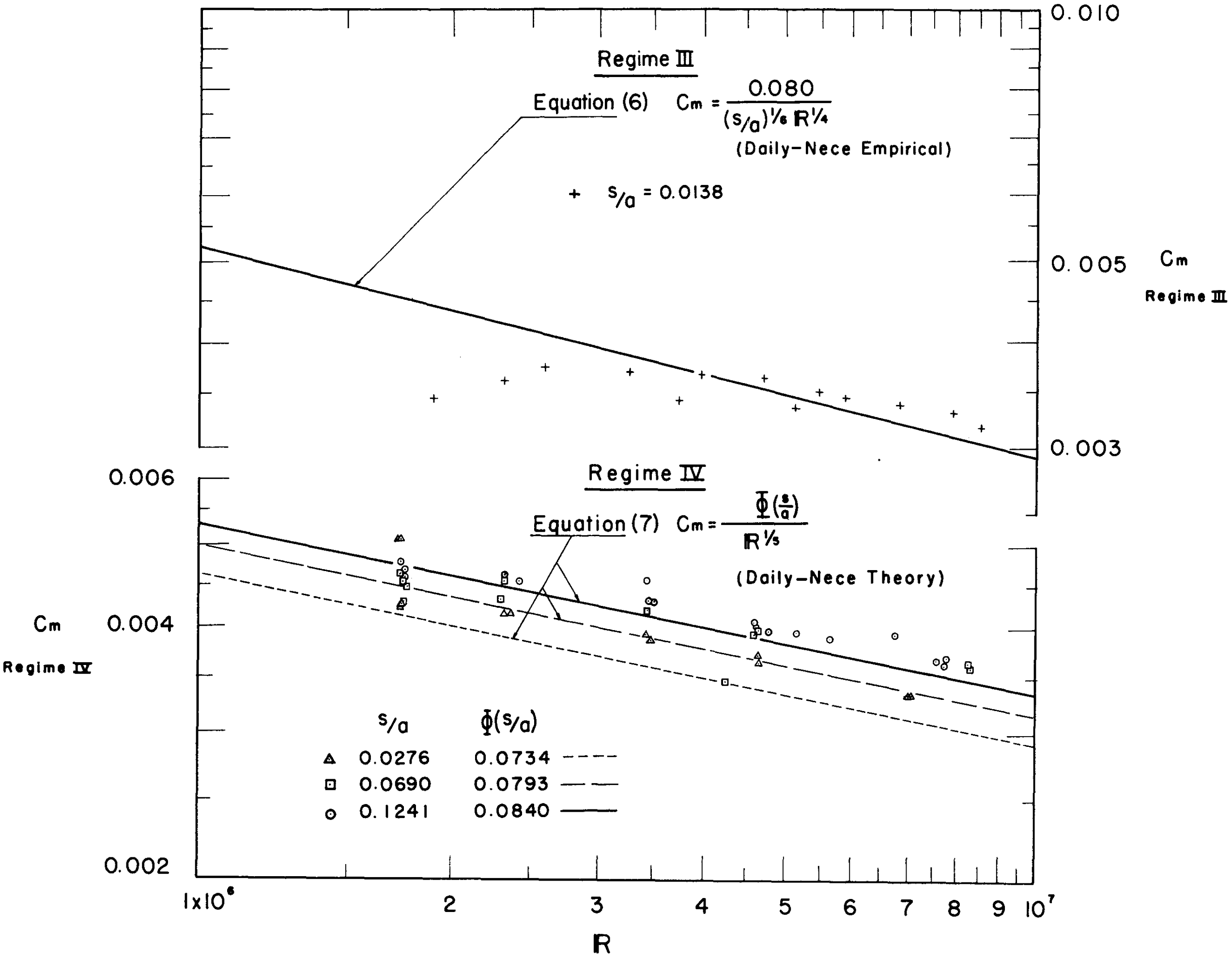

Fig. 48 Torque Coefficients for Zero Throughflow

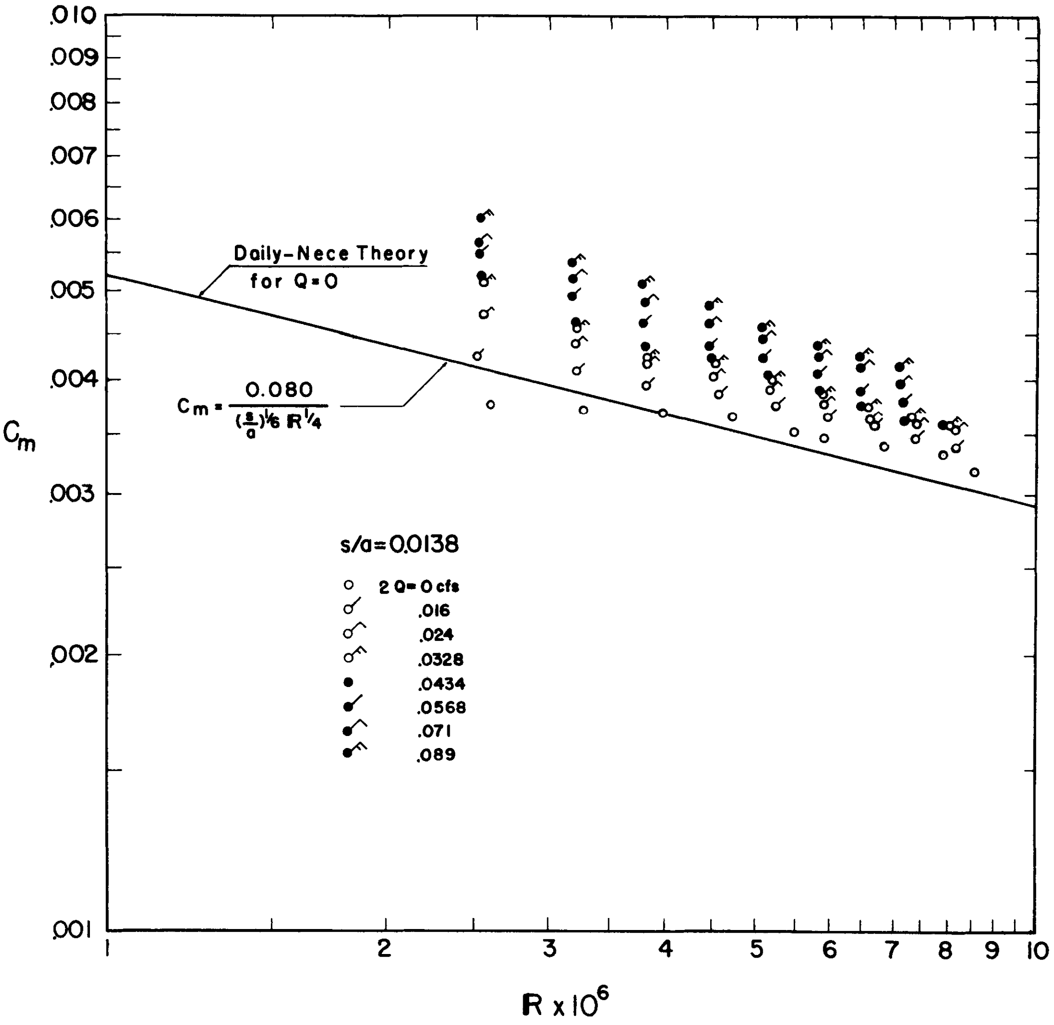

Fig. 49 Torque Coefficients for Variable Throughflow: s/a = 0.0138

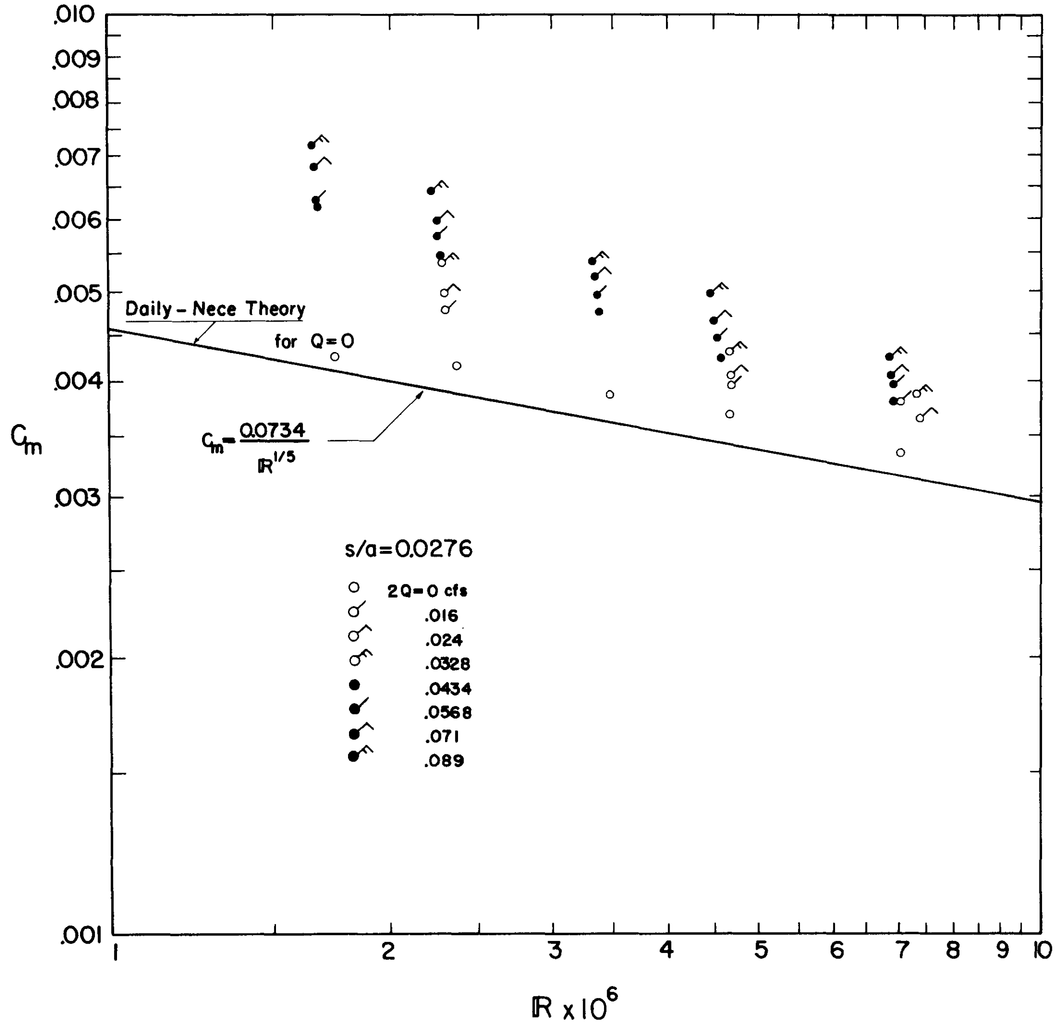

Fig. 50 Torque Coefficients for Variable Throughflow: s/a = 0.0276

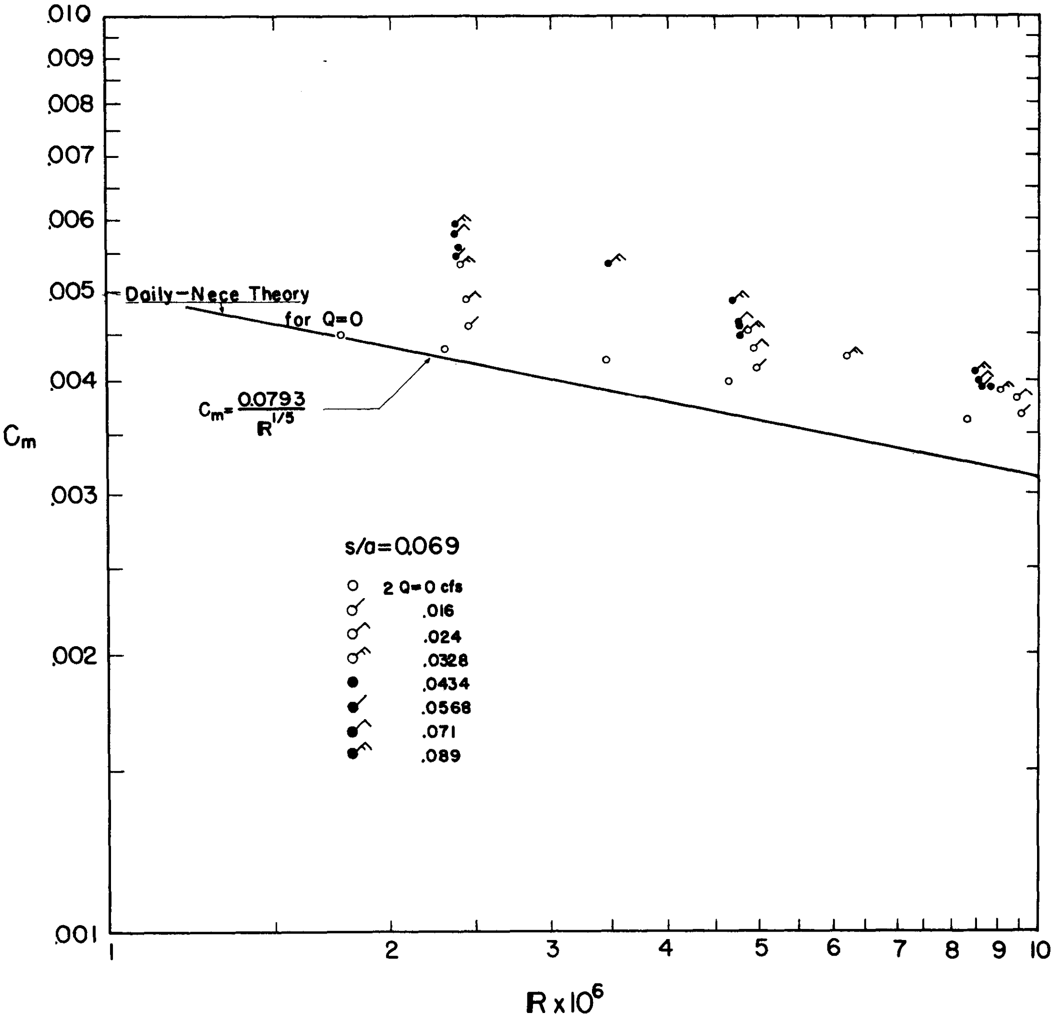

Fig. 51 Torque Coefficients for Variable Throughflow: s/a = 0.069

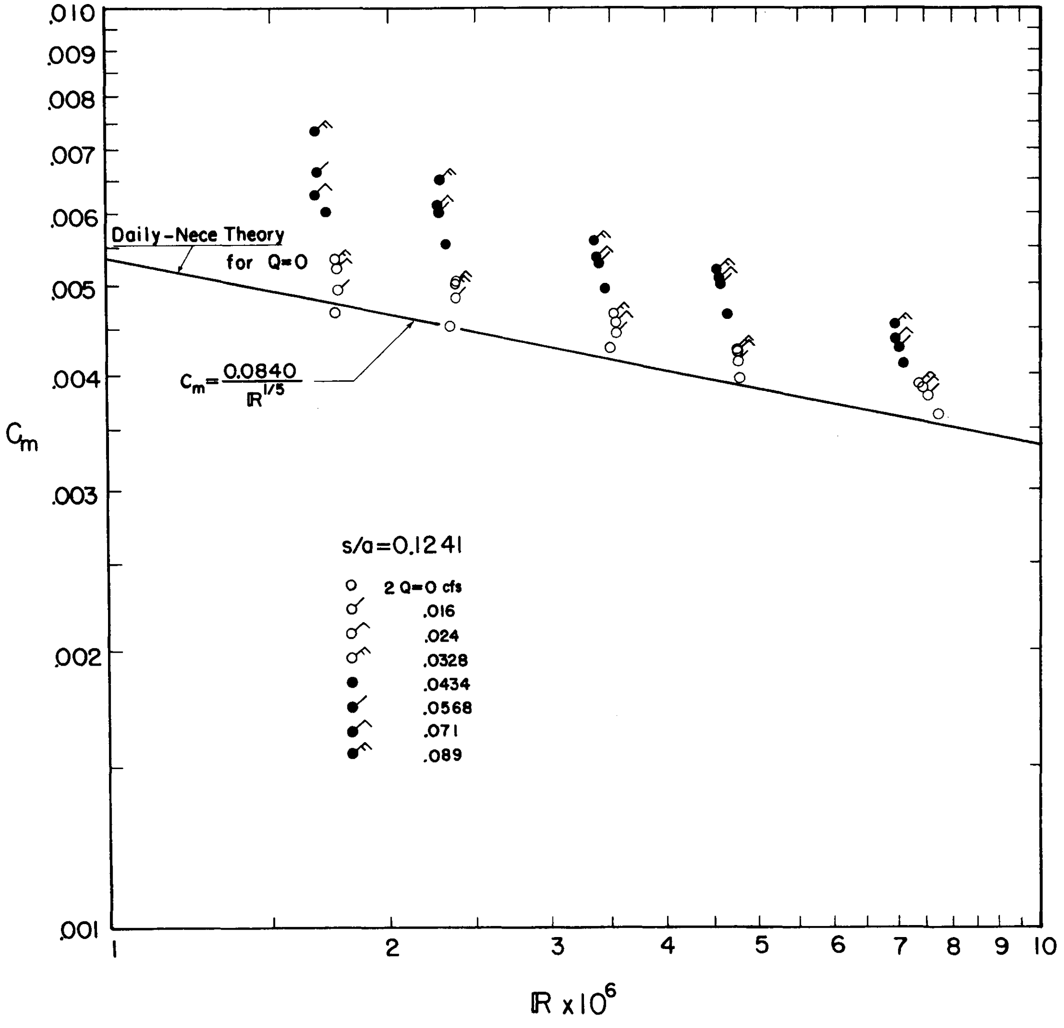

Fig. 52 Torque Coefficients for Variable Throughflow:
s/a = 0.1241

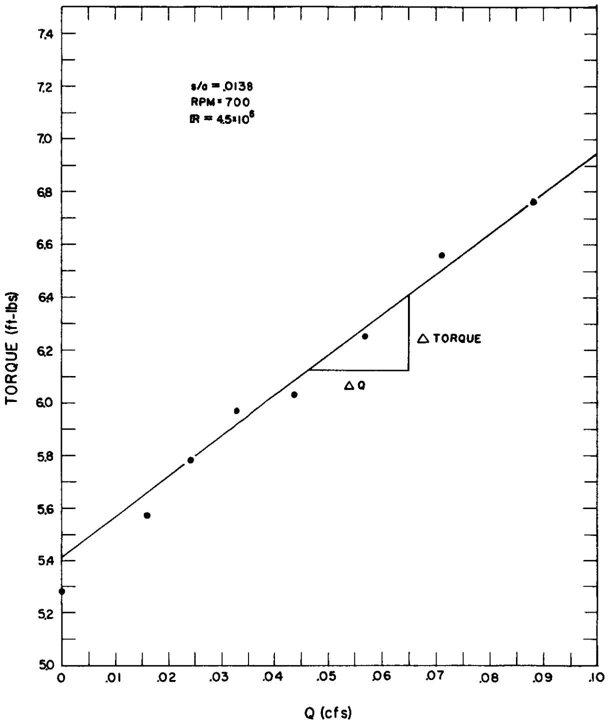

Fig. 53 Measure Torque vs. Q (typical)

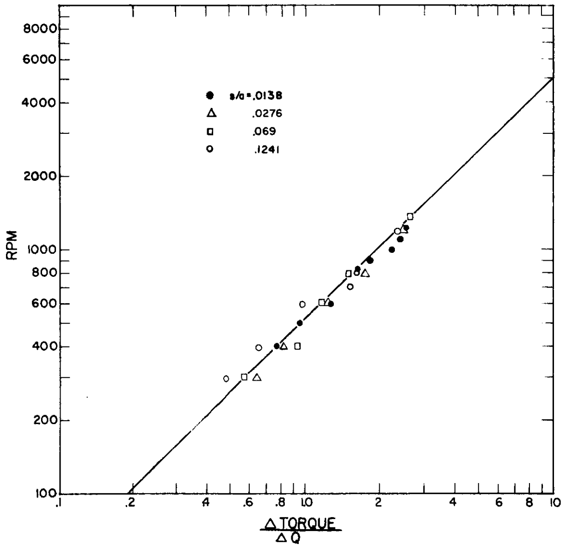

Fig. 54 ΔM/ΔQ vs. Disk Speed

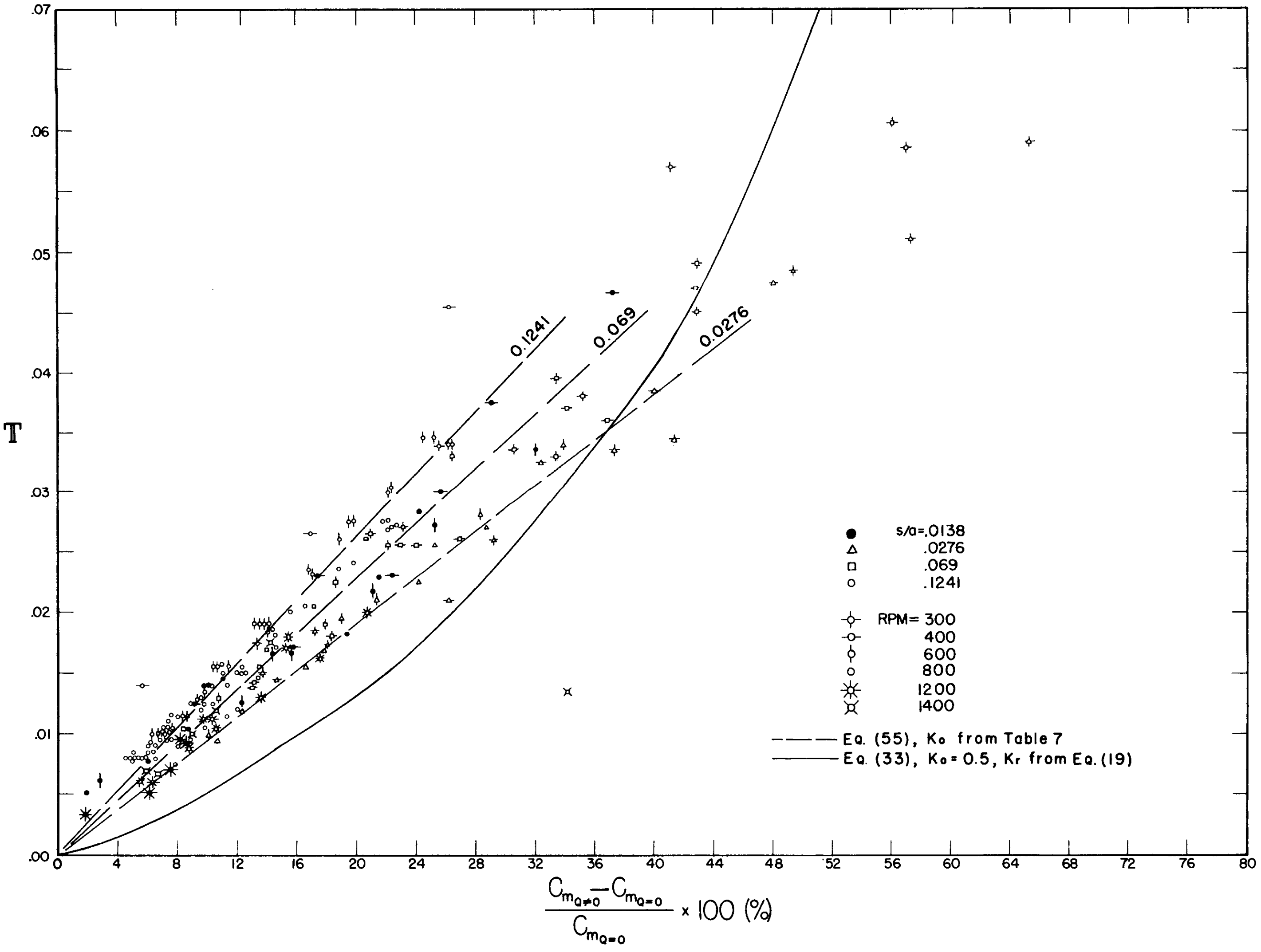

Fig. 55 Percentage Torque Increase as a Function of Throughflow Number

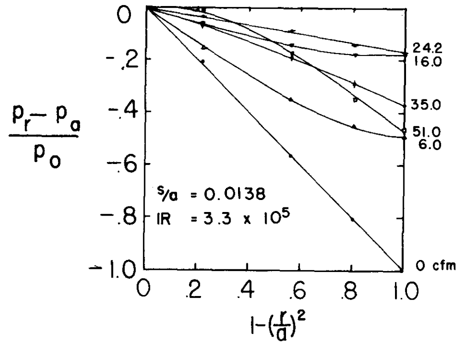

Fig. 56

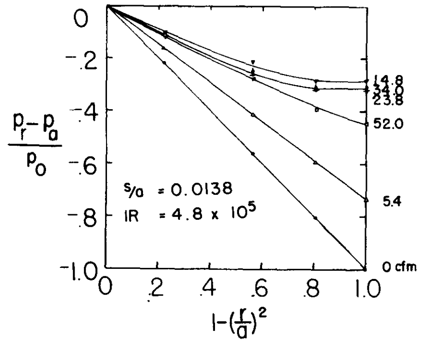

Fig. 57

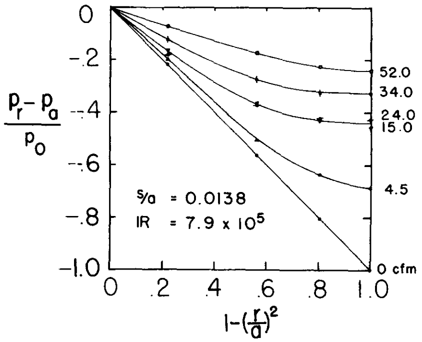

Fig. 58

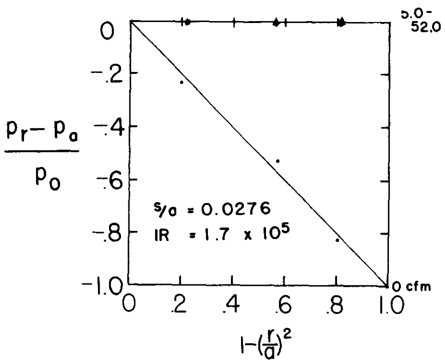

Fig. 59

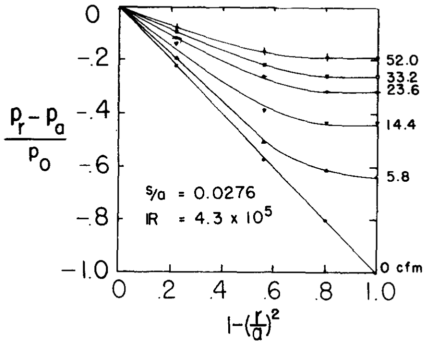

Fig. 60

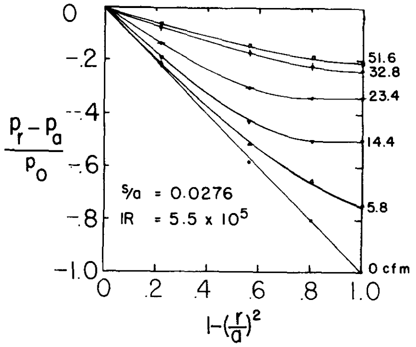

Fig. 61

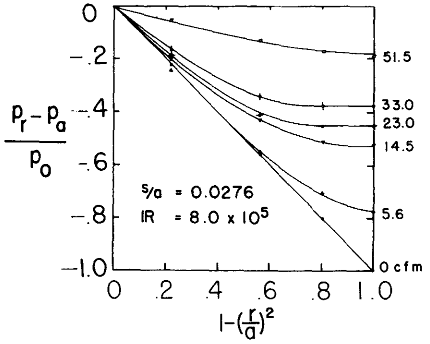

Fig. 62

Figs. 56-62 Dimensionless Pressure Distributions using Air
s/a = 0.0138, 0.0276

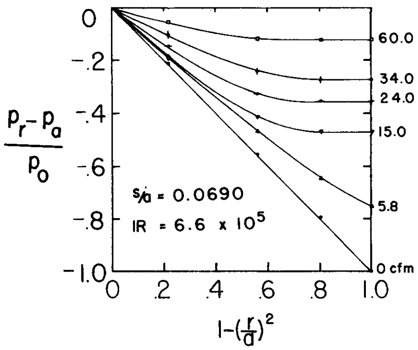

Fig. 63

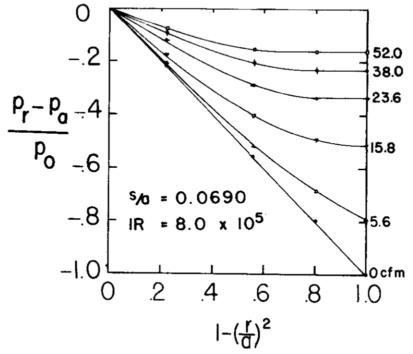

Fig. 64

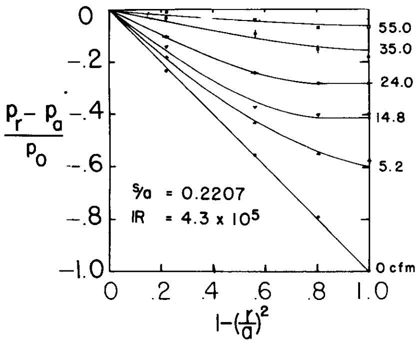

Fig. 65

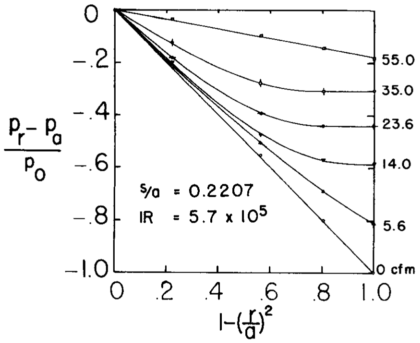

Fig. 66

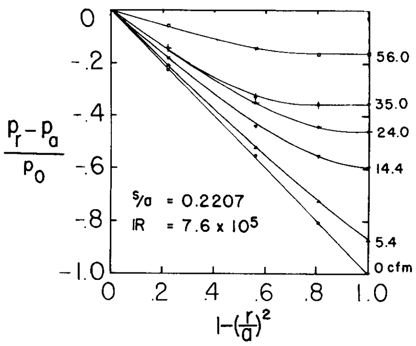

Fig. 67

Figs. 63-67 Dimensionless Pressure Distributions using Air
s/a = 0.069, 0.2207

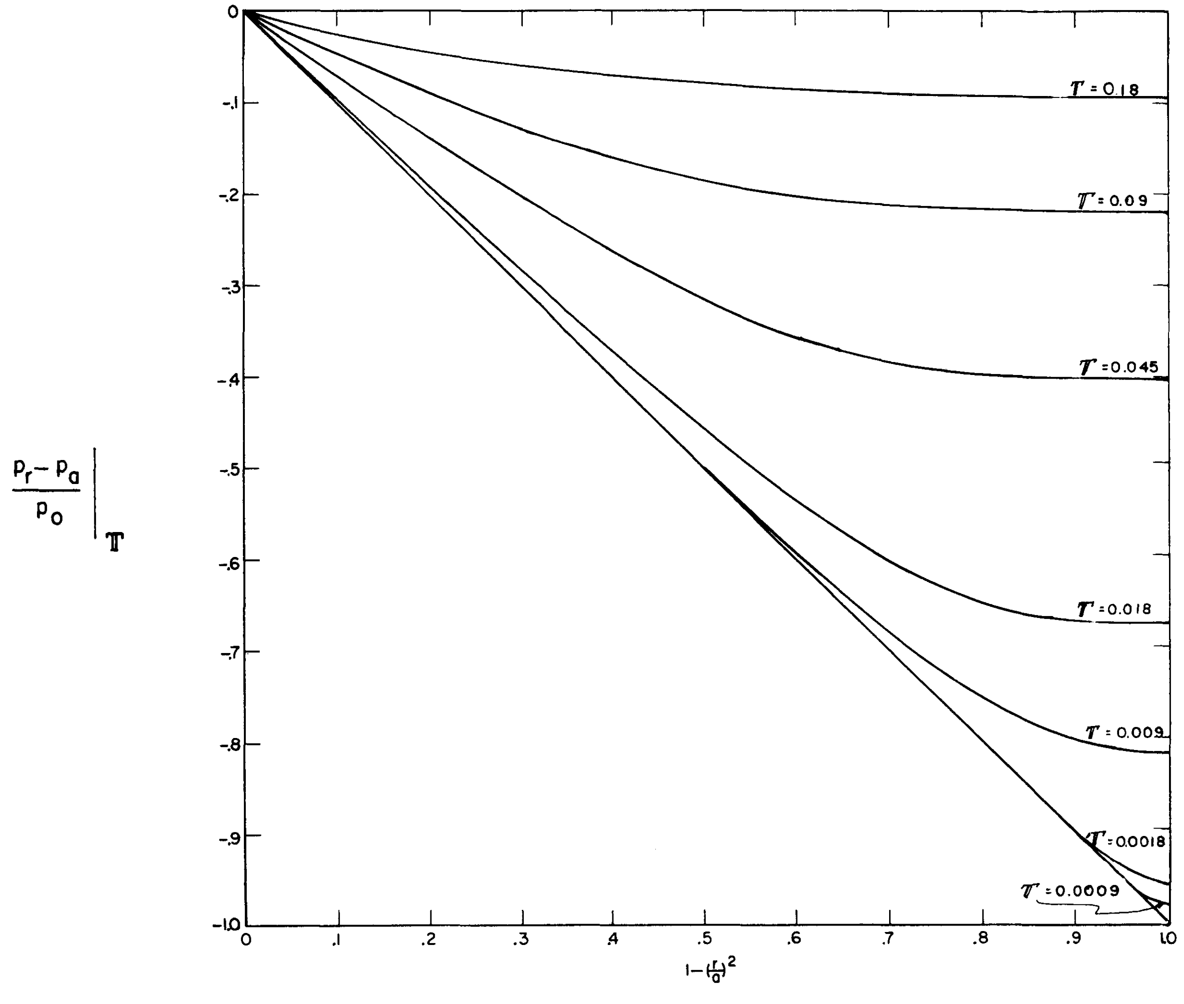

Fig. 68 Theoretical Pressure Distribution: $\overline{Q} = 0$

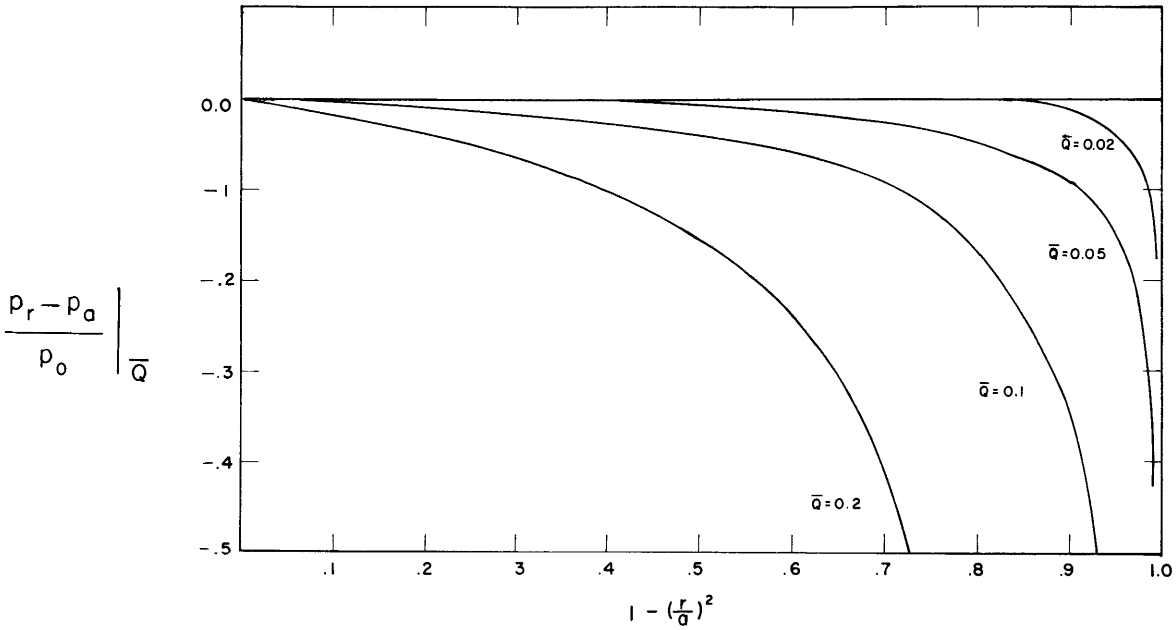

Fig. 69 Theoretical Pressure Distribution: $\mathbb{T} = 0$

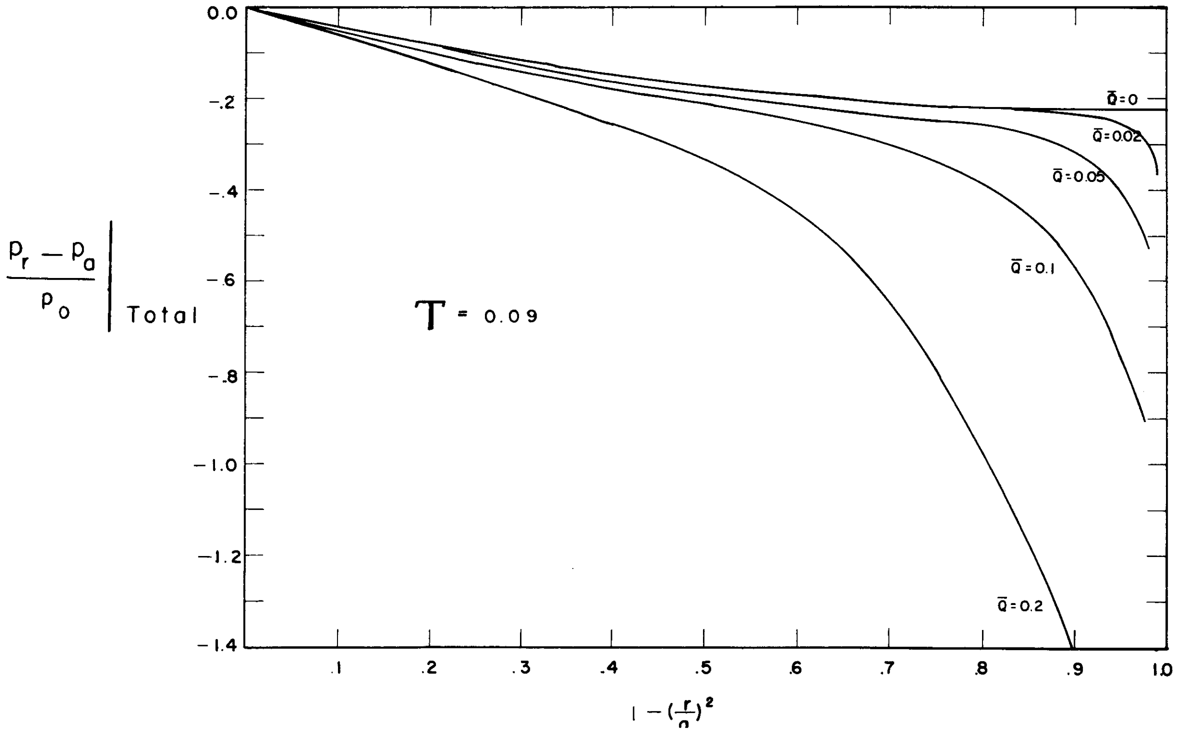

Fig. 70 Theoretical Pressure Distribution due to Combined Effects.

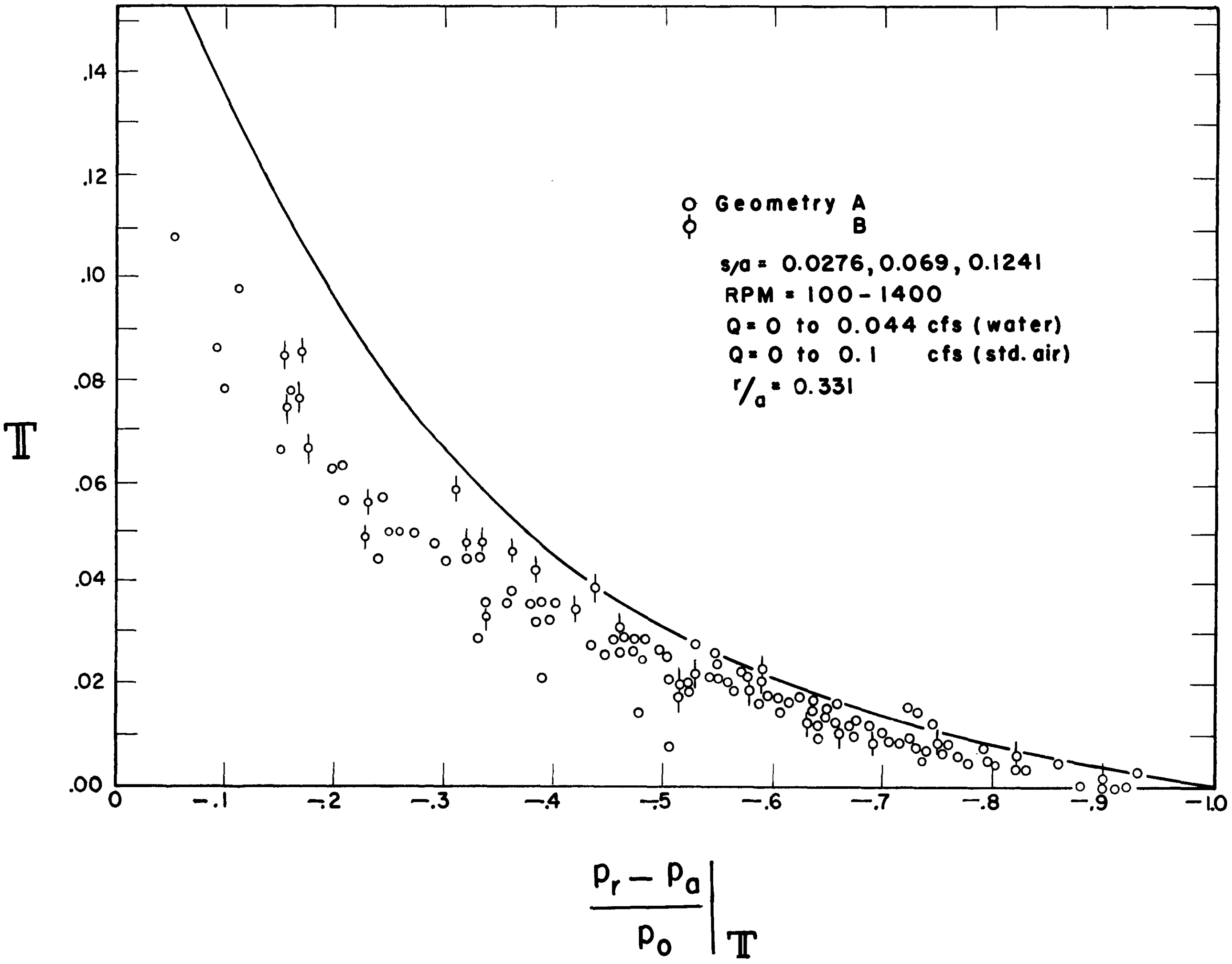

Fig. 71 Theoretical and Measured Pressure Distributions as Functions of Throughflow Number: r/a = 0.331

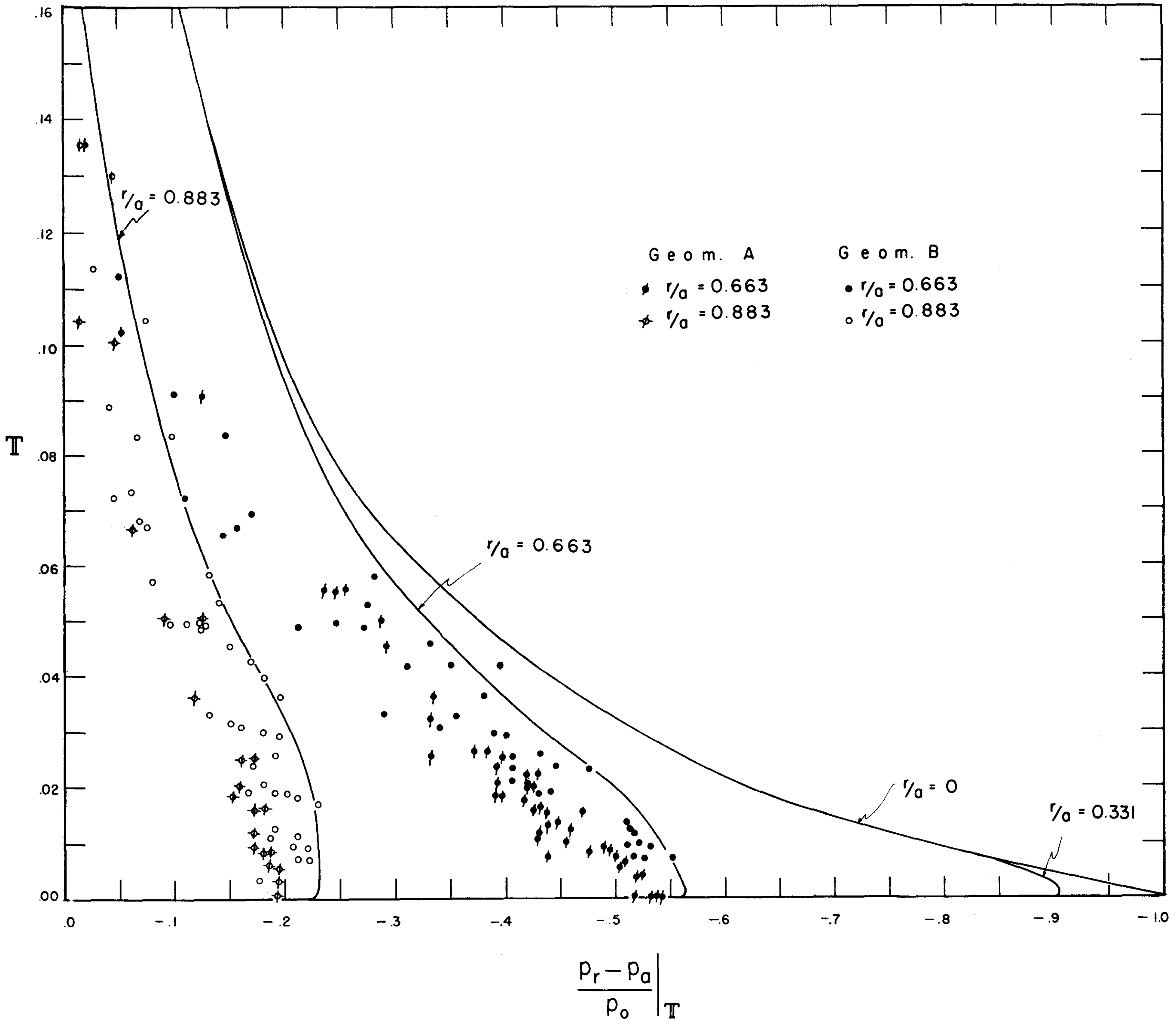

Fig. 72 Theoretical and Measured Pressure Distributions as Functions of Throughflow Number: r/a = 0.663, 0.883

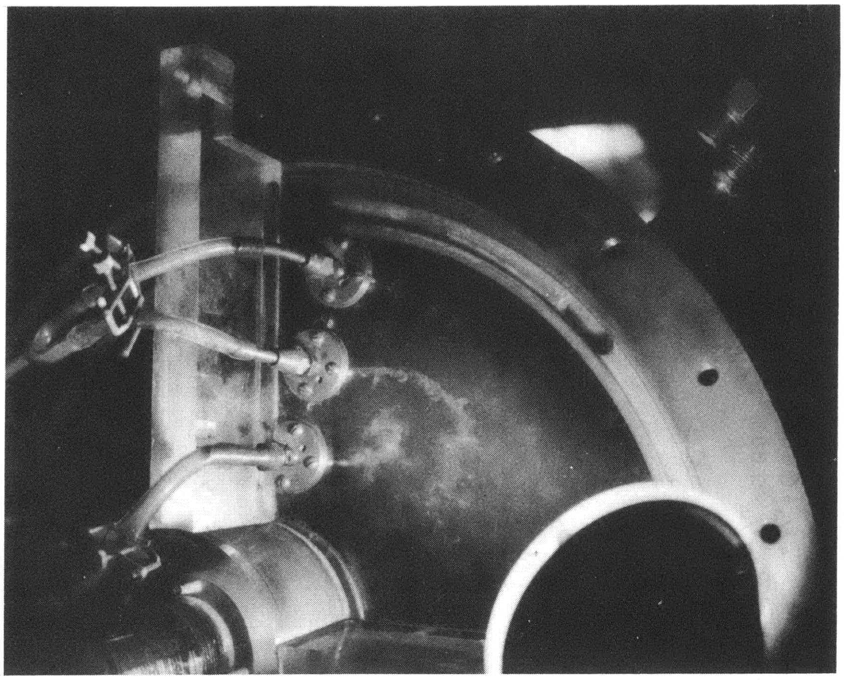

Fig. 73 Example of Periodic Fluctuation with Geometry A (New)

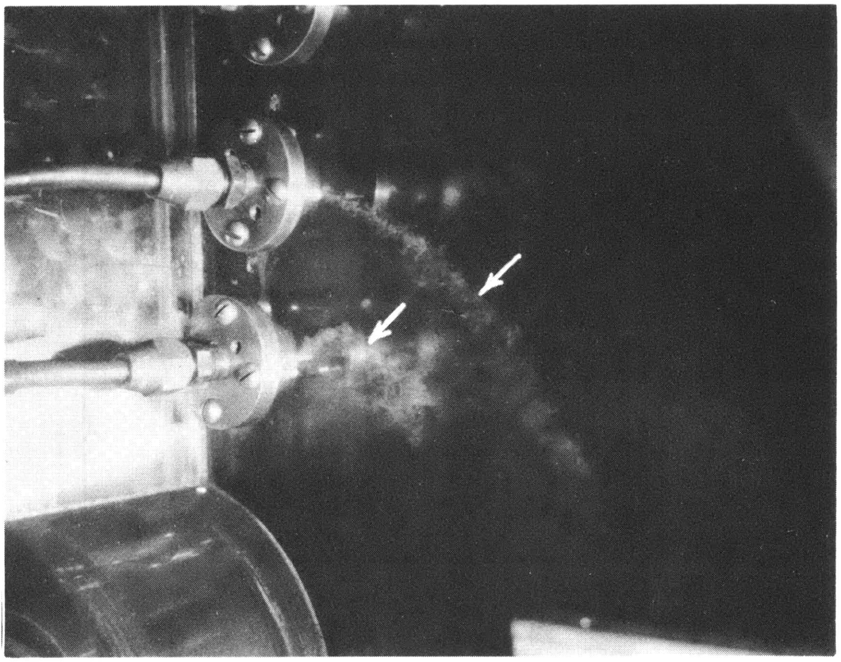

Fig. 74 Example of Periodic Fluctuation with Geometry B (Old)

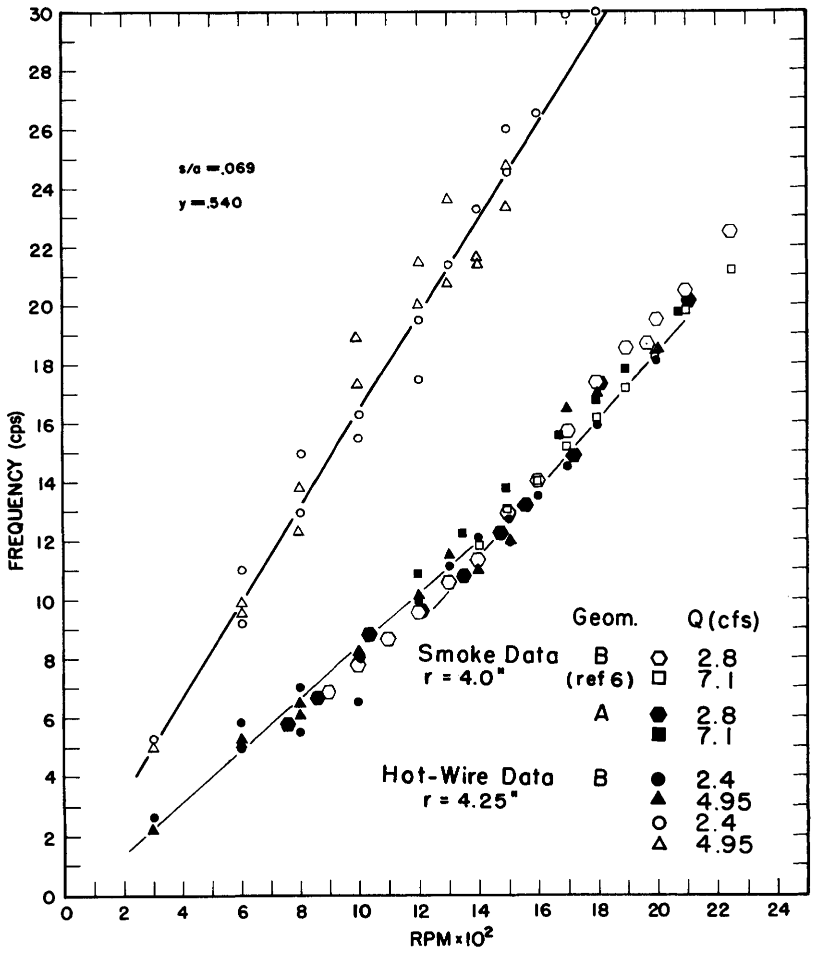

Fig. 75 Fluctuation Frequencies as Determined by Smoke Visualization and by Power Density Spectra: r = 4.0 and 4.25 inches

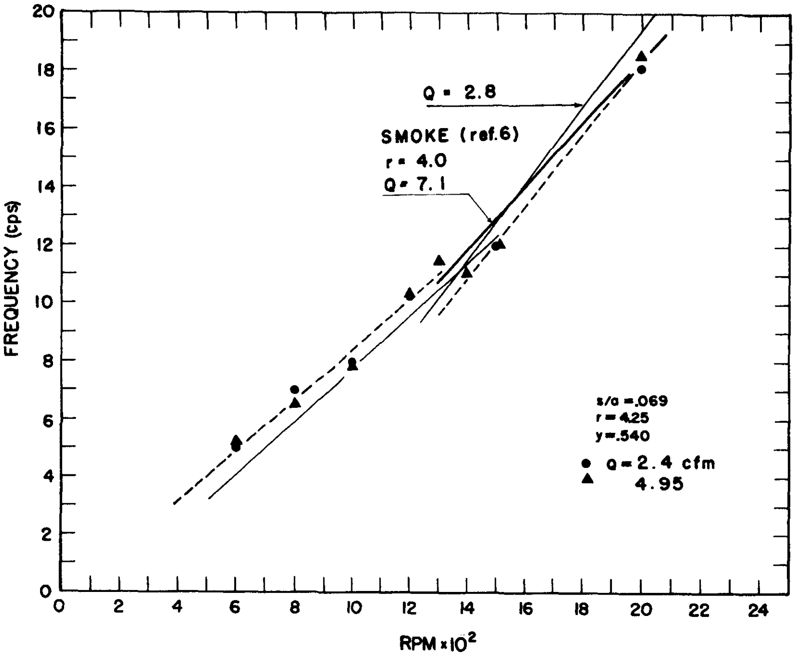

Fig. 76 Fluctuation Frequencies as Determined by Power Density Spectra: r = 4.25 inches

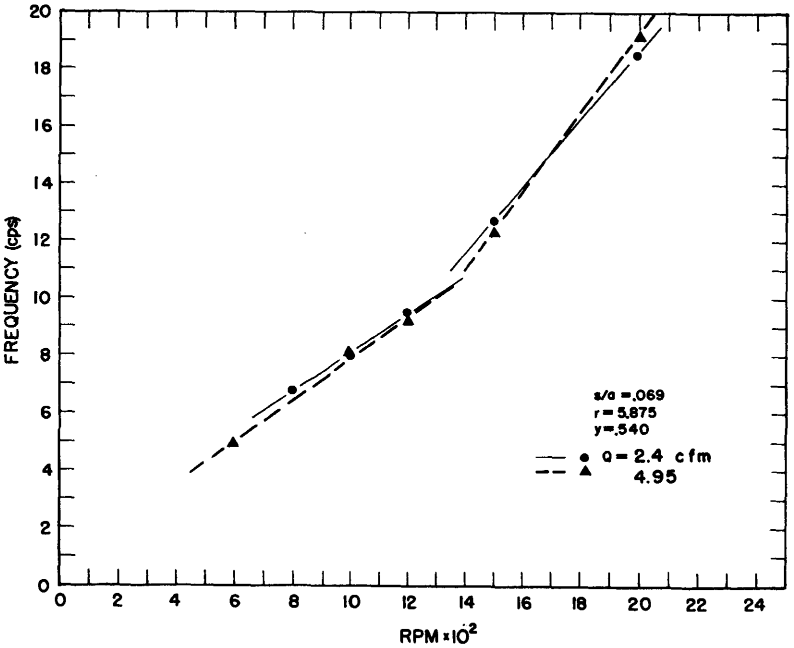

Fig. 77 Fluctuation Frequencies as Determined by Power Density Spectra: r = 5.875 inches

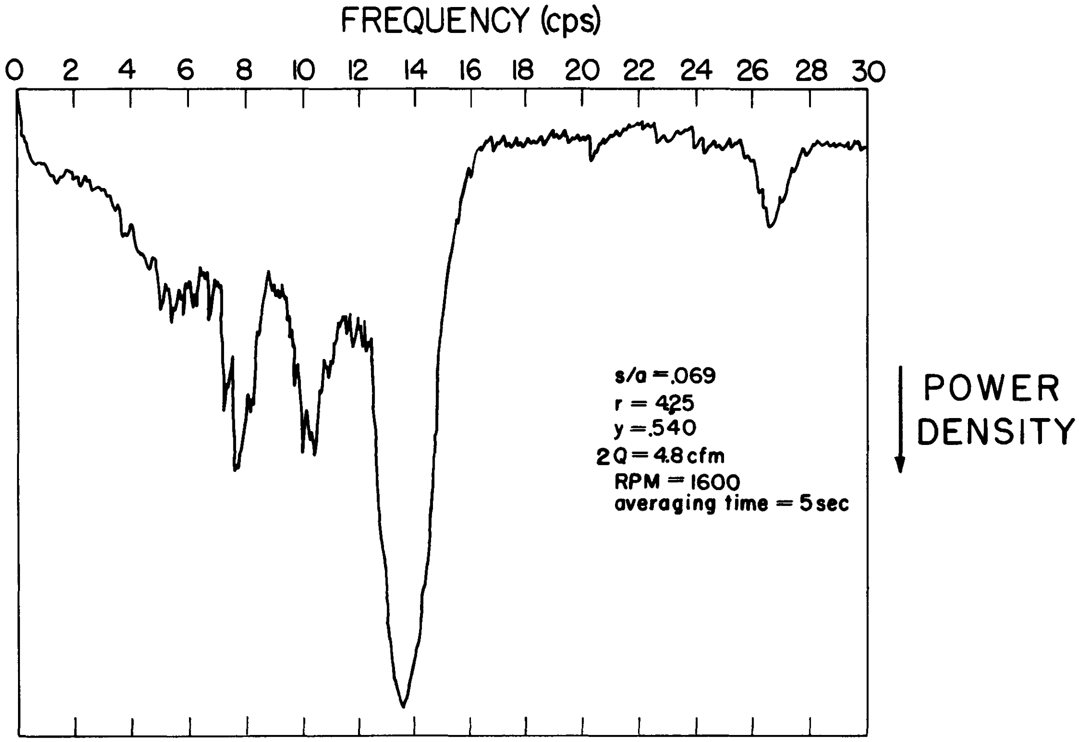

Fig. 78 Typical Power Density Spectra from Analyzer

OFFICIAL DISTRIBUTION LIST
(R64-16)

Commanding Officer
Army Research Office (Durham)
Attn: CRD-AA-1
Box CM, Duke Station
Durham, North Carolina 5

Chief of Ordnance
Attn: ORDTB
Hq, Department of the Army
Washington 25, D. C. 1

Chief of Research & Development
Attn: Research Division
Department of the Army
Washington 25, D. C. 1

Commanding General
Aberdeen Proving Ground
Attn: Technical Library, Bldg. 313
Aberdeen Proving Ground, Maryland 1

Commanding Officer
Detroit Arsenal
Attn: Technical Library
Center Line, Michigan 1

Commanding General
Frankford Arsenal
Attn: Technical Library
Bridge-Tacony Streets
Philadelphia 37, Pennsylvania 1

Commanding Officer
Picatinny Arsenal
Attn: Technical Information Service
Dover, New Jersey 1

Commander
Army Rocket & Guided Missile Agency
Attn: Technical Library
Redstone Arsenal, Alabama 1

Commanding General
Army Ballistic Missile Agency
Attn: Technical Library
Redstone Arsenal, Alabama 1

Commanding Officer
Springfield Armory
Attn: R & D Division
Springfield, Massachusetts 1

Commanding Officer
Rock Island Arsenal
Attn: 9340 Documents Section
Rock Island, Illinois 1

Commanding General
Ordnance Weapons Command
Attn: Research Branch
Rock Island, Illinois 2

Commanding General
Watervliet Arsenal
Attn: ORDBF-R
Watervliet, New York 1

Commanding Officer
Ordnance Materials Research Office
Watertown Arsenal
Watertown 72, Massachusetts 1

Commanding Officer
Watertown Arsenal
Attn: Technical Information Section
Watertown 72, Massachusetts 1

Commanding General
Hq, White Sands Missile Range
Attn: ORDBS-OM-TL
White Sands Missile Range,
New Mexico 1

Commanding General
Hq, White Sands Missile Range
Attn: ORDBS-OM-SAO
Whitesands Missile Range,
New Mexico

Commanding Officer
Diamond Ordnance Fuze Laboratories
Attn: Tech. Ref. Section ORDTL-PQW
Washington 25, D. C. 1

The Defence Research Member
Canadian Joint Staff
2450 Massachusetts Avenue
Washington 8, D. C. 1

Office of Naval Research
Attn: Code 438
Washington 25, D. C. 1

The Director
Naval Research Laboratory
Washington 25, D. C. 1

Commanding Officer
Officer of Naval Research
Branch Office
Navy 100, Box 39, FPO
New York, New York 2

Commander
U. S. Naval Weapons Laboratory
Dahlgren, Virginia

U. S. Naval Ordnance Laboratory
Attn: Library Division
White Oak, Silver Spring 19,
Maryland

Commanding Officer
U. S. Naval Propellant Plant
Indian Head, Maryland 1

Chief, Bureau of Weapons
Attn: Technical Library
Navy Department
Washington 25, D. C. 1

Director
Air University Library
Maxwell Air Force Base, Alabama 1

Commander
Wright Air Development Division
Attn: Technical Library
Wright-Patterson Air Force Base,
Ohio 1

Director
National Bureau of Standards
Washington 25, D. C. 1

National Aeronautics and Space
Administration
Attn: Chief, Research Coordination
1512 H Street, N. W.
Washington 25, D. C. 1

Commanding Officer
Engineering Research & Development
Laboratory
Fort Belvoir, Virginia 1

Armed Services Tech. Info. Agency
Arlington Hall Station
Arlington 12, Virginia 10

Director, Applied Physics Lab.
Johns Hopkins University
8621 Georgia Avenue
Silver Spring, Maryland 1

Technical Information Service
Attn: Reference Branch
P. O. Box 62
Oak Ridge, Tennessee 1

Director
Jet Propulsion Laboratory
California Institute of Technology
Pasadena 3, California 1

U. S. Army Standardization Group
Box 65, USN 100
United Kingdom
FPO New York, New York 2

Commanding Officer
U. S. Army Transportation
Research Command
Attn: Technical Services Division
Fort Eustis, Virginia 1

Commander
Air Force Office of Scientific
Research
Attn: Director of Information
Washington 25, D. C. 1

Commanding General
U. S. Army Medical R & D Command
Main Navy Building
Attn: Basic Science Research
Branch
Washington 25, D. C. 1

Commanding Officer
U. S. Army Signal R & D Laboratory
Attn: Technical Documents Center
Fort Monmouth, New Jersey 1

Commanding Officer
U. S. Army Signal R & D Laboratory
Attn: Director of Research
Fort Monmouth, New Jersey 1

Commanding Officer
U. S. Army Transportation
Research Command
Fort Eustis, Virginia 1

Commanding Officer
U. S. Army Chemical R & D Lab.
Attn: Tech. Library, Room 200,
Building 330
Army Chemical Center, Maryland 1

Commanding Officer
U. S. Army Biological Laboratories
Fort Detrick
Frederick, Maryland 1

Commanding General
U. S. Army CmLC R & D Command
Attn: Chemical Division
Washington 25, D. C. 1

Office of the Chief Signal Officer
Research & Development Division
Attn: Signal Research Office
Room 2D, 244, The Pentagon
Washington 25, D. C. 1

Commanding General
Hq, R & E Command, U. S. Army
QM R & E Center
Attn: Tech. Services Div, Tech
Library
Natick, Massachusetts 1